5.
Results and Discussion

The mass balance for slag and metal phases are strongly dependent on the decarburization and FeO reduction kinetics. The model parameters are computed in order to fit the measured chemical composition of both phases, consequently, such parameters are influenced by the rate of carbon availability in the metal phase. Hence, the melting rates of carbon sources such as scrap and pig iron are very relevant.

The diversity of transient mechanisms that are taking place during an EAF operation makes the preheating and melting processes very complex to be modeled, even when it is broken down to their more simple steps. Scrap charged to BOF is accepted to be a dissolution process, while in an EAF, it may be considered as a mix of both mechanisms (dissolution and melting). The high carbon content of HBI and pig iron causes their liquidus temperatures to be significantly lower than the metal phase, indicating that melting mechanism could be predominant.

In modern EAF facilities, whenever amounts of solid pig iron higher than 20% are charged under high electrical power input of 0.70 – 1.0 MW/ton, events of non-molten pig iron or sudden turbulent chemical reactions, like intense boiling, at the end of refining process have been reported. The intense turbulence is presumed to be caused by high CO production rate. This phenomenon is also known as “slopping”.

Industrial evidences have indicated that the heat transfer is controlling the pig iron melting rate in the EAF. Hot heel “chilling” effect may be occurring and slowing down its melting rate.

5.1.
Decarburization and Slag Formation – Industrial Tests

The data collected from metal and slag phases were submitted to the GRG algorithm, and the results of model prediction versus measured chemistries are presented in the next figures. Of the twenty-eight heats, at least twenty-seven heats presented acceptable model prediction. After removing outliers samples (8-11% for metal phase samples and 4% for slag phase), carbon content in the metal phase showed a limited agreement of the model prediction and measured results, and indicated a good agreement for FeO content in the slag. Linear regression coefficients (R2) for the model prediction versus measured results are 0.75 for carbon and 0.92 for iron oxide. For carbon, 188 samples were accepted and 205 samples were fully utilized for iron oxide calculations.

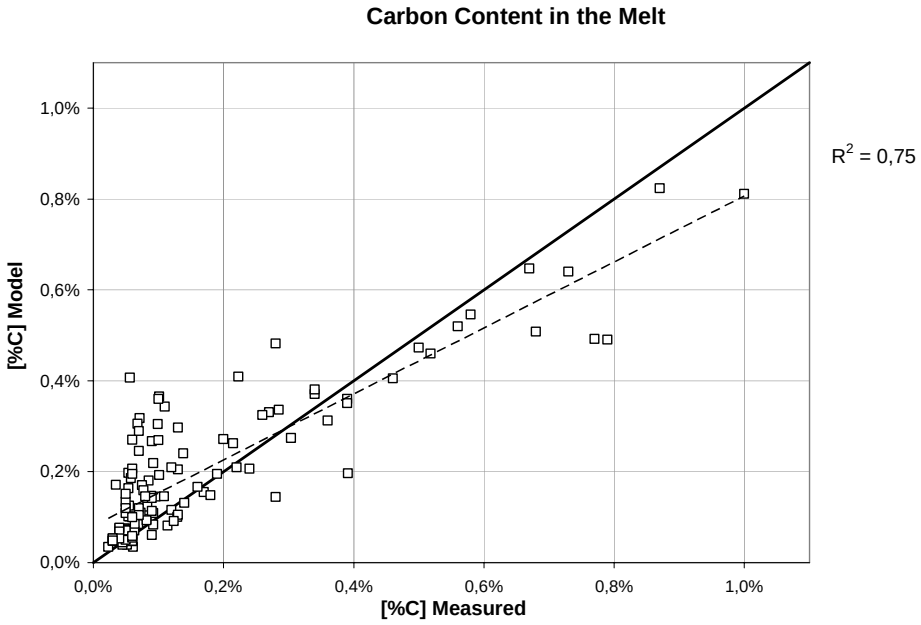

Figure 64 – %wt C measured in the metal phase vs. model prediction.

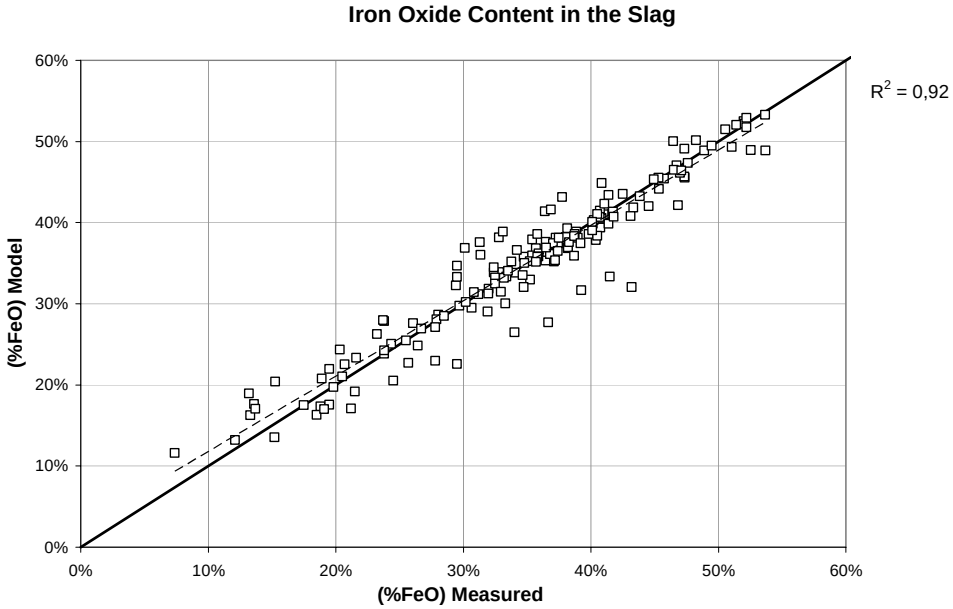

Figure 65 – %wt FeO measured in the slag vs. Model prediction.

Other estimates for the most relevant oxides present in the slag phase are shown in Figure 66 to Figure 70, and additional species Si and P dissolved in the metal phase are presented in Figure 71 and Figure 72, respectively .

Mass concentration estimates for CaO and SiO_2 are consistent with the measured quantities. The MgO mass concentration estimates seem to be affected by dololime chemical composition (assumed constant), and/or also influenced by other oxides estimates.

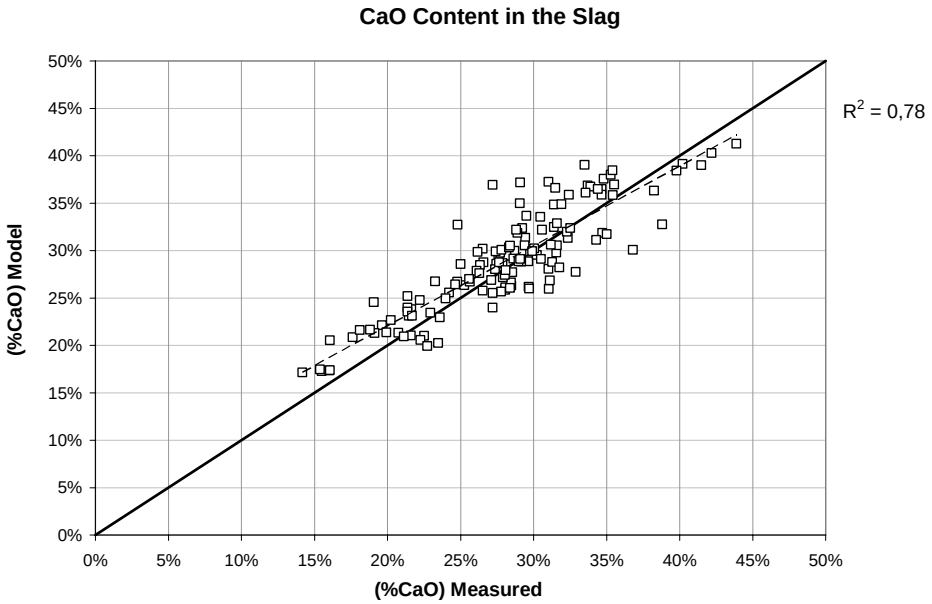

Figure 66 – %wt CaO measured in the slag vs. Model prediction.

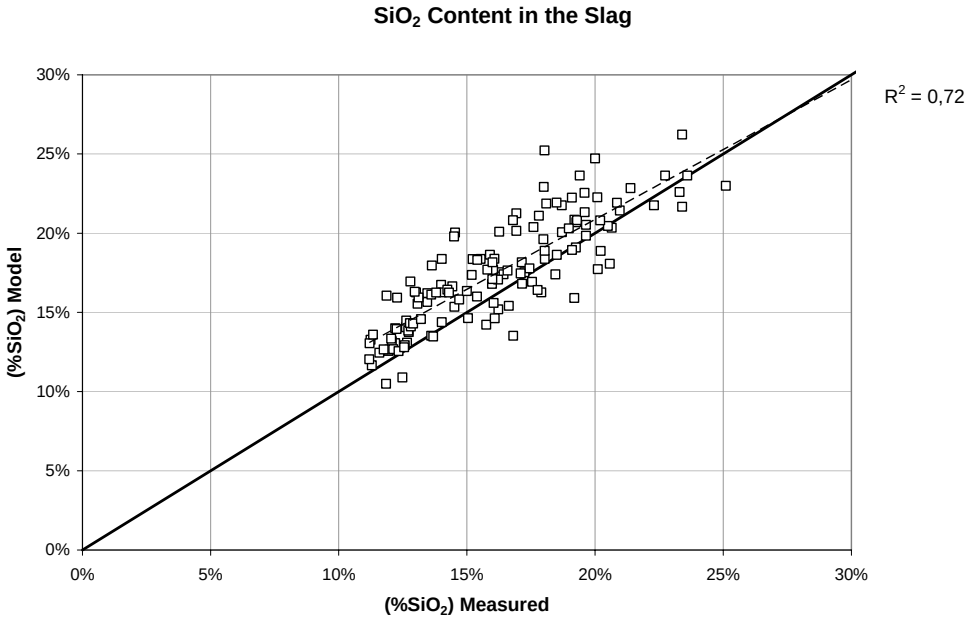

Figure 67 – %wt SiO_2 measured in the slag vs. Model prediction.

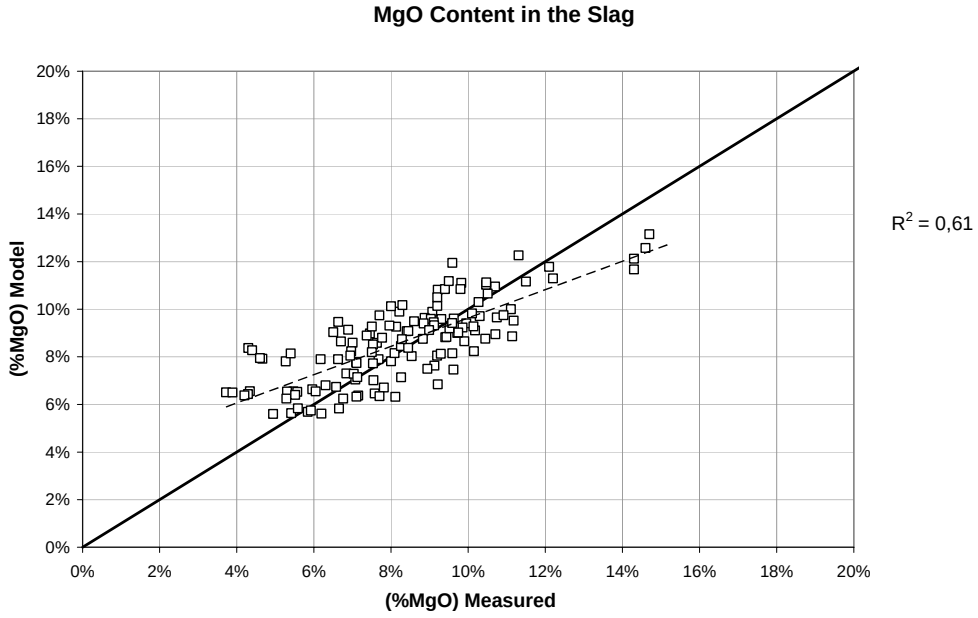

Figure 68 – %wt MgO measured in the slag vs. Model prediction.

The MnO and P_2O_5 mass concentration estimates presented lower correlation with the measured quantities maybe due to their lower amounts, narrow variation ranges, and less accuracy provided by the slag analyzer. However, they have minor influence on mass balance.

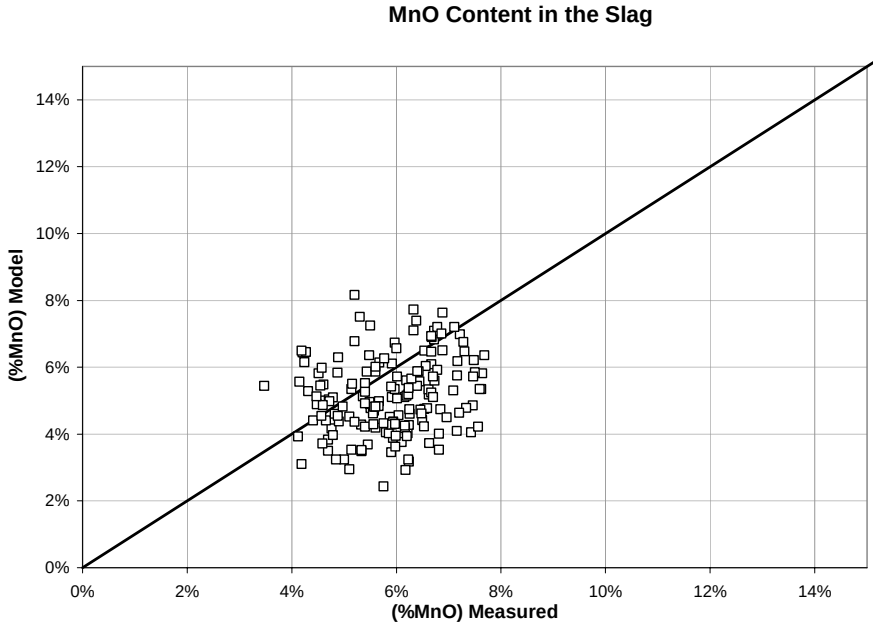

Figure 69 – %wt MnO measured in the slag vs. Model prediction.

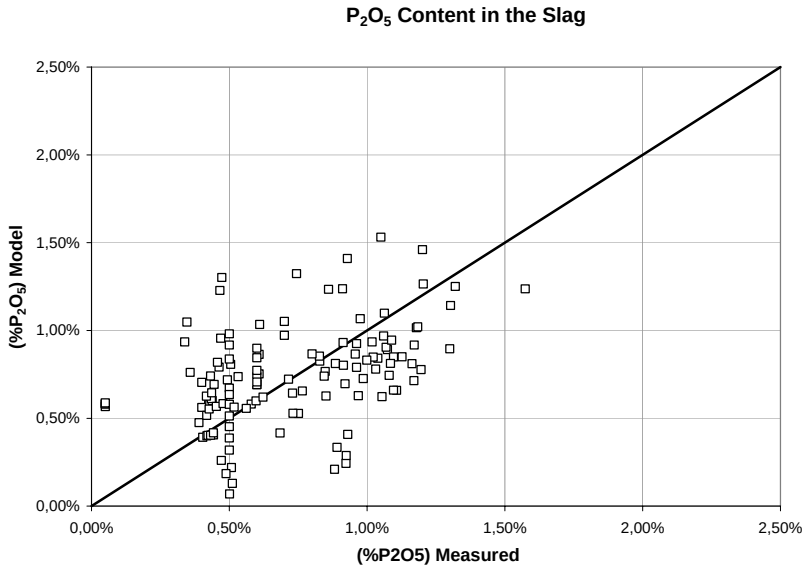

Figure 70 – %wt P_2O_5 measured in the slag vs. Model prediction.

As expected from the equilibrium condition calculation, the mass concentration of silicon was often very low and the optical spectrometer calibration which is usually adjusted for %wt Si higher than 0.10% contributed to less accuracy in respect to the range of 0.010% or lower. In most cases, the availability of dissolved silicon in the metal phase followed the pig iron melting rate, which was lower than the scrap melting rate. Therefore, the high affinity of oxygen by silicon made their mass concentration over the tap-to-tap time

(processing time) lower than 0.04%. Highest contents around 0.08% were achieved when low and delayed oxygen injection took place.

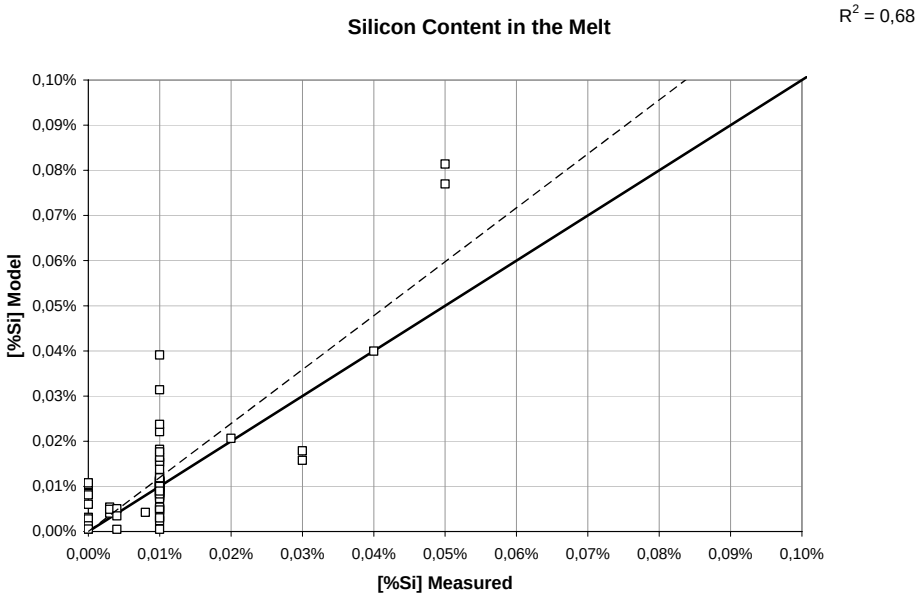

Figure 71 – %wt Si measured in the metal phase vs. Model prediction.

In the context of industrial applications, the mass concentration of phosphorus was reasonably consistent.

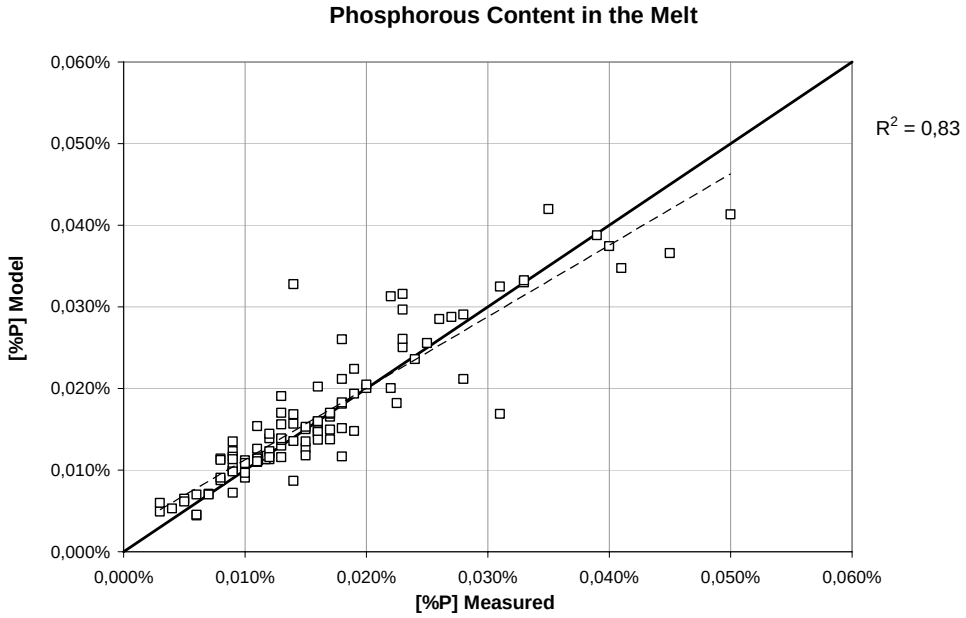

Figure 72 – %wt P measured in the metal phase vs. Model prediction.

Examples of the chemistries profiles of slag and metal phases in the course of processing time for two heats are presented. Actually, two limiting situations were selected to briefly demonstrate the model sensitivity: heat 78787 (Figure

73), 8% of charged pig iron, no oxygen flow through the lances and simultaneous full coke injection for 5 minutes in the refining step; the second heat 80121, 32% of pig iron was charged, full oxygen flow through the lances and no coke injection for 6 minutes in the refining step, are presented in Figure 74. In both cases, the model prediction was reasonably good.

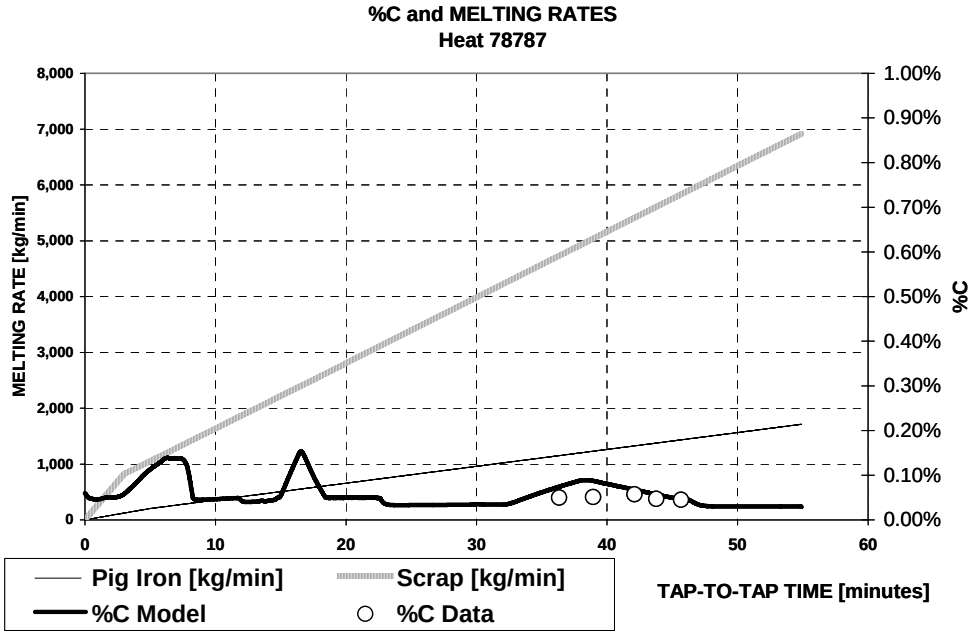

(a)

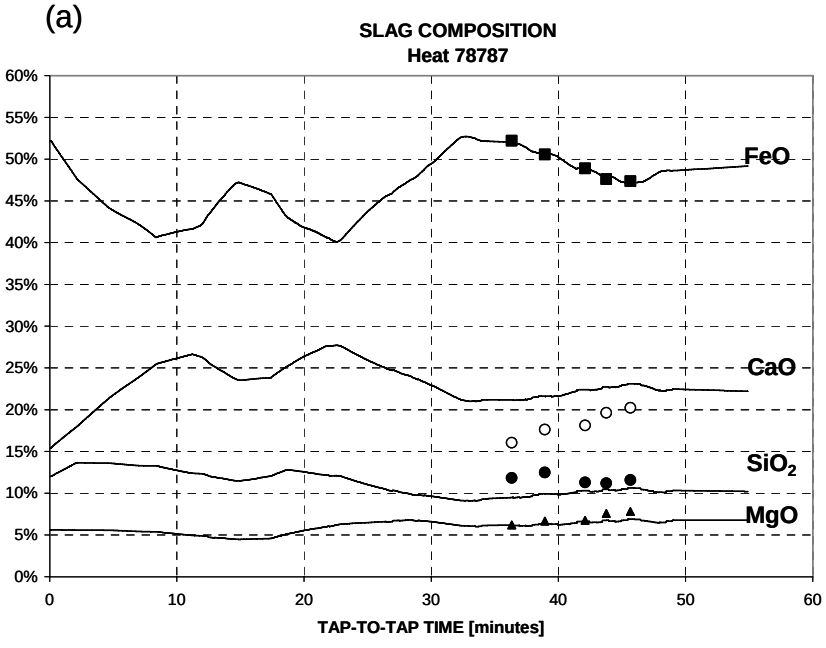

(b)

Figure 73 - Model prediction (lines) and experimental data (discrete points) for (a) carbon content in the metal phase and melting rates of pig iron and scrap blend; (b) slag composition along the heat 78787. Charge 8% of pig iron, and melt not submitted to oxygen flow through the lances and full coke injection during 5 minutes in the interval of 38 to 43 minutes of the tap-to-tap time.

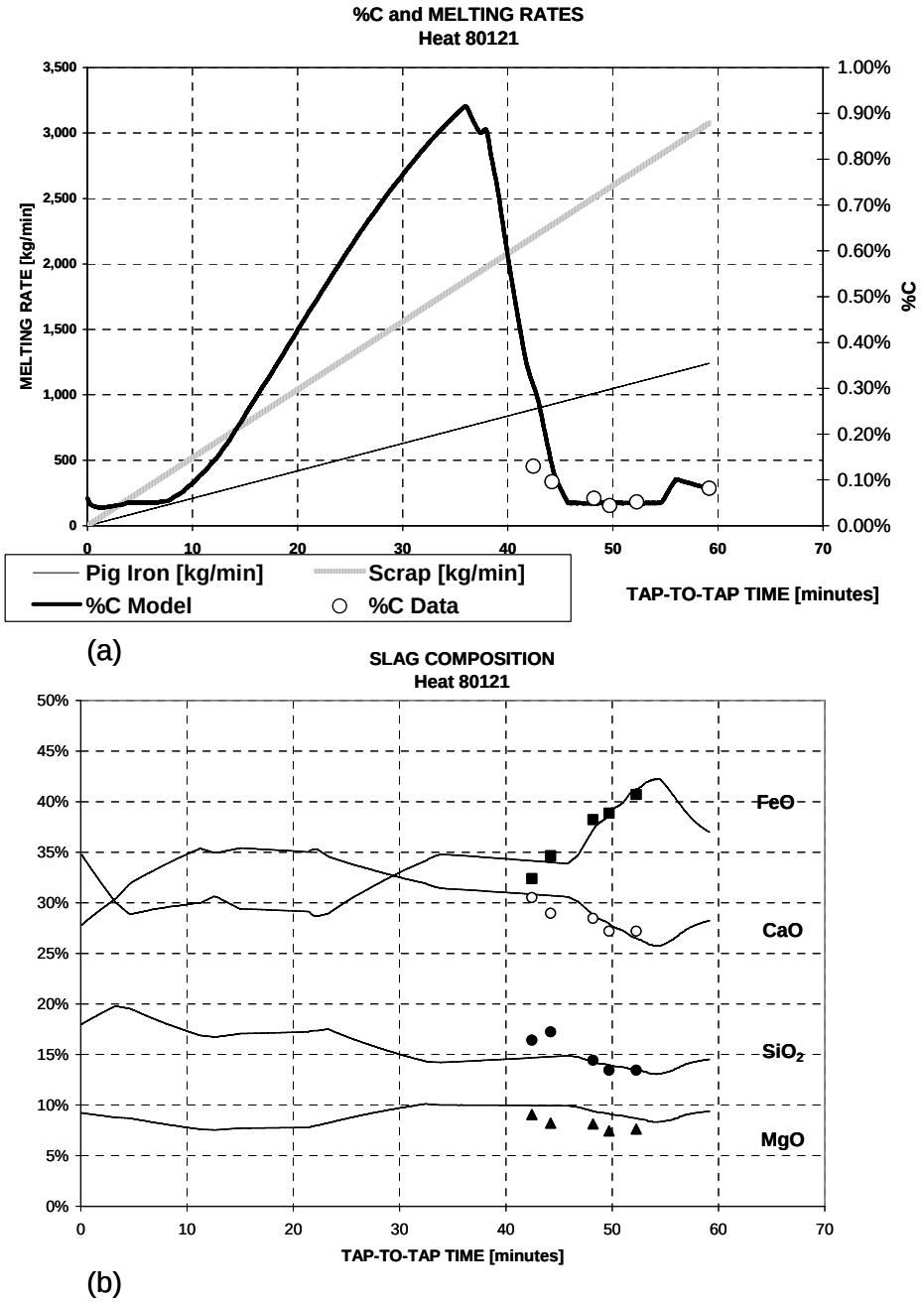

Figure 74 – Model prediction (lines) and experimental data (discrete points) for (a) carbon content in the melt and melting rates of pig iron and scrap blend; (b) slag composition along the heat 80120. Charge 32% of pig iron, and melt submitted to full oxygen flow through the lances and no coke injection during 6 minutes in the interval of 27 to 34 minutes of power on time.

Figure 75 shows an example of model mass balance for slag: slag produced, slag formers dissolution, slag off, carbon injected but not reacted in time and the slag mass resident in EAF.

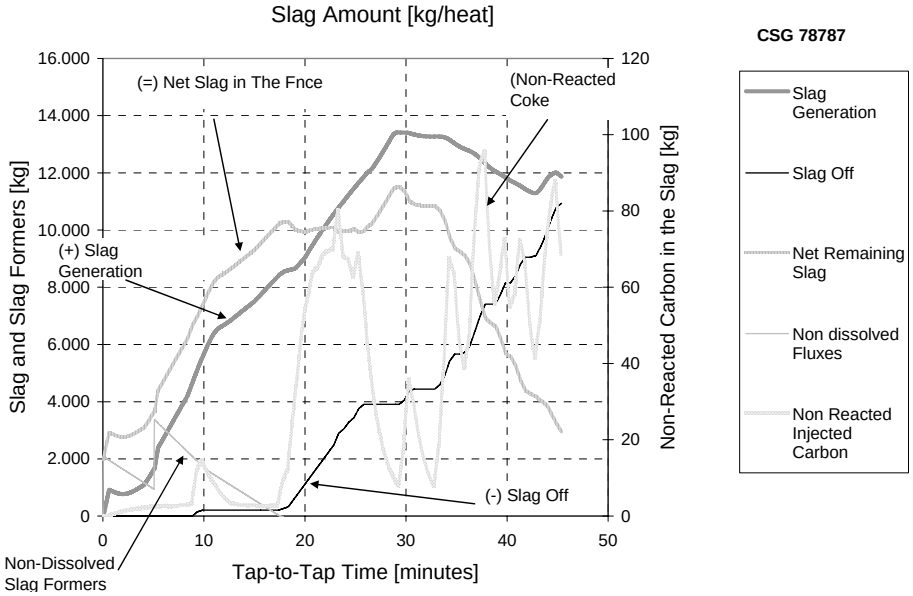

Figure 75 – Model prediction Net Slag = (+) Slag Generated (-) Slag Off, non-reacted carbon and non-dissolved fluxes along the heat 78787.

Table 21 summarizes the primary and the secondary parameters values, as well their allowed variation ranges used to define the constraints for the GRG algorithm.

Table 21 – Summary of the GRG calculation for model parameters.

				SQP CONSTRAINT RANGE		AVERAGE	d[%C]/dt *(iv)*
				min	max		%C/min
Decarburization	Decarburization Rate Parameter ([%C]>[%C]^{Cr})	k_{C1} *(i)*	[Nm3^{-1}]	No constrain		1,5E-03	**0,21%**
	Decarburization Rate Parameter ([%C]<[%C]^{Cr})	k_{C2} *(ii)*	[min^{-1}]	No constrain		0,74	**0,03%**
	Critical %Carbon	$[\%C]^{Cr}$	[%]	0,05%	0,80%	0,19%	
Desiliconization	Desiliconization coefficient	k_{Si}	[min^{-1}]	No constrain		0,98	
	Critical %Silicon	$[\%Si]^{Cr}$	[%]	0,003%	0,50%	0,14%	
	Ratio k_{C2} / k_{Si} Model Avg			0,4	2,5	0,76	
Dephosphorization	"a" mA Product for Phosphorous Removal	a	[m^3/min]	0	2,00	1,38	
	"b" mA Product for Phosphorous Removal	b	[min^{-1}]	0	0,50	0,005	
	Dephosphorization Parameter average 50-100 ton	k_P	[min^{-1}]	No constrain		0,131	
	Ratio k_{C2} / k_P Model Avg			0,5	15	5,7	
Post Combustion Ratio	Post combustion Ratio maximum. It is the maximum value for post combustion ratio regarding the C->CO, CO2 above the slag promoted by PC Injectors	$R_{PC}^{Max\,Atm}$	[%]	0,1	0,80	0,80	
		$R_{PC}^{Avg\,Atm}$	average (iii) ->			0,11	
	Post combustion Ratio in the Slag. It is the average value for post combustion ratio in the slag due to FeO + CO = Fe + CO2	R_{PC}^{Slag}	[%]	0,00	0,05	2,5%	
Iron Oxide Reduction	FeO reduction rate constant. $k_{FeO->Fe}$ (Coke reaction).	k_{red}	[min^{-1}]	0,10	10,00	1,39	

				SQP CONSTRAINT RANGE		AVERAGE
				min	max	
Initial Slag Amount	Initial slag amount	$W_{initial}^{Slag}$	[ton]	1	5	2,4
Oxygen - Lancing Injector	Effectiveness of the oxygen in excess from the lancing mode for the Fe oxidation to FeO. This coefficient concerns about the idle flame, which is not reaching the bath.	OLE_{FeO}	[%]	90%	100%	94%
Oxygen - Post Combustion Injector	Effectiveness of the oxygen available through the PC Injectors for decarburization purposes	$OPCE_{Decarb}$	[%]	10%	20%	15%
	Effectiveness of the oxygen available through the PC Injectors for FeO formation by reaction with solid scrap, steel bath surface and/or steel droplets	$OPCE_{FeO}$	[%]	50%	70%	58%
Raw Materials & Slag	Pig Iron Chemistry	$\%C\ (v)$	[%]			4,2%
		$\%Si\ (v)$	[%]			0,6%
		$\%P\ (v)$	[%]			0,12%
	Carbonaceous Materials - Injection Yield	n_{CMat}	[%]	85%	98%	95%
	Slag generated		[ton]			9,8
	Coke Injected		[kg/ton]			9,2
	Carbon Injected + Ferrous Blend		[kg/ton]			24,6
	Mix Density		[ton/m3]			0,77
Melting Rates	Pig Iron		%			27%
	Max Pig Iron Melting Rate		[kg/min]			1852
	Max Scrap Melting Rate		[kg/min]			4057
	Total Melting Rate		[kg/min]			3556

Part II

i) Average of constant of decarburization rate, according to the conditions tested. Just for illustration;
ii) Average of constant of decarburization rate after 90% of molten charge;
iii) Average of post combustion ratio including slag and EAF atmosphere, but not include the surrounding atmospheric air infiltration;
iv) Calculated decarburization rate [%C]/min at 6,000 Nm^3/h, melt weight of 50,000 t and critical carbon of 0,19%;
v) %C and %Si contents in pig iron were permitted to vary according to chemical analysis of the main suppliers;

The discussion of the variables presented above will be presented in the next sessions.

5.1.1.
Decarburization

Most of industrial tests conducted in this study presented a departure from the equilibrium computed for Fe-C-O system, regarding the reaction $[\underline{C}]+[\underline{O}]=CO$. Figure 76 makes evident the dispersive behavior of soluble carbon and oxygen in the metal phase. This fact has been observed in many other steelmaking facilities, hence, the validity of conclusions based on the presumed Fe-C-O equilibrium should be viewed with some degree of skepticism. Despite the fact that this model is limited, because other species in solution in iron were neglected, the departure from the equilibrium curve maybe also influenced by kinetic issues.

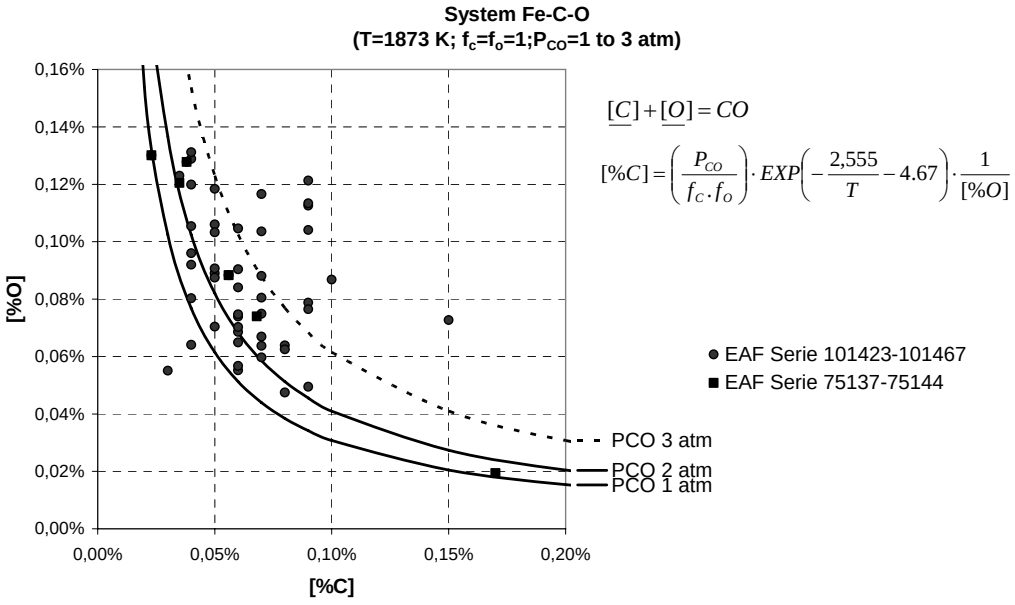

Figure 76 – Equilibrium curve for %C vs. %O soluble in iron melt, Henryan activity coefficients for carbon and oxygen are closer to 1.0. Plot of soluble oxygen measured by electrochemical probes and carbon content through optical spectrometer. Heats series 101423-101467 are additional samples.

In spite of accuracy issues, the trends for carbon content prediction were moderately achieved. Figure 77 presents a typical carbon content plot, where: (i) the carbon content in the metal phase is influenced by the pig iron melting rate; (ii) two carbon content peaks are related to the two buckets charge; (iii) the decarburization pattern is very different than the continuous decreasing of carbon content observed in OSM. A complex transient of simultaneous melting, competing dissolution-oxidation reactions of carbon and other alloying elements

are taking place along the EAF process time. In contrast, more than 80% of the ferrous charge is already molten at OSM, and high carbon content is available for continuous removal since the beginning; (iv) linear and non-linear decarburization occurrence indicates the effect of the balance between incoming carbon from pig iron melting and simultaneous carbon oxidation.

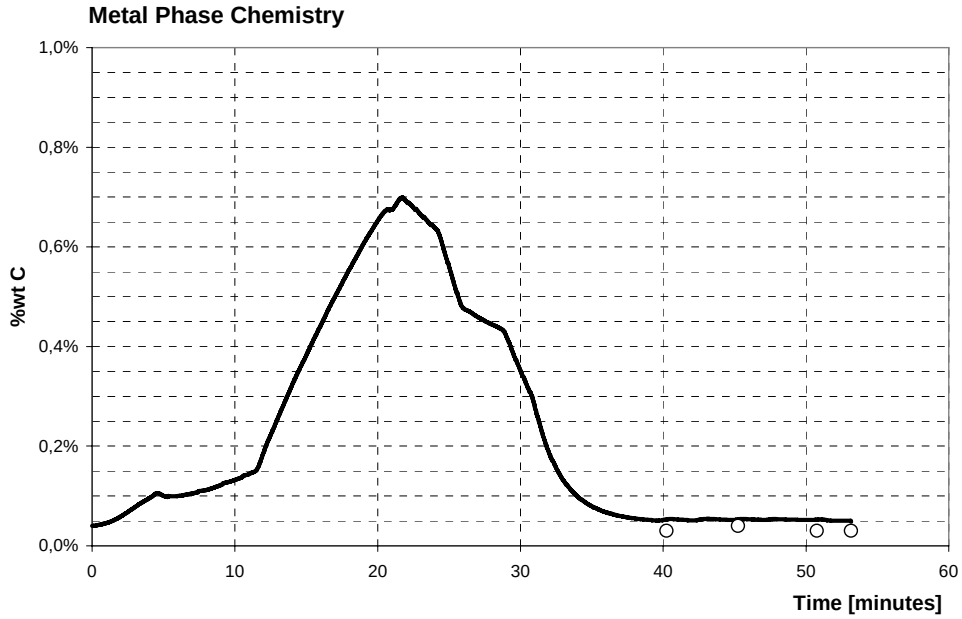

(a) 99735; 9% pig iron

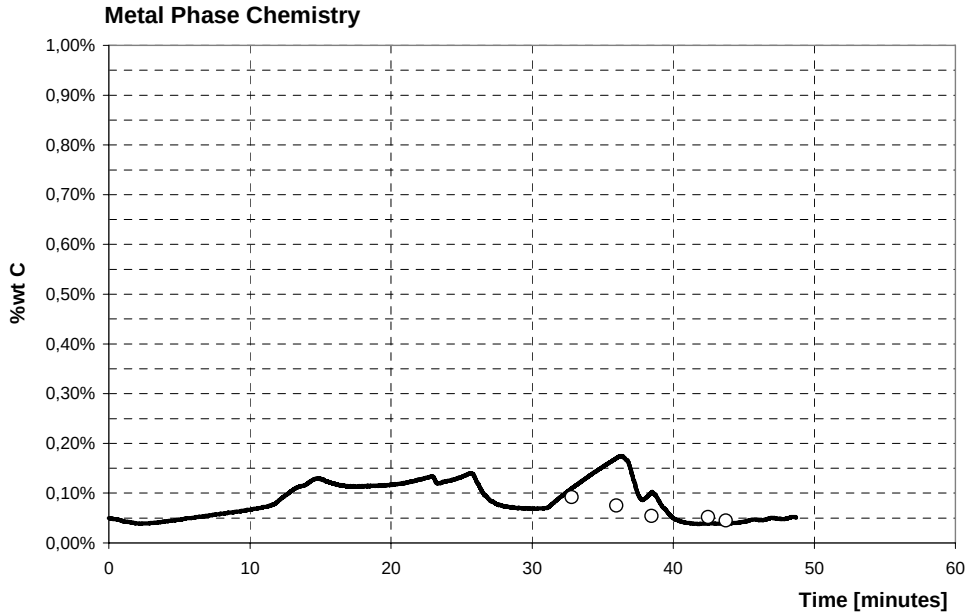

(b) 80883; 8% pig iron

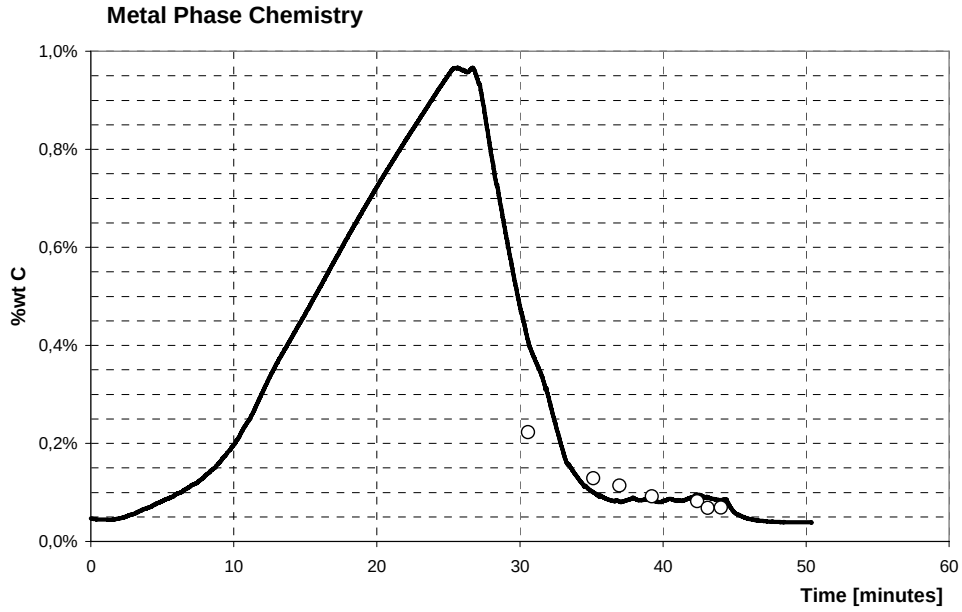

(c) 80120; 30% pig iron

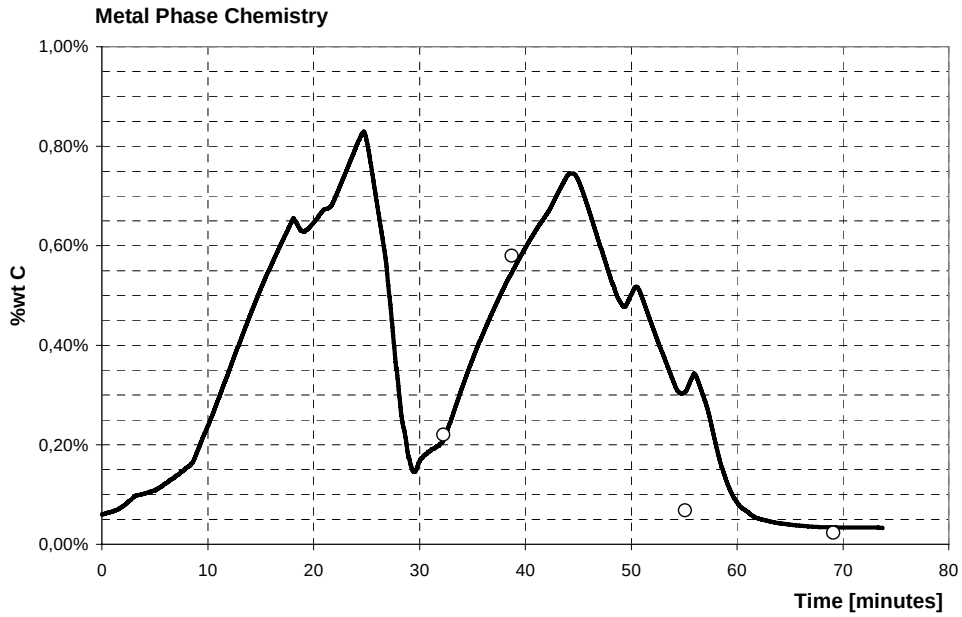

(d) 75138; 44% pig iron

Figure 77 – Model prediction for %wt carbon content (line) and experimental data (dots) along the heats (a) 99735, 9% pig iron; (b) 80883, 8% pig iron; (c) 80120, 30% pig iron; (d) 75138, 44% pig iron.

Dispersive behavior of carbon content presented in Figure 64 occurred more frequently in the heats with pig iron charge higher than 30% and, mostly in the beginning of the meltdown step. Figure 78 and Figure 79 denote this trend for low and high pig iron charge, respectively. Therefore, the melting rate of pig iron

and the carbon availability in the metal phase may not be following the melting rate model for every heat. The way the buckets are layered and the job procedures for charging, definitely contribute for different distribution of pig iron the EAF vessel.

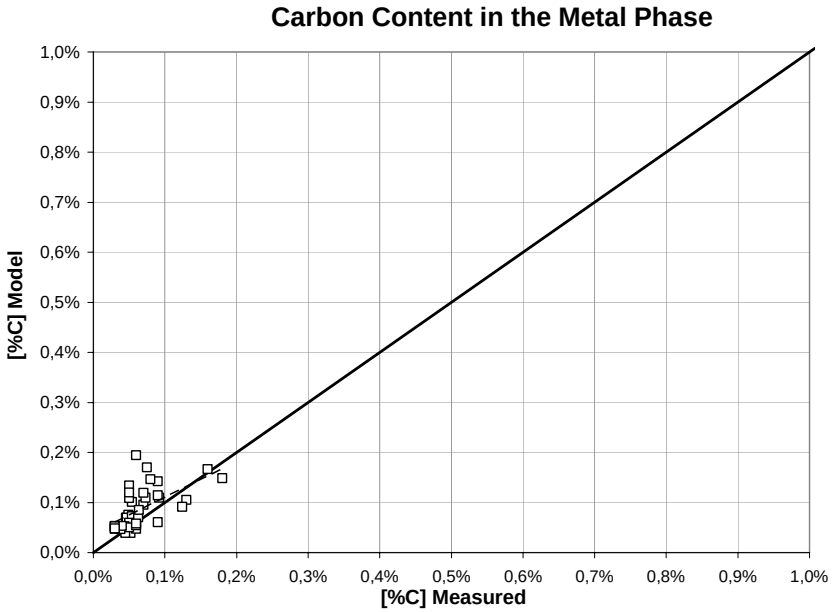

Figure 78 – %wt C measured in the metal phase vs. **m**odel prediction for pig iron charge in the range of 8% to 14%.

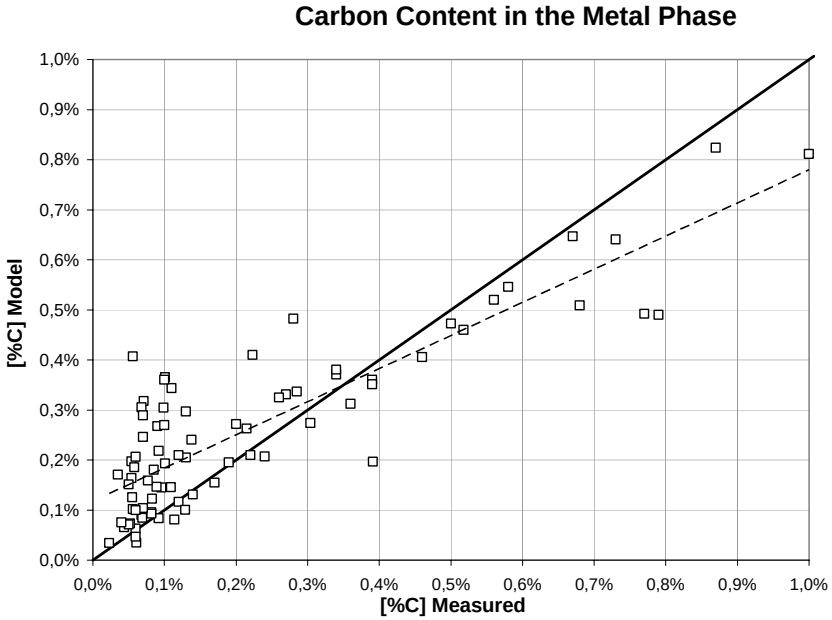

Figure 79 – %wt C measured in the metal phase vs. model prediction for pig iron charge in the range of 29% to 51%.

At this point, there was significant co-existing solid charge submerged in the hot heel, and it may have contributed to heterogeneous carbon distribution. It means that the premise of homogeneity of metal phase is not completely fulfilled. In the beginning of meltdown, distinct pools of liquid steel may form in the hot heel, separated partially by solid scrap barriers. Figure 80 presents two examples of carbon content prediction issues.

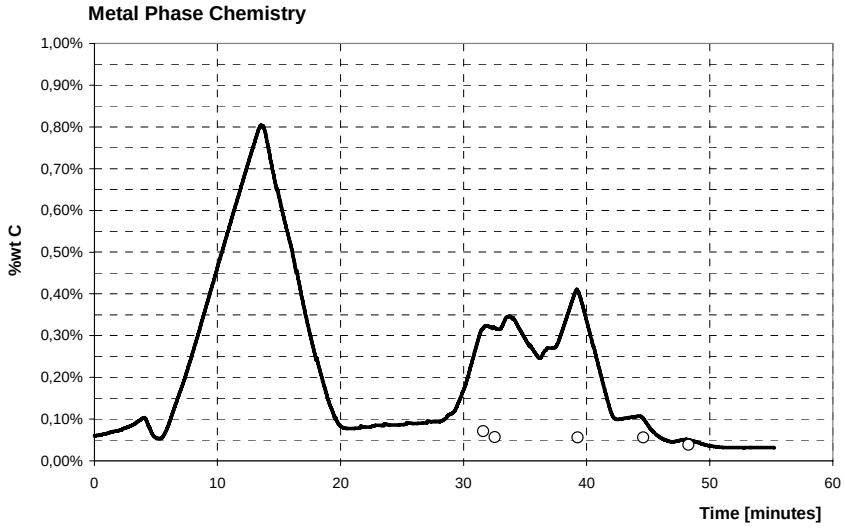

(a) 75137; 42% pig iron

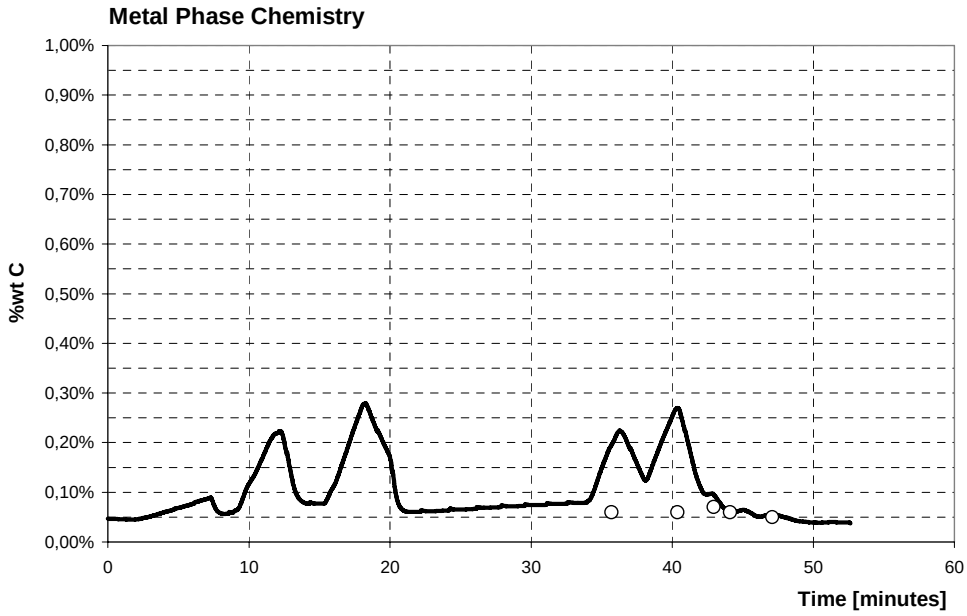

(b) 79727; 30.4% pig iron

Figure 80 – Model prediction for %wt carbon content (line) and experimental data (dots) along the heats (a) 75137, 42% pig iron; (b) 79727, 30.4% pig iron.

Carbon and oxygen injection obviously affect the soluble carbon content in the metal phase. In addition, the pig iron melting rate has also significant effect on carbon content along the processing time. Such effect is pointed out in Figure 81 (a) and (b), where two different pig iron melting rates were applied and the carbon content was computed, resulting in very different prediction patterns. Figure 81 (a) present unsuitable relation with the measured carbon content (expected pattern - dotted), (b) was result of the GRG optimization. Figure 81 (c) simulates the worse effect of changing arbitrarily the critical carbon computed by the GRG of 0.36% to 0.10%.

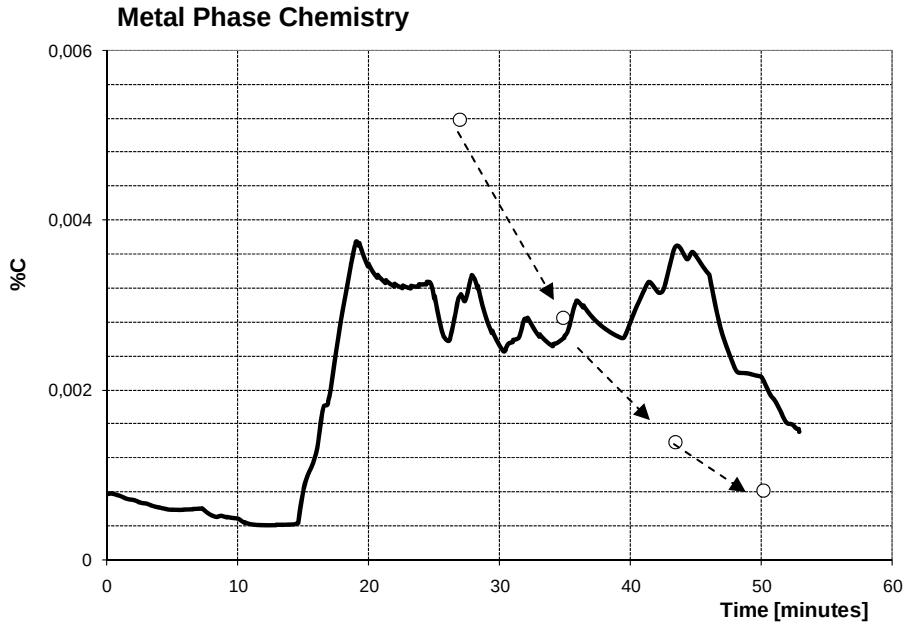

(a) 2356 [kg/min]; $\%C^{Cr}$ 0.36%

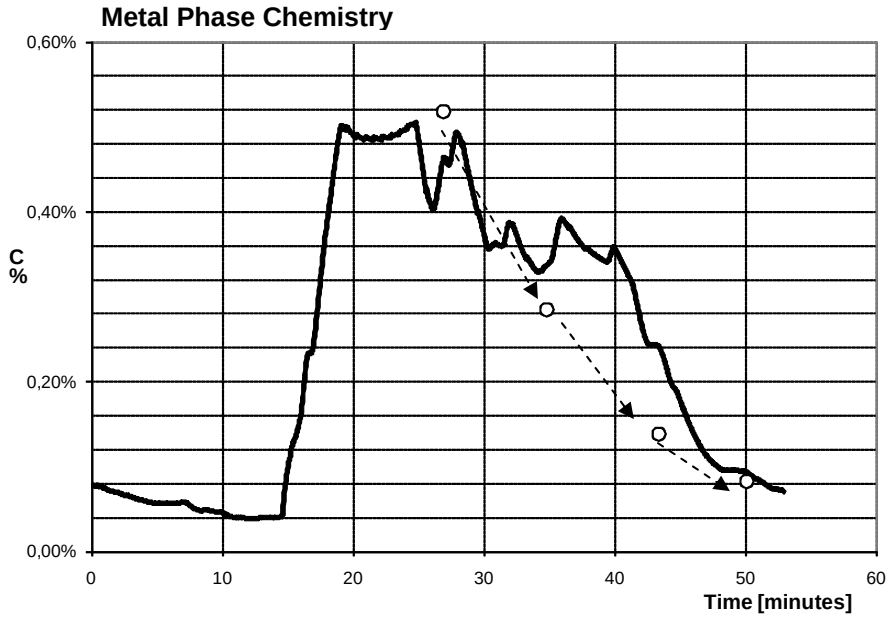

(b) 3529 [kg/min]; %C^{Cr} 0.36%

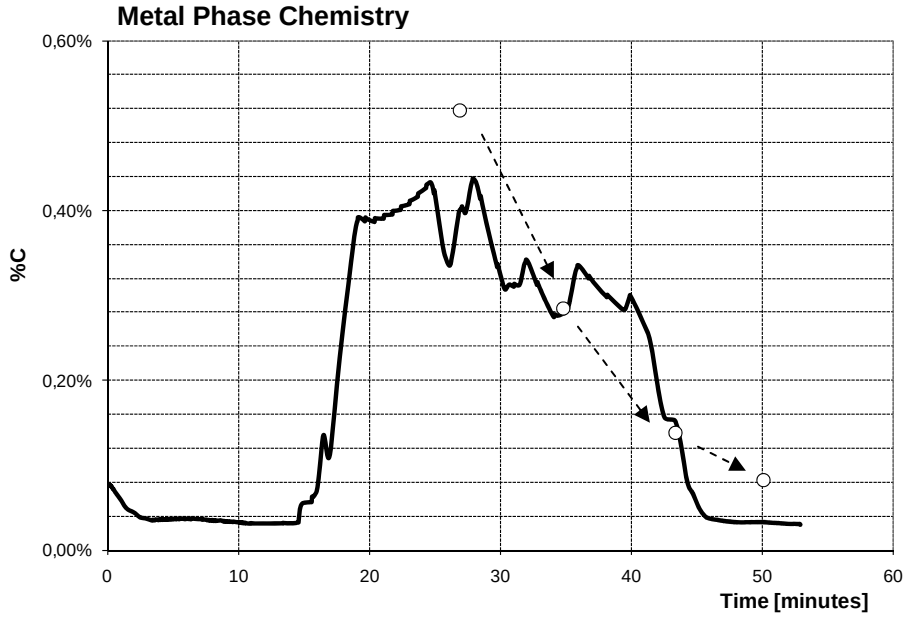

(c) 3529 [kg/min]; %C^{Cr} 0.10%

Figure 81 – Model prediction for %wt carbon content (line) and experimental data (dots) along the heat 80887, 40 % pig iron computed for different pig iron average melting rates (a) 2356 [kg/min], %C^{Cr} 0.36%; (b) 3529 [kg/min], %C^{Cr} 0,36% respectively, and (c) 3529 [kg/min], %C^{Cr} 0,10%.

The decarburization model adopted in this study was not considered to be a stand alone tool. Indeed, decarburization is not a bottle-neck for modern EAF facilities. Actually the major role of the decarburization model is to support the

inverse calculation of melting rates and the net oxygen available to produce iron oxide.

5.1.1.1. Decarburization rate constant

Both decarburization rate constant k_{C1} and k_{C2} represented by equations eq. 174 and eq. 177, respectively, should vary along the heat processing. At EAF, the variation of the reaction interface caused by forced or natural convection, turbulent stirring due to CO evolution, and emulsion intensity result in variation of the decarburization rate constant (k_{C2}) with time. The metal phase weight is increasing according to ferrous materials melting rate in the course of the processing time, hence, it is also influencing the rate constant. Therefore, the decarburization rate constant is somehow an inaccurate description, and is rather to be referred as decarburization rate parameter in this study. Similar approach ha been made for other studies where mass transport affects the reaction rates [23, 26, 31, 72, 87, 92].

$$k_{C1} = c.\frac{MW_C}{W_t^{Metal}}.(1+F_{CO}).100 \qquad \text{eq. 174}$$

$$k_{C2} = \frac{\rho^{Melt} m_C A}{W_t^{Metal}} \qquad \text{eq. 177}$$

Figure 82 presents an example of k_{C1} and k_{C2} computed by the model: (i) linear and non-linear rates are alternated according to the available soluble carbon and oxygen flow rate; (ii) both parameters decrease with time; (iii) ups and downs were caused by switching off the oxygen injection for sampling metal and slag phases. From now on, an average of both parameters is computed for the period of time corresponding to the half molten charge up to full molten charge conditions.

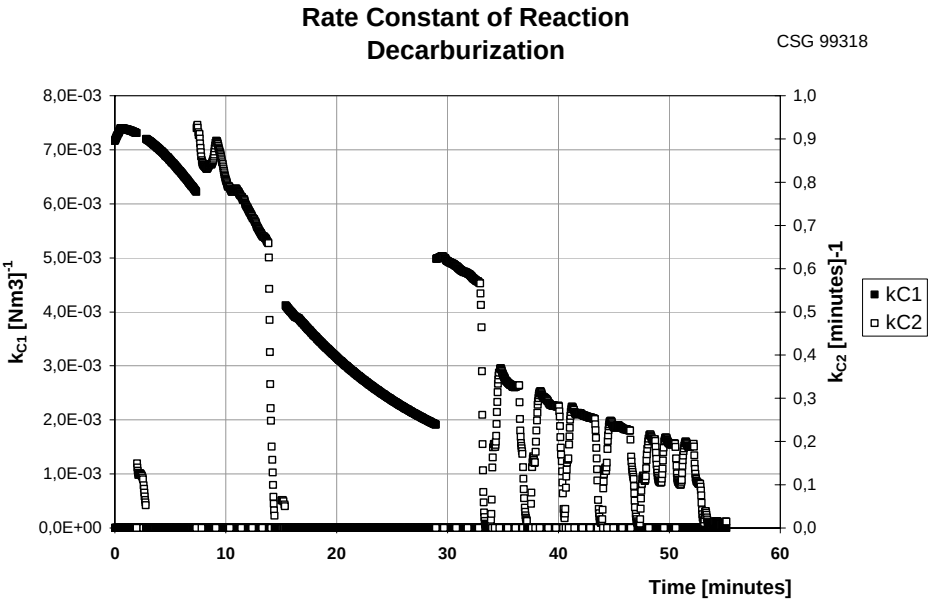

Figure 82 – Computed rate parameter of decarburization reaction (heat 99318). The rate parameters for decarburization are excluding each other. The critical carbon content determines what rate controlling mechanism is predominant at every time *t*, and consequently, k_C is switched accordingly. k_{C1} depends on oxygen flow rate and k_{C2} is governed by carbon diffusion, metal phase weight and the driving force $[\%C]_t - [\%C]^{eq}$.

It has been expected that the rate parameter of decarburization should be lower for EAF when compared with OSM, since the rate is reported faster for OSM. This assumption was not confirmed in this present work when the rate parameter of decarburization is normalized to oxygen flow rate "$m_C.A/Q_{O_2,t}^{L^*}$" as shown in eq. 208. It was found to be 0.098 (0,089 – 0,179), which is agreement with the range of 0.061 to 0.153 achieved for EAF of 40 t and 100 t [30], respectively. Actually, below the critical carbon content, "$m_C.A$" is assumed to be a function of $Q_{O_2,t}^{L^*}$, and it is expected that, whenever the oxygen flow rate increases, "$m_C.A$" should increase too. This increase is due to higher values for both m_C and *A*, because the turbulence is enhanced and larger slag-metal surface is created. Apparently, the present data is pointing out that "$m_C.A$" increases faster than $Q_{O_2,t}^{L^*}$, resulting in lower $[\%C]^{Cr}$. For example, the value of "$m_C.A/Q_{O_2,t}^{L^*}$" for a BOF was found as 0.050 and its correspondent critical carbon content was calculated as 0.3 mass% [97].

$$\frac{m_C.A}{Q_{O_2,t}^{L^*}} = \frac{2.\left(c.\frac{MW_C}{\rho}\right).}{[\%C]^{Cr}} \qquad \text{eq. 208}$$

The slag-metal surface is affected by the number and size of gas bubbles produced by the oxygen injectors. Usually, the oxygen injector technology is quite different for EAF compared to OSM. The current configuration consisting of three to five injectors located at different sites, contribute to increase the interface available for decarburization reaction. Besides, the co-existing solid ferrous materials submerged in the hot heel could also works as additional interface for reaction.

Figure 83 presents the correlation found between the decarburization rate parameter and critical carbon content for different experimental conditions. Almost 70% of the heats fitted fairly well when critical carbon content was in the range of 0.10% to 0.20%. Examining the operational data, no definitive causes were clearly associated to explain the variation in the range of 0.10% to 0.50%. A comprehensive round up on 21 Japanese OSM facilities pointed out %wt critical carbon content variation in very wide range of 0.1% to 1.2% [1].

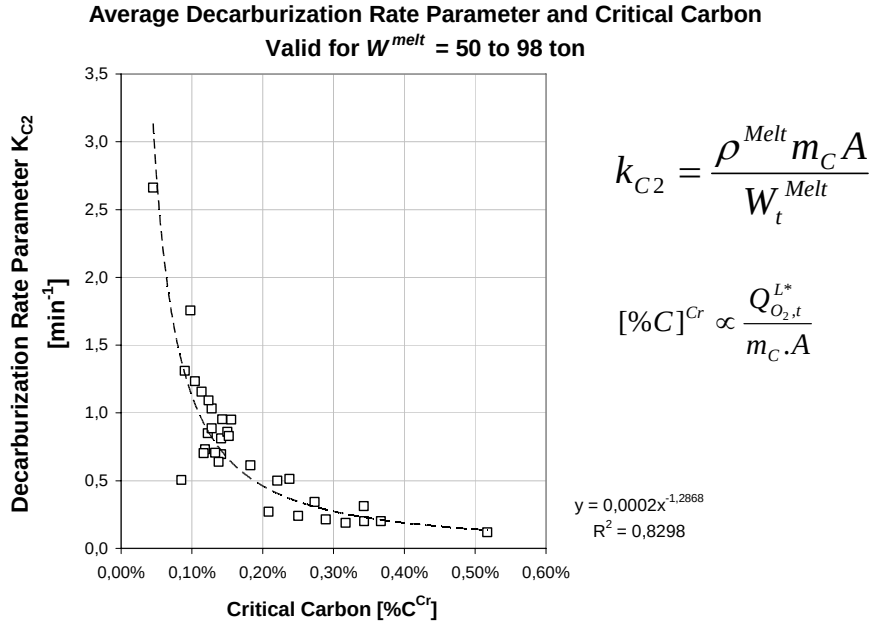

Figure 83 – Rate parameter of decarburization and critical carbon content. k_{C2} is computed as an average.

Since the critical carbon content and its transition time are properly estimated, obvious savings from iron oxidation as well of the oxygen consumption

may be obtained. For high productivity EAF, usually the oxygen flow rate through the lancing mode is kept almost constant along the refining step, and somehow, the over oxidation rate can be partially compensated by carbon injection. The present model could be a promising tool to help the operators to change the operational procedure according to the iron oxidation prediction.

5.1.2. Silicon and Phosphorus oxidation

Raw materials contain other species that influence the oxygen, metal and slag phases' mass balances. Even though in less extent than carbon (20-30 kg/ton), silicon (1-4 kg/ton) can shift the slag pattern. Manganese (4-5 kg/ton) and phosphorus (0.5-1 kg/ton) have a minor effect, many times negligible.

5.1.2.1. Desiliconization

As discussed earlier, the computed silicon content in the metal phase is low along the heat and very low just before tapping, what is in agreement with the sample analysis and ThermoCalcTM estimates. The desiliconization process is very fast, and the pig iron melting rates seemed to be too slow to provide silicon content build up in the metal phase higher than 0.07%. Figure 84 presents estimates for carbon and silicon contents (a) after the GRG reached the optimum equations solution, and shows (b) once again the pig iron melting rate clearly influencing both carbon and silicon contents in the metal phase. By decreasing the pig iron melting rate, the peaks of both soluble carbon and silicon are delayed in time; as well (c) the variation of critical silicon shifts the silicon content prediction.

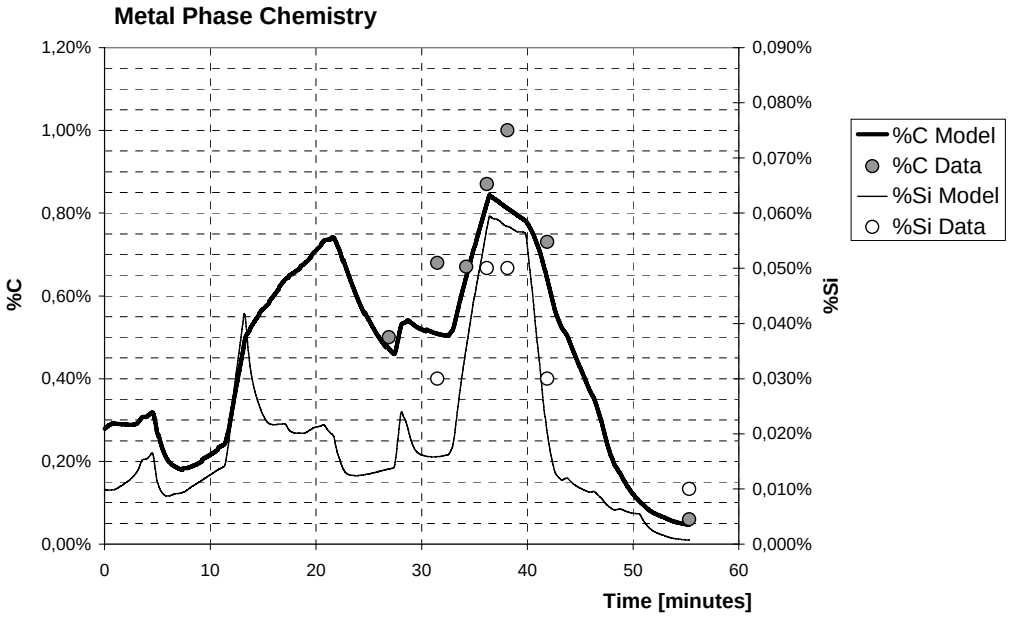

(a) 2693 [kg/min]; $\%Si^{Cr}$ 0.15%

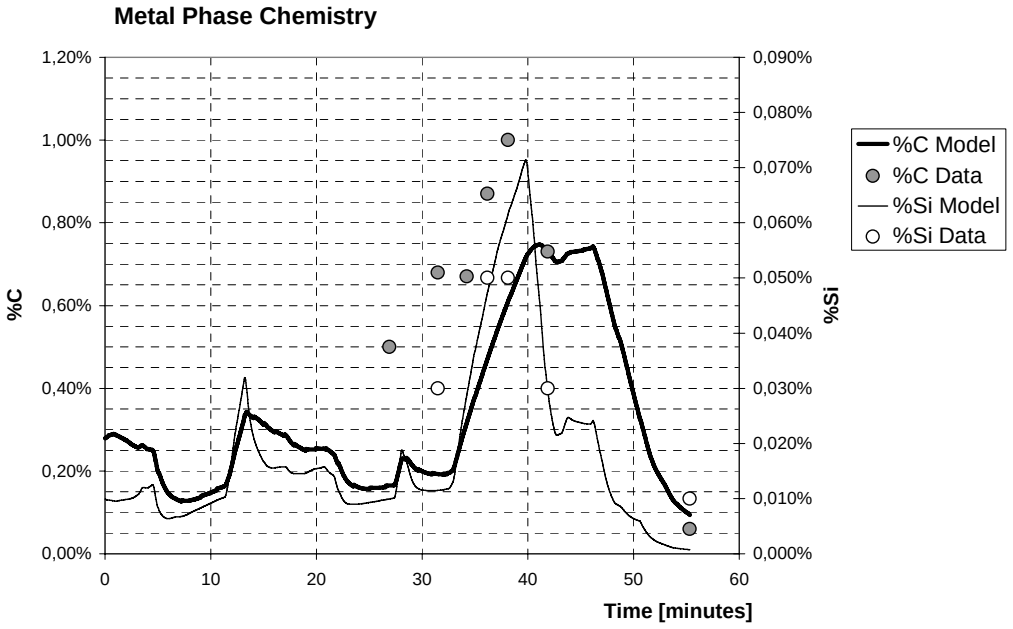

(b) 1675 [kg/min]; $\%Si^{Cr}$ 0.15%

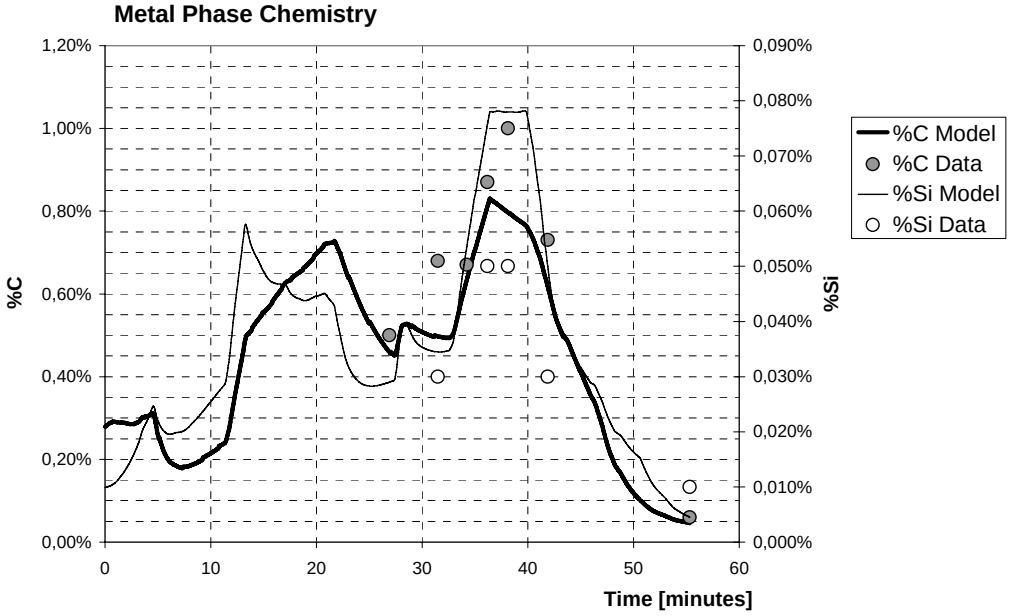

(c) 2693 [kg/min]; %Si^{Cr} 0.35%

Figure 84 – Model prediction for %wt carbon and silicon content (line) and experimental data (dots) along the heat 80887, 40 % pig iron (a) 2693 [kg/min], %Si^{Cr} 0.15% ; (b) 1675 [kg/min], %Si^{Cr} 0.15%; (c) 2693 [kg/min], %Si^{Cr} 0.35%

The current study estimated an average of %wt Si^{Cr} 0.13%, and the rate constant of desiliconization normalized to oxygen flow rate "$m_{Si}.A/Q_{O_2,t}^{L^*}$ resulted in an average of 0.115. According to the decarburization and desiliconization models adopted, carbon and silicon react with FeO and share the same interface of reaction. When both carbon and silicon are below their critical contents, the ratio of rate parameters can be described by combining $k_{C2} = \frac{\rho^{Metal} m_C A}{W_t^{Metal}}$ (eq. 177) and $k_{Si2} = \frac{\rho^{Metal} m_{Si} A}{W_t^{Metal}}$ (eq. 188),

$$\frac{k_{C2}}{k_{Si2}} = \frac{m_C A}{m_{Si} A} \qquad \text{eq. 209}$$

combining eq. 181 and eq. 191,

$$\frac{k_{C2}}{k_{Si2}} = \frac{c.\frac{MW_C(1+F_{CO}).Q_{O_2,t}^{L^*}}{\rho^{Metal}.\left([\%C]^{Cr}-[\%C]^{eq}\right)}}{c.\frac{MW_{Si}.Q_{O_2,t}^{L^*}}{\rho^{Metal}.\left([\%Si]^{Cr}-[\%Si]^{eq}\right)}} = \frac{2.MW_C}{MW_{Si}}.\frac{\left([\%Si]^{Cr}-[\%Si]^{eq}\right)}{\left([\%C]^{Cr}-[\%C]^{eq}\right)} \qquad \text{eq. 210}$$

for simplification, it is assumed that $[\%C]^{eq},[\%Si]^{eq} \approx 0$, thus

$$\frac{k_{C2}}{k_{Si2}} = \frac{2.MW_C}{MW_{Si}} \cdot \frac{[\%Si]^{Cr}}{[\%C]^{Cr}} \qquad \text{eq. 211}$$

An example of the product *"m_i.A"* for decarburization versus desiliconization is presented in Figure 85.

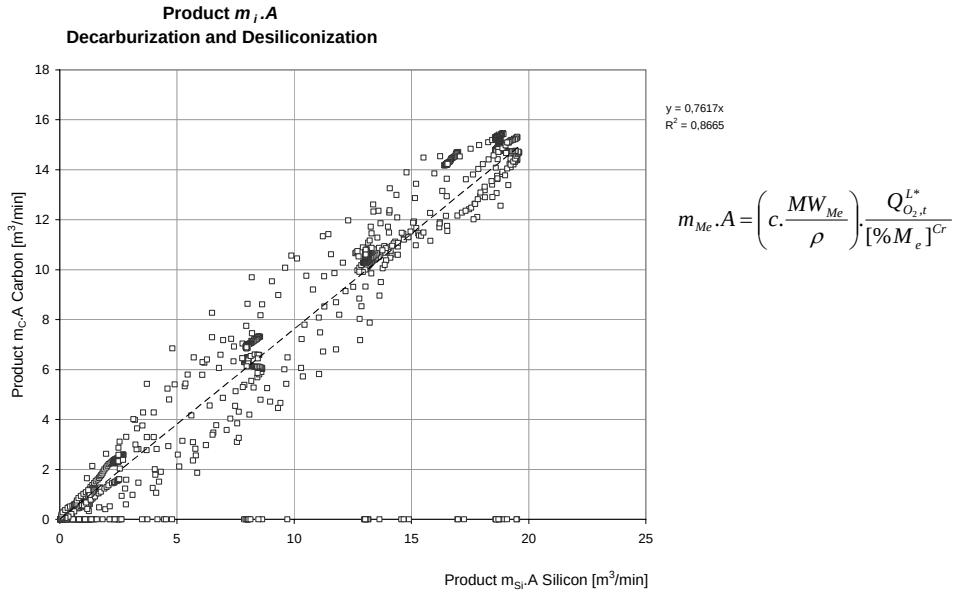

Figure 85 – Model prediction for product *"m_i.A"* along the heat 80882 processing time

Figure 86 and Figure 87 show the ratio of rate parameters and the critical contents computed for decarburization and desiliconization. The ratio k_{C2}/k_{Si2} was found around 0.81.

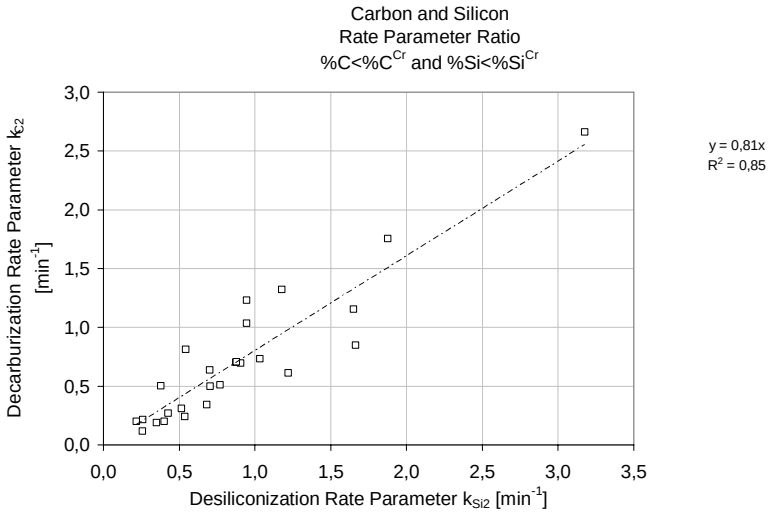

Figure 86 – Model prediction for decarburization and desiliconization rate parameters.

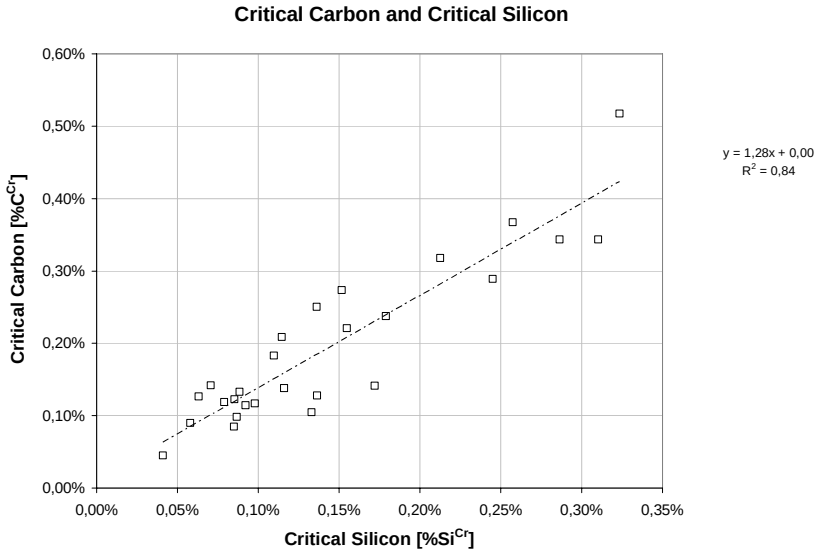

Figure 87 – Model prediction for critical carbon and silicon contents

Actually, according to the boundary layer theory, mass transfer coefficients of carbon and silicon in the liquid iron phase maybe also evaluated based on diffusivities ratio. Additionally, other relations have been proposed for liquid phase mass transfer coefficient for the regime of surface renewal at the gas-liquid interface [9], according to eq. 212.

$$N_i \propto \frac{D_i}{\delta_C} \qquad \text{eq. 32}$$

$$k_i \propto D_i^{1/2} \qquad \text{eq. 212}$$

The estimated k_{C2}/k_{Si2} in this study is good agreement with observed ranges elsewhere [98]**,** considering literature data as presented in Table 22.

Table 22 – Carbon and silicon diffusivity in liquid iron at 1873, according to References (i) [9] and (ii) [98].

Ratio k_{C2} / k_{Si2} Model Avg

	Ref (i)	Ref (ii)			
		Calculated	Observed		
			min	max	
D_C	7,80E-05	4,80E-05	2,00E-05	2,00E-04	cm^2/s
D_{Si}	3,80E-05	6,00E-05	2,50E-05	1,20E-04	cm^2/s
(D_C / D_{Si})	2,05	0,80	0,80	1,67	
$(D_C / D_{Si})^{1/2}$	1,43	0,89	0,89	1,29	

5.1.3.
Dephosphorization

Similarly to carbon and silicon, the GRG algorithm works out simultaneously the prediction for other species which are influenced by the pig iron and scrap melting rates, as well the amount of oxygen delivered to the furnace. In order to improve the estimates for rate parameters of decarburization and iron oxide reduction reactions, phosphorus was initially selected as an additional tracer for pig iron melting rate prediction, since pig iron presented high phosphorus content (%wt 0.08-0.12%). Meanwhile, dephosphorization has proved to be as complex or more than decarburization reaction appeared to be. The thermodynamics and empirical models applied to slag as well the kinetic models demanded a lot of effort to adjust the model parameters properly. Instead of a secondary indicator only, the value of this tracer made its prediction as important as carbon.

Figure 88 shows some typical model prediction for both %wt carbon and phosphorus content in the metal phase and the corresponding metal samples chemistries. Three heats were taken as examples, with pig iron charge varying in the range of 8% to 40% and different oxygen consumption.

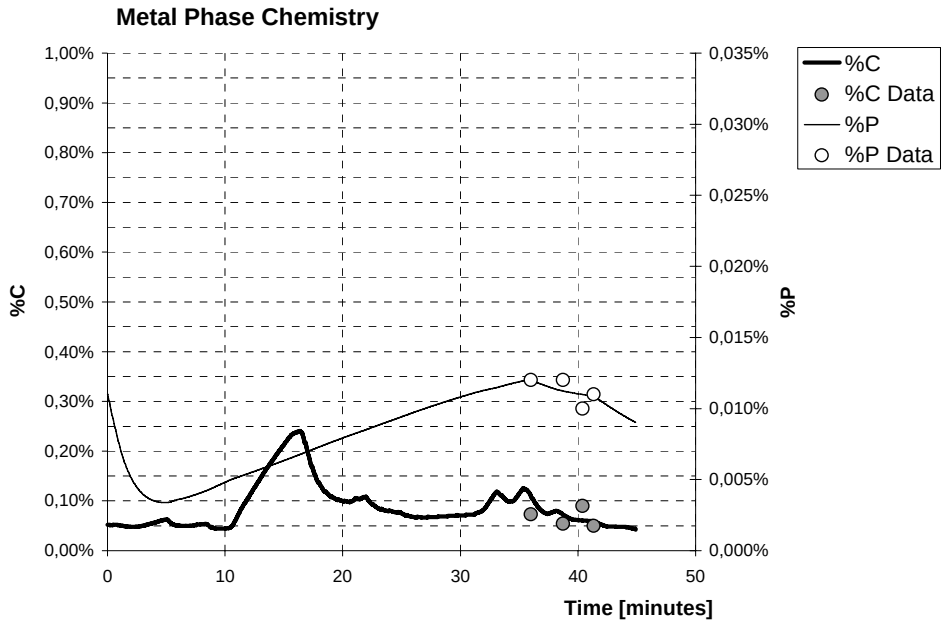

a) heat 80882, 8% pig iron

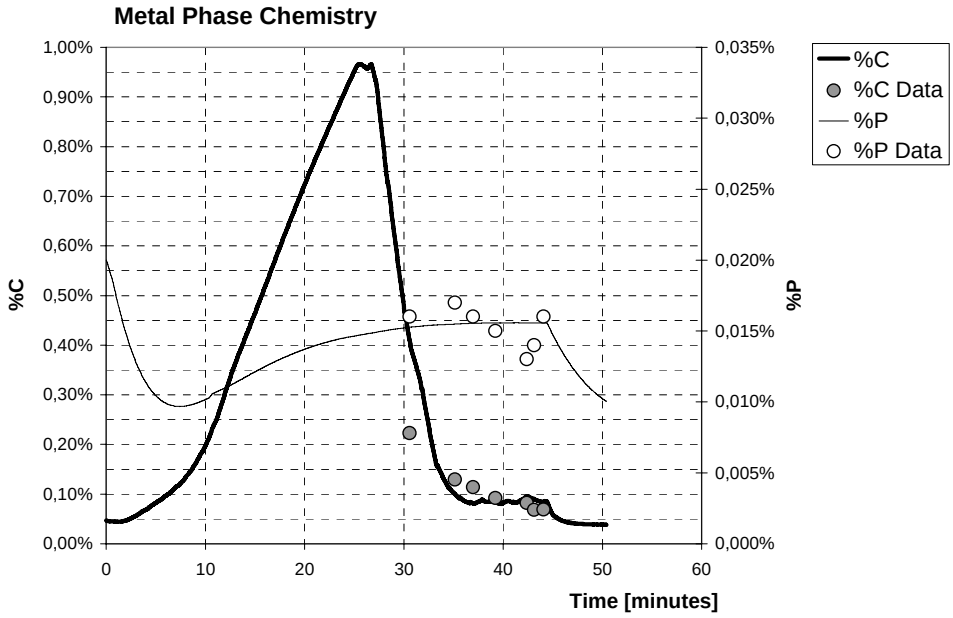

(b) heat 80120; 30% pig iron

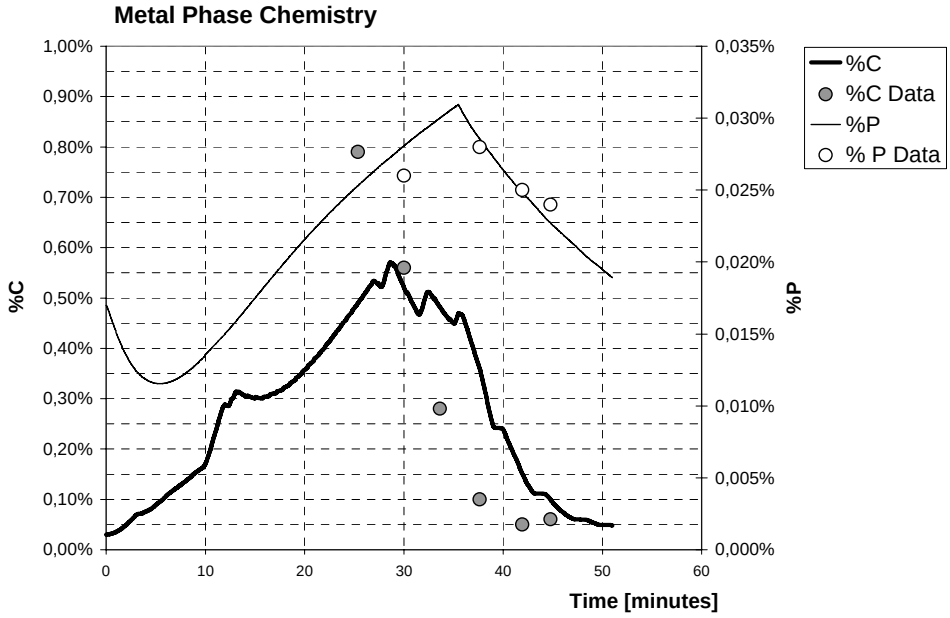

(c) heat 104428; 40% pig iron

Figure 88 – %wt Phosphorus and carbon evolution for (a) heat 80882, 8% pig iron; (b) heat 80120, 30% pig iron; (c) heat 104428, 40% pig iron. The discrete points are actual furnace melt chemistries

The phosphorus content profile along the processing time was lower for low pig iron charge and for heats with higher oxidation degree, indicated at this point, being proportional to FeO content in the slag. As expected, the carbon content peaks were evident for higher pig iron charge. Additionally, Table 23 describes briefly some of the variables supporting the model for these particular heats.

Table 23 – Summary of operational data for heats 80120, 80882 and 104428

				Heats		
				80120	**80882**	**104428**
Dephosphorization	Dephosphorization Parameter average 50-100 ton	k_P	[min^{-1}]	0,145	0,095	0,048
Raw Materials & Slag	Pig Iron Chemistry	*%C pig iron (v)*	[%]	4,2%	4,5%	4,2%
		%Si pig iron (v)	[%]	1,0%	1,1%	0,5%
		%P pig iron (v)		0,12%	0,12%	0,12%
	Carbonaceous Materials - Injection Yield	n_{CMat}	[%]	95%	98%	94%
	Slag generated		[ton]	11,1	12,9	12,7
	Carbon Injected + Ferrous Blend		[kg/ton]	21	19	33
	Mix Density		[ton/m3]	0,75	0,64	0,89
Melting Rates	Pig Iron		%	30%	8%	40%
	Max Pig Iron Melting Rate		[kg/min]	1.423	579	2.999
	Max Scrap Melting Rate		[kg/min]	2.631	4.919	4.163
	Total Melting Rate		[kg/min]	2.275	4.566	3.695
Oxygen Consumption	Total		Nm3/t	43,9	42,4	55,2
Lancing Mode	Oxygen consumption for		Nm3/t	25,0	23,9	28,3
	FeO -> CO, SiO2, MnO		Nm3/t	18,9	9,3	21,2
	FeO remaining after reactions with carbon		Nm3/t	5,5	13,1	7,0
	Off-gas		Nm3/t	0,6	1,5	0,2
Burning Mode	Burners		Nm3/t	12,7	13,2	18,2
PC Mode	Oxygen consumption for		Nm3/t	6,2	5,3	8,7
	FeO -> CO, SiO2, MnO		Nm3/t	0,6	0,5	0,9
	Post combustion (CO->CO2)		Nm3/t	0,7	1,2	3,0
	FeO remaining after reactions with carbon		Nm3/t	2,9	1,4	3,4
	Off-gas		Nm3/t	1,9	2,1	1,5

Examining this data, it can be noticed that the ratio carbon/lancing oxygen input is higher for heat 104428, but it is almost the same for heats 80882 and 80120. The slag formers additions were quite the same too, but the oxygen profiles were different for all of them. Therefore, the understanding of such multiple reactions is not that simple, and should not be limited to computing the overall consumption figures. The long transient period during solid charge EAF processing makes such analysis very dependent on ferrous materials melting rate, which cannot be measured up to now in industrial scale. Hence, the carbon and phosphorus contents in the metal phase, as well the FeO content in the slag phase along the time are valuable indicators of ferrous charge melting rates. One way to estimate this information is applying kinetic models for decarburization and dephosphorization, as coupled reactions, sharing roughly the same sources of oxygen. Figure 89 presents the continuous slag phase chemistry prediction, and the measured chemical composition.

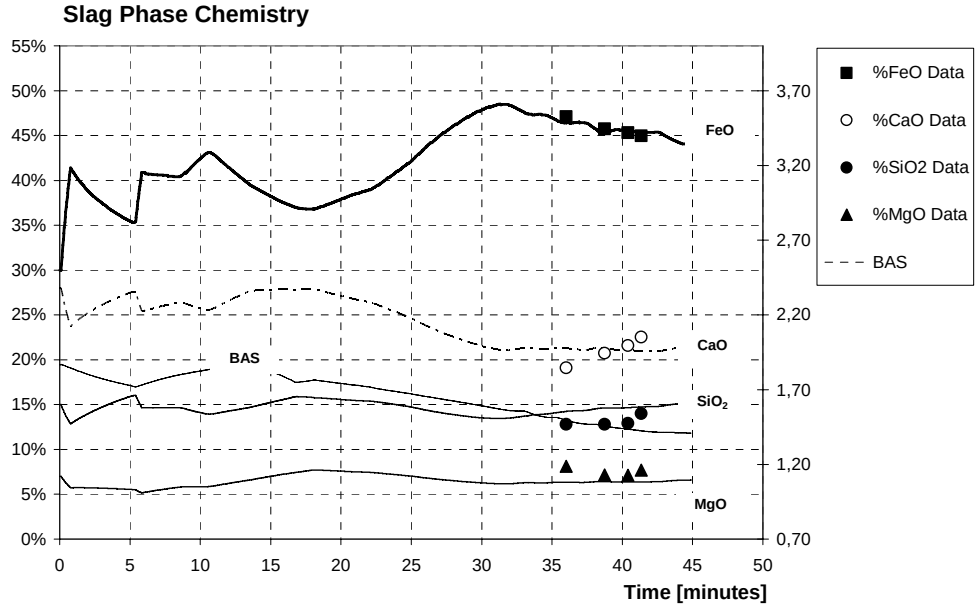

(a) heat 80882, 8% pig iron

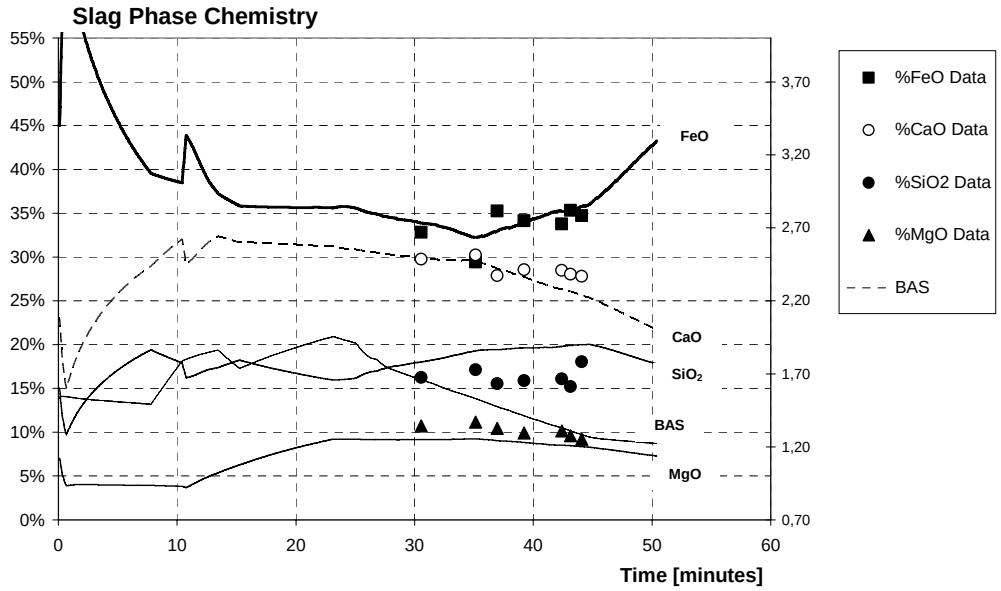

(b) heat 80120, 30% pig iron

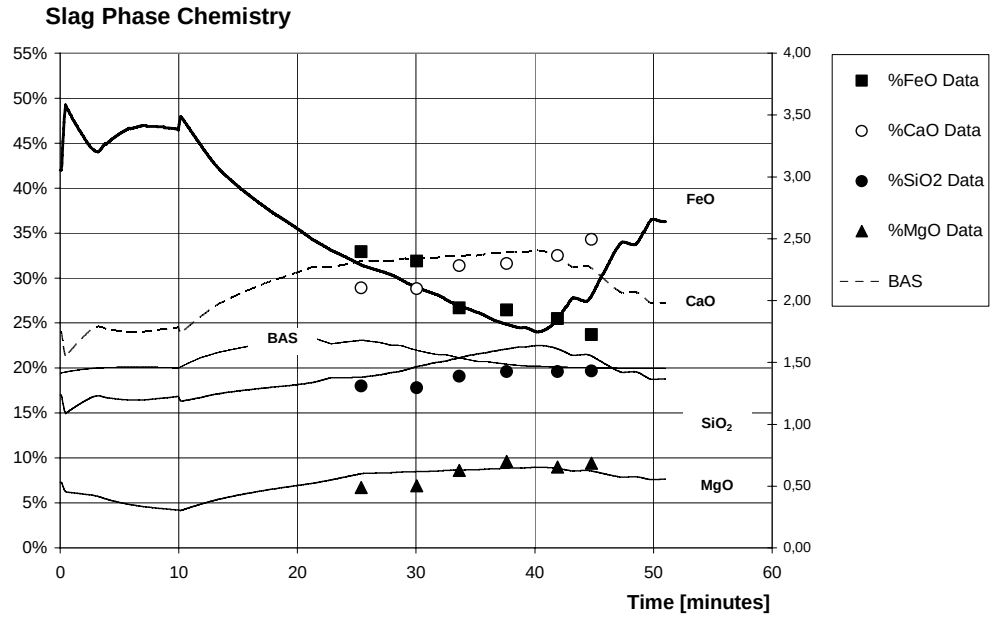

(c) heat 104428; 40% pig iron

Figure 89 – Slag chemical composition predicted by the model and measured %wt chemistry (discrete points): (a) heat 80882, 8% pig iron;(b) heat 80120, 30% pig iron; (c) heat 104428, 40% pig iron

In the beginning of the meltdown stage, phosphorus content tends to decrease, favored by high CaO and FeO content in the remaining slag produced in the previous heat, and also by the new lime and dololime charged in the first and second buckets. Another source of FeO is the impurities entrapped in the scrap and pig iron in limited extent, but contributing to dissolve the new slag formers charged. Part of this mass is carried to the off-gas system. The slag balance will be detailed in sessions 5.1.5. Iron Oxide Reduction and 5.1.6. Initial slag amount.

Moreover, the initial L_P was in order of 100-200, which is very high, and besides, low phosphorus content scrap was computed to melt faster than high phosphorus content pig iron. Therefore, the dissolution rate of phosphorus followed the pig iron melting rate. As long as pig iron melting proceeds, phosphorus is delivered to the metal phase, and its content increases because the computed dephosphorization rate was slower than the phosphorus dissolution rate. Later, the partition of phosphorus L_P decreases by the end of refining time, due to the decrease of CaO content in the slag and to the rapid increase of temperature shown in Figure 90. The expected decreasing in dephosphorization rate by the end of heat is somehow compensated by the

increasing of FeO content in slag, and mainly by the end of active source of phosphorus. Pig iron, as the major source of phosphorus, was completely molten according to estimates in Figure 91. The L_P even though low, is still high enough to provide late dephosphorization without competition with phosphorus dissolution. For instance, heat 104428 was estimated to have the pig iron charge completely molten around 35 minutes. Figure 88 (c) presents an inflexion point at the same time.

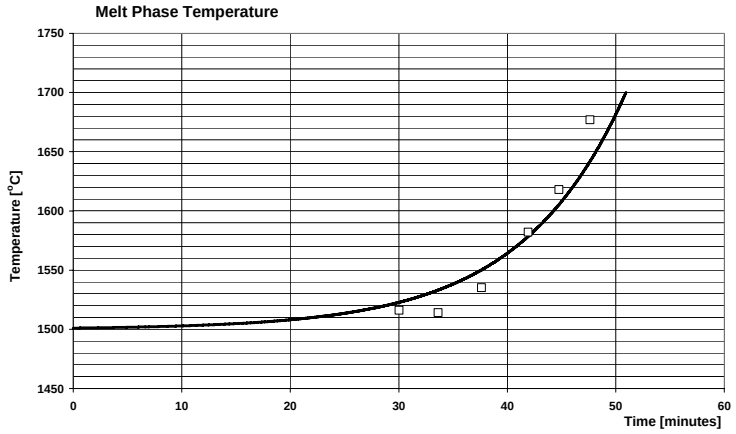

Figure 90 – Temperature profile along the heat 104428 processing time.

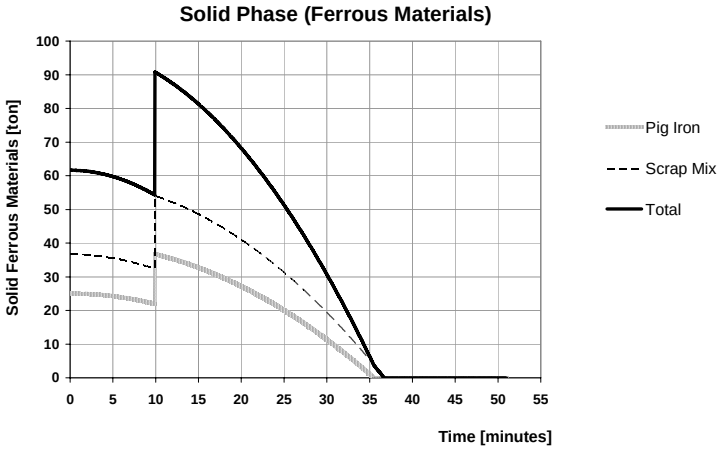

Figure 91 – Estimated solid phase (pig iron + scrap mix) evolution along the heat 104428

Figure 92 summarizes the relation predicted by the current model for soluble %wt carbon-oxygen content in the metal phase and the FeO content evolution in slag for heat 104428. Besides the dissolution of carbon from pig iron, significant amount of coke was injected in the period of 20 to 40 minutes, and consequently, influencing on FeO reduction reaction. The inflection point for

phosphorus was reported around 35 minutes. After this point, the oxygen content increases fast because the oxygen supply is higher than the carbon transport to the interface of reaction. Consequently, the FeO content in the slag phase and soluble oxygen in the metal phase also increase to accommodate such excess of oxygen supply.

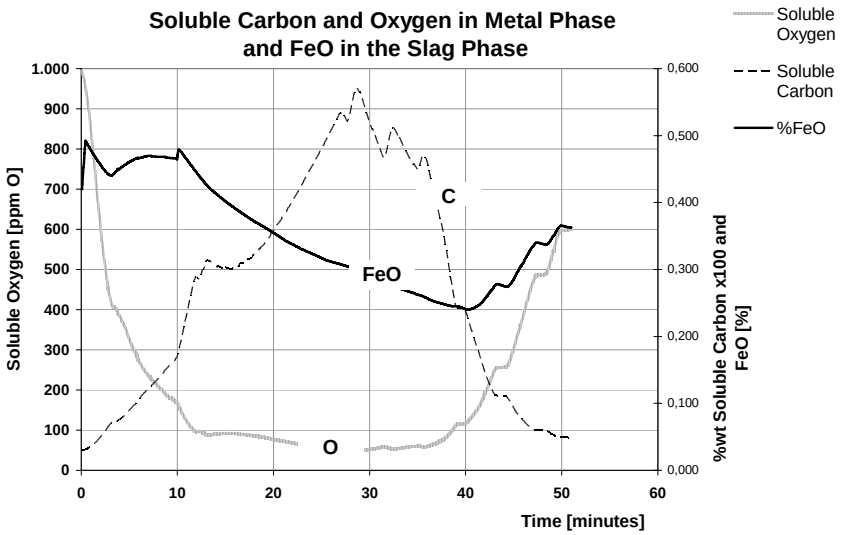

Figure 92 – Model prediction for soluble carbon and oxygen in the metal phase and FeO content in the slag phase. (Heat 104428)

The estimates for rate parameters of dephosphorization were possible by reverse calculation, based on the samples chemistry of both metal and slag phases and mass balance along the processing time. Thermodynamic and kinetic assumptions were made based on models developed elsewhere [72, 82-87], and earlier described by eq. 193 and eq. 194.

$$\left.\frac{d[\%P]_t}{dt}\right| = r_t^{P-Oxi} = -k_P.([\%P]^{\infty} - [\%P]^{eq})$$

$$[\%P]^{eq} = \frac{(\%P)}{L_P} \qquad \text{eq. 193}$$

$$k_P = \frac{\rho^{Metal} m_P^* A}{W_t^{Metal}} = \frac{\rho^{Metal} A}{W_t^{Metal}} \frac{1}{\left(\frac{\rho^{Metal}}{k_P^{Slag}.\rho^{Slag}.L_P} + \frac{1}{k_P^{Metal}}\right)}$$

$$m_P^* = \frac{1}{\left(\frac{\rho^{Metal}}{k_P^{Slag}.\rho^{Slag}.L_P} + \frac{1}{k_P^{Metal}}\right)} \qquad \text{eq. 194}$$

Previous work conducted at industrial EAF facilities, where significant amount of HBI was blended to scrap [72], found that $m_P^* A$ increased with time. This unexpected behavior was computed by rearranging eq. 193 into eq. 213,

$$\left(m_P^* A\right)t = \frac{W_t^{Melt}}{\rho^{Melt}} \sum_n \int \frac{([\%P]_n^{\infty} - [\%P]_n)}{([\%P]_{n+1}^{\infty} - [\%P]^{eq})} d[\%P] \qquad \text{eq. 213}$$

Integrating eq. 213 numerically, the slope of the curve shown in Figure 93 at any time corresponds to "$m_P^* A$" estimates, where Σ is the right hand of the equation shown above.

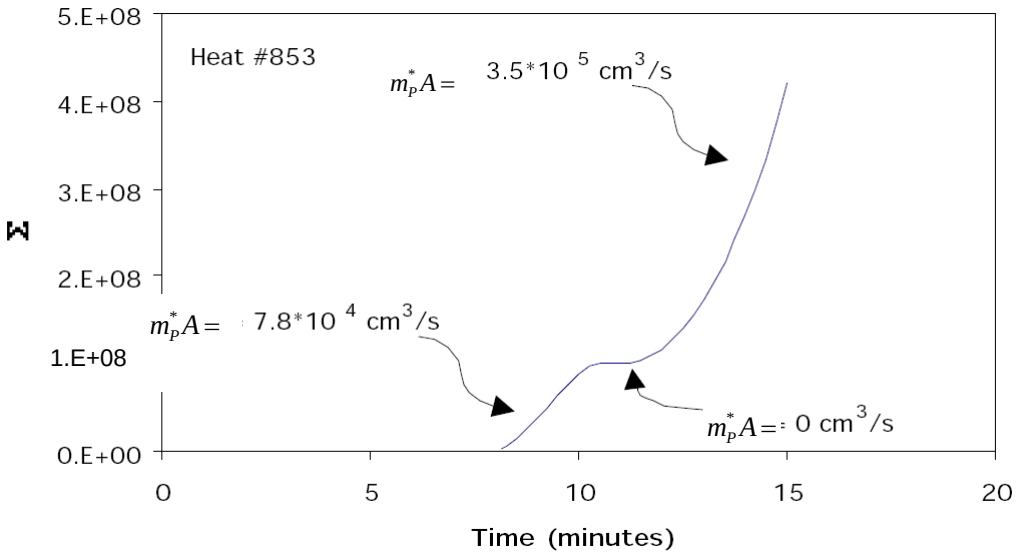

Figure 93 – Estimate of $m_P^* A$ for another EAF facility [72]

It could be seen that, in this particular study [72], "$m_P^* A$" increased more than four times along the heat processing time. Such behavior was connected to the temperature increasing and, consequently, slag viscosity decreasing with time. Besides, the co-existing solid phase in the hot heel could create barriers inhibiting fluid flow in the earlier meltdown stage. Later, the oxygen flow rate was increased by 30% during refining period, probably influencing the stirring effect.

In the current study, an exponential function was proposed to allow the product $m_P^*.A$ to be dependent on processing time, in order to accommodate the variations just described above,

$$m_P^*.A = a.e^{+b.t} \qquad \text{eq. 214}$$

However, the trend of "$m_P.A$" to increase with processing time did not work well for all dephosphorization rate prediction, and a constant dependence of product "$m_P^* A$" with time fitted better instead. Figure 94 presents the plot of L_P, "$m_P^* A$" and k_P for the same heats 80882, 80120 and 104428. The L_P shows similar profile, k_P decreases with time behavior for all heats, but "$m_P^* A$" varied: heats (a) and (c) show an independence with time and corresponded to 81% of the observed heats; case (b) represents only 19% of the heats.

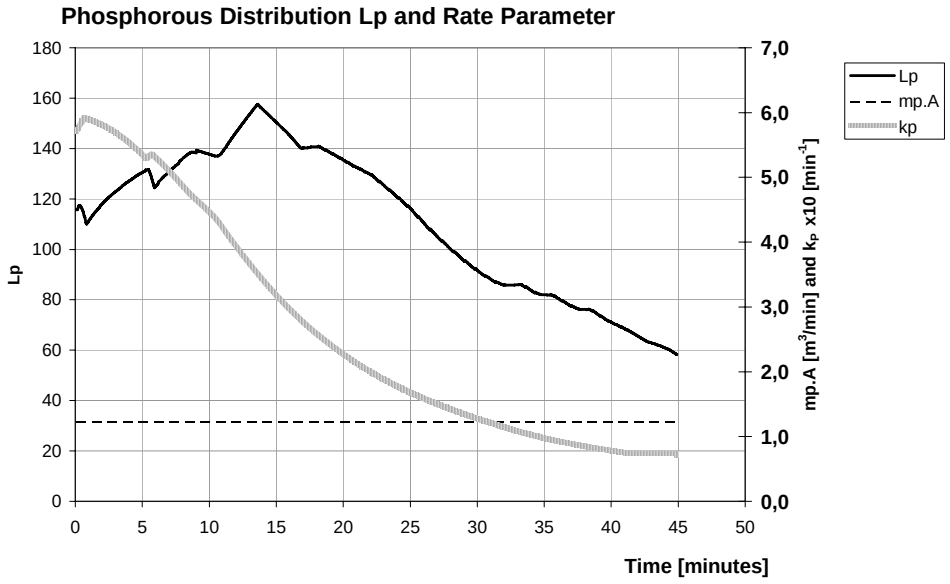

(a) heat 80882; 9% pig iron

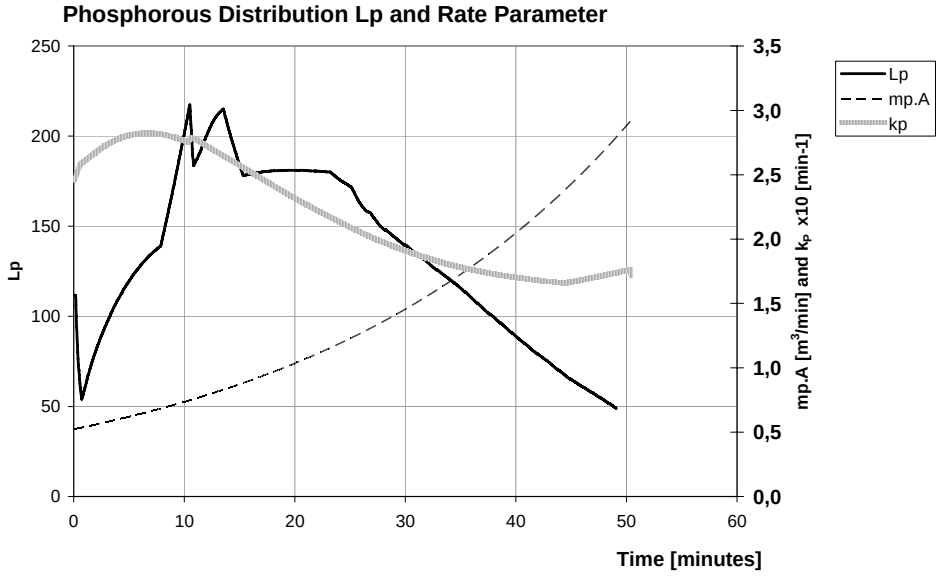

(b) heat 80120; 30% pig iron

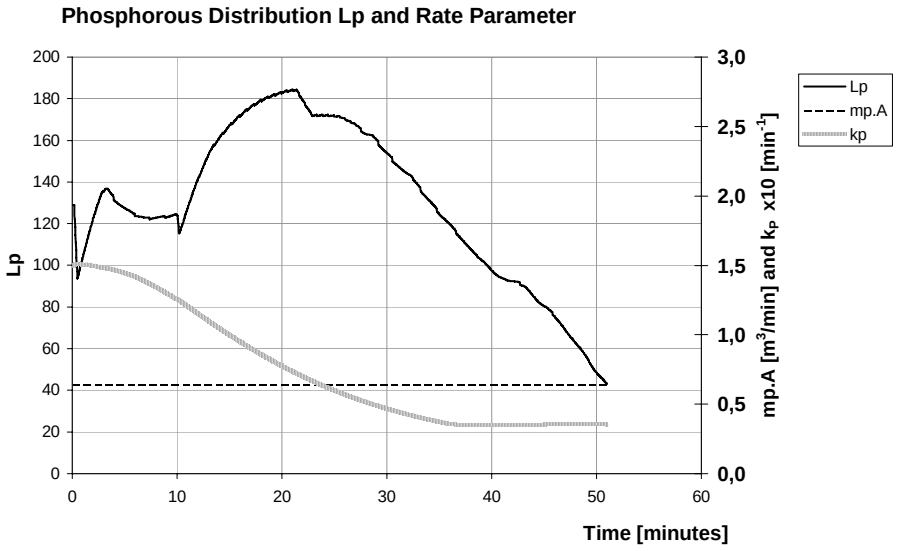

(c) heat 104428; 40% pig iron

Figure 94 – Phosphorus distribution L_P, product $m_P^* A$, and overall dephosphorization rate parameter k_P: (a) heat 80882, 9% pig iron (b) heat 80120, 30% pig iron; (c) heat 104428, 40% pig iron

The dephosphorization rate parameter for the whole set of heats observed in this study is plotted in Figure 95. The dispersive appearance is connected to the scheduled different experimental conditions, for example: carbon injection rate, slag foaming performance, as well different oxygen injection profiles. The trend of the overall rate parameter decreasing with time is absolutely predominant.

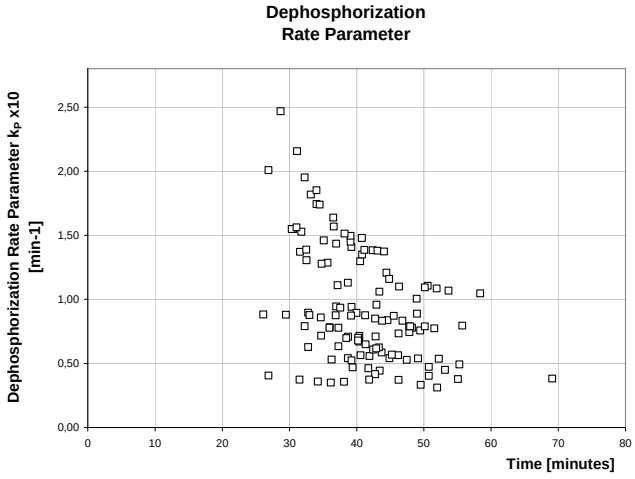

Figure 95 – Dephosphorization rate parameters for all heats vs. time

If decarburization and dephosphorization rate parameters depend on the same extension of reaction interface, and both mechanisms are limited to liquid phase mass transfer, the ratio k_{C2}/k_P should be connected to the diffusivity of phosphorus and carbon.

$$\frac{k_{C2}}{k_P} = \frac{m_C.A}{m_P^*.A} \propto \frac{D_C}{D_P} \qquad \text{eq. 194}$$

The correlation between k_{C2} and k_P presented in Figure 96 encourages to believe that both parameters are connected in agreement with the applied kinetics models.

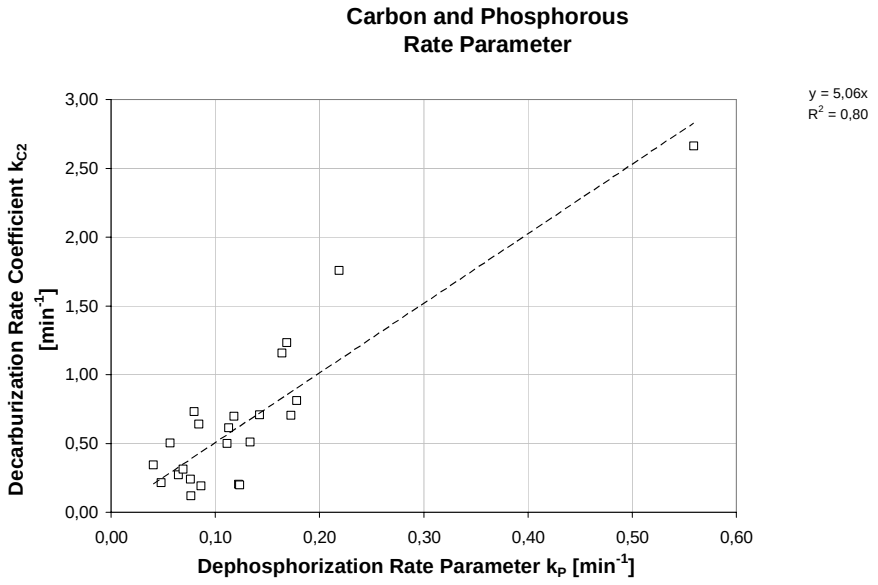

Figure 96 – Decarburization vs. dephosphorization rate parameters

Despite the fact that Figure 96 showed a consistent correlation and the ratio k_{C2}/k_P found is in same order of magnitude, it is at least 3 to 6 times higher than expected, according to data of diffusivity ratio presented in Table 24.

Table 24 – Carbon and phosphorus diffusivity in liquid iron at 1873 reference (i) [9], reference (ii) [98]

Ratio k_{C2} / k_P Model Avg		Ref (i)	Ref (ii)		
			Calculated	Observed	
D_C	cm^2/s	7,80E-05	4,80E-05	2,00E-05	2,00E-04
D_P	cm^2/s	4,70E-05	7,40E-05	2,50E-05	
(D_C / D_P)		1,66	0,65	0,80	
$(D_C / D_P)^{\wedge}1/2$		1,29	0,81	0,89	

Figure 97 presents both model prediction and the equilibrium computed for phosphorus content considering the heat 104429, for instance. The empirical model described earlier by eq. 151 and re-written in terms of P_2O_5 by eq. 215 maybe underestimating the phosphorus in equilibrium for the current operational conditions. Consequently, this would increase the driving force of reaction, decrease the dephosphorization rate parameter and, increase the rate parameter ratio k_{C2}/k_P .

$$\log L_P = \frac{(\%P_2O_5)^{Slag}}{[\%P]^{Metal}} = \left(\begin{array}{l} \frac{10{,}730}{T} + \\ +4.11.\log(\%CaO + 0.15\cdot(\%MgO) - 0.05\%FeO) + \\ +2.5.\log\%FeO + 0.5.\log\%P_2O_5 - 13.51 \end{array} \right) \quad \text{eq. 215}$$

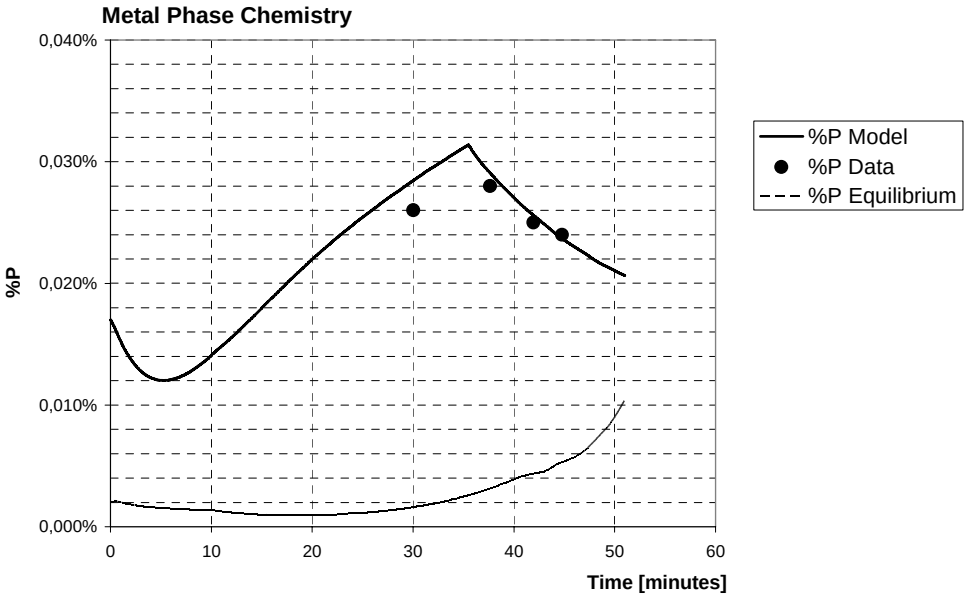

Figure 97 – %wt Phosphorus prediction, measured phosphorus (discrete points) and phosphorus in equilibrium computed for heat 104428.

Re-writing eq. 89 regarding the soluble content of phosphorus and oxygen in liquid iron, eq. 216 and eq. 217 describe the phosphorus oxidation and the equilibrium constant of reaction.

$$2\underline{P} + 5\underline{O} \rightarrow P_2O_{5(l)} \qquad \text{eq. 216}$$

$$K_{P_2O_5} = \frac{a_{P_2O_5}}{h_P^2 \cdot h_O^5} \cong 5.62 \cdot 10^{-12} \qquad \text{eq. 217}$$

The activities of phosphorus and oxygen dissolved in liquid iron are very low, consequently, eq. 217 points out that the activity of phosphorus oxide in slag phase shall be also very low. Therefore, the oxidation of phosphorus directly in the liquid iron should be not realistic, hence, reactions and equilibrium at slag-metal phase interface must be considered to provide low activity of phosphorus oxide [99]. Thus, many empirical models have been proposed to incorporate the influence of other oxides in complex slags created under EAF conditions.

Rearranging eq. 151 in respect to phosphorus equilibrium constant K_P adopted in the present study, the empirical model (Model 1) [72] describing the equilibrium constant can be written according to eq. 218,

$$LogK_P = Log\frac{(\%P_2O_5)}{[\%P]\cdot(\%FeO)^{2.5}} = \qquad \text{eq. 218}$$
$$= \begin{pmatrix} +4.11.\log(\%CaO + 0.15\cdot(\%MgO) - 0.05(\%FeO) + \\ +0.5.\log\%P_2O_5 + \frac{10{,}730}{T} - 13.51 \end{pmatrix}$$

In similar manner, other empirical model (Model 2) proposed by the same author of eq. 218, is described in eq. 219 [82],

$$\log K_P = Log\frac{(\%P_2O_5)}{[\%P]\cdot(\%FeO)^{2.5}} = \qquad \text{eq. 219}$$
$$= \begin{pmatrix} 0.072\cdot\left[(\%CaO) + 0.15\cdot(\%MgO) + 0.6\cdot(\%P_2O_5) + 0.6\cdot(\%MnO)\right] + \\ +\frac{11{,}570}{T} - 10.14 \end{pmatrix}$$

Both of models presume that K_P is not constant when the slag chemical composition changes. Accordingly, the term K_P "Apparent Equilibrium Constant" is proposed. Figure 98 depicts the plot of Model 1's equilibrium prediction for Log K_P as a function of CaO, MgO, FeO and P_2O_5,

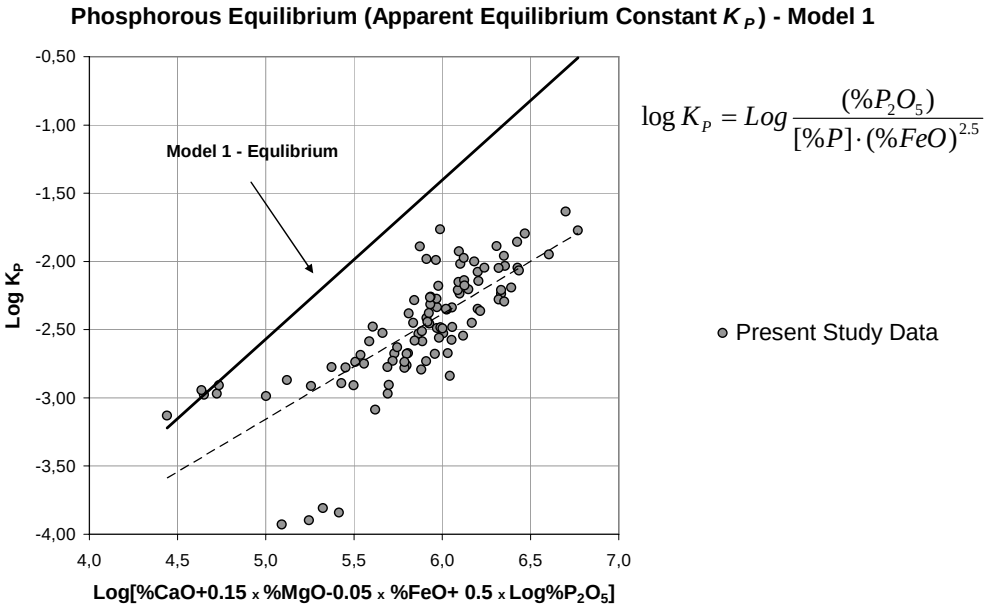

Figure 98 – Model 1 Log K_P *vs*. an empirical equation including CaO, MgO, FeO and P_2O_5 [72]. The discrete points are the present study industrial data (1873 K).

The departure from the equilibrium curve is the driving force for dephosphorization or rephosphorization. Figure 99 shows the Model 2's equilibrium prediction for the present industrial data, as well for results from other EAF facility and laboratory data obtained elsewhere [82].

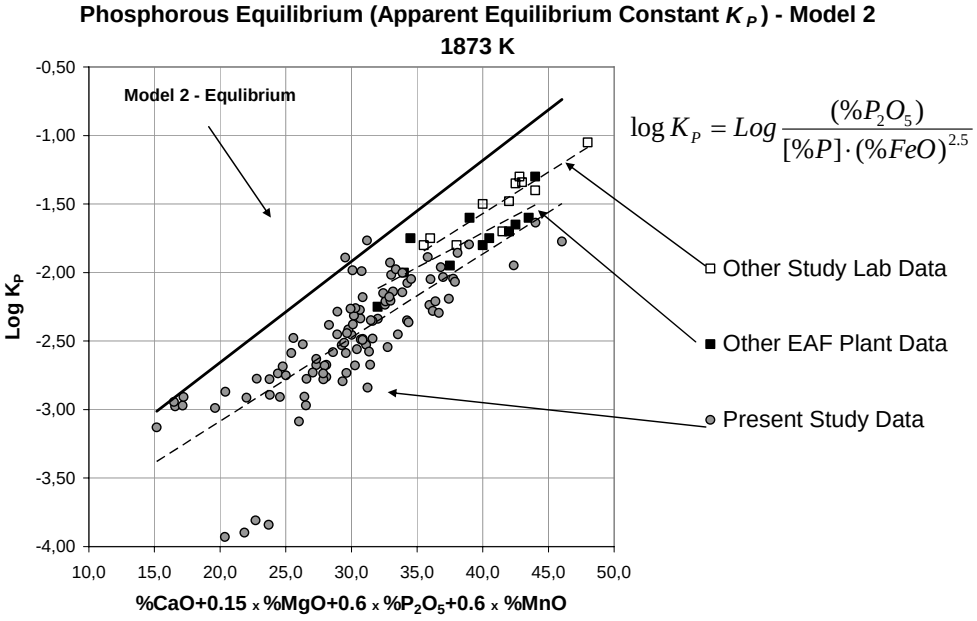

Figure 99 – Model 2 Log K_P vs. an empirical equation including CaO, MgO and P_2O_5. Other EAF and laboratory data [82] are added to the present study data (1873 K).

The estimates of K_P regarding the present study data are in reasonable agreement with other industrial data (Figure 99). If the empirical Model 1

described earlier by eq. 151 is underestimating the phosphorus in equilibrium for the current operational conditions, the higher the departure from the equilibrium models, the higher the driving force for dephosphorization and smaller the rate parameter are. Consequently, the k_{C2}/k_P ratio would be higher than expected. When Model 2 is applied, the departure from the equilibrium is smaller than Model 1's prediction, but the difference found in k_{C2}/k_P could be decreased only 25-30%, and it would be at least four times higher than expected still, according to diffusivity coefficient ratio. Nevertheless, the assumption that the reaction interface is the same for both coupled reactions of carbon and phosphorus oxidation, may not be accurate. If the CO bubbles interface with Fe-C-P droplets is larger than the interface for phosphorus reaction, the difference found for k_{C2}/k_P ratio in this study could be partially explained. Further investigation is required to evaluate the dynamic of mass transfer regarding coupled reactions of carbon and phosphorus in Fe-C-P droplets and slag in emulsified media.

However, comparing the results of rate parameter k_P and "$m_P^* A$" computed in industrial scale, according to Table 25, the present study results are in agreement with other of experiments conducted elsewhere [72].

Table 25 – Summary of rate parameter of dephosphorization and product $m_P^* A$ for the current study and other researchers [72].

	Current Study		**Others**	
	k_P	$m_P.A$	k_P	$m_P.A$
	min^{-1}	m^3/min	min^{-1}	m^3/min
Minimum	0,04	0,64	0,05	1,02
Maximum	0,25	25,92	1,00	21,00
Average	0,13	3,61		
Best Fit			0,25	5,22
BOF			1,00	
Laboratory Experiments			0,16	

Differences in the stirring conditions and the intensity of slag-metal emulsion among EAF facilities may lead to significant differences in the rate parameter.

5.1.4.
Post combustion ratio

Post combustion in the gas phase of the EAF volume

The average computed for post combustion ratio R_{PC}^{MaxAtm} were 0.1 and 0.22, for all heats and heats with post combustion injectors activated (PC Injectors), respectively. Both are lower than data presented in literature [9, 100-102] because the model estimates do not consider the infiltration of atmospheric air as a possible additional source of oxygen to proceed the oxidation of CO above the slag line, neither is this source assumed to promote iron oxidation. The literature values reflect additional post combustion by infiltration air. Figure 100 presents an example of CO content and PCR in the off-gas phase: higher PCR during meltdown because the PC injectors are activated, and high CO flow rate during refining stage due to significant carbon injection. PCR is almost negligible after 30 minutes because the use of PC Injectors is discontinued.

The energy release and its transfer from post combustion reaction has been discussed extensively, since it is not clear if the decrease in the achieved electrical energy consumption is mostly caused by iron oxidation instead of CO oxidation. Iron yield can easily vary by 0.5-1.0% on monthly basis due to raw materials issues, making it difficult to separate one effect to the other. In other words, post combustion may be over estimated due to iron oxidation.

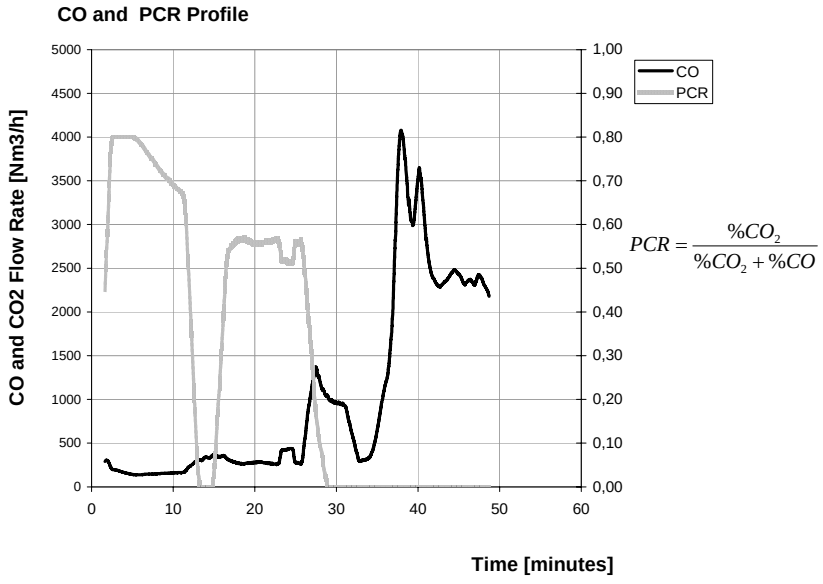

Figure 100 – Model prediction for CO flow rate and PCR (Post combustion Ratio); heat 80883

Post combustion in the slag phase

The R_{PC}^{Slag} parameter is expected to be low, and assumed to be in the range of 0 - 0.05. Actually, the average was 0.025 and shown a minor effect on the oxygen mass balance.

5.1.5. Iron Oxide Reduction

The proposed model presumes the iron oxide reduction rate $r_t^{\text{Fe-Red}}$ is controlled by mass transfer of FeO in the slag or chemical kinetics, and the reaction area is proportional to the carbon weight in the slag $W_{C,t}^{\text{Slag}}$ [97]. Equation eq. 199 first struggles with the definition of $(\%\text{FeO}^{\text{eq}^*})_t$, which considers the FeO in dynamic equilibrium at the interface of reaction.

$$r_t^{\text{Fe-Red}} = k_{\text{Fe-Red}}^{\text{CMInj}} \cdot W_{C,t}^{\text{Slag}} \cdot \frac{\left((\%\text{FeO})_t - (\%\text{FeO}^{\text{eq}^*})_t\right)}{100} \qquad \text{eq. 199}$$

If the Fe-C-O system and reaction eq.AN1 - 47 are selected, the definition of equilibrium becomes a critical concern because the data presented in Figure 101 indicates a significant departure of %wt FeO content in the bulk of slag phase when soluble carbon content is higher than 0.10%.

$$FeO_{(l)} + \underline{C} = Fe + CO \qquad \text{eq.AN1 - 47}$$

At oxygen flow rate through lance injector of 2,000 Nm^3 O_2/h at 1.2-1.5 m oxygen jet length, the O_2 pressure at impact would be about 4.4 atmospheres absolute - this is how the coherent jet is designed for this distance to the bath. The issue is that this is a local pressure at impact rather than the overall reaction interface. It is not realistic to assume such pressure in the overall interface of reaction over the entire reactor. Also, it is known that a low jet impact pressure does not bring the system closer to equilibrium - rather it moves away from equilibrium because of less mixing. So, the question is whether this is a pressure factor, or a mixing problem that causes deviation from equilibrium. Therefore, it can be presumed that:

- Iron oxide reduction rate is not fast enough to achieve the equilibrium along EAF processing time;

- Carbon mass transport in metal liquid phase to the gas-metal interface is limited when %C<%C^{Cr} (0.10 - 0.20 %wt), allowing more oxygen to dissolve in the metal phase.

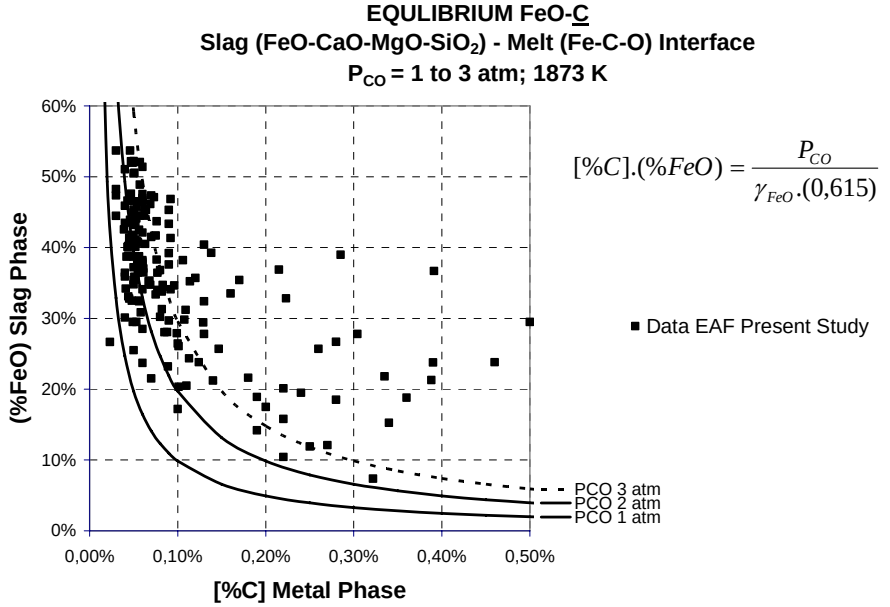

Figure 101 – The curves are the mass concentration of FeO in slag phase for different basicity index in equilibrium with carbon in the Fe-C metal phase. The discrete points are measured furnace slag chemistries.

Additionally, if $(\%\mathrm{FeO}^{eq*})_t$ is assumed to be equal to the slag composition in the bulk of the slag phase, the driving force measured by $\left((\%\mathrm{FeO})_t - (\%\mathrm{FeO}^{eq*})_t\right)$ would be almost not available when carbon content is around 0.050% for tapping, because the FeO content the slag bulk would be too high and closer to the supposed equilibrium. Likewise, in this heat processing stage, the reduction rate usually is known to reach a high degree. Therefore, the concept of $(\%\mathrm{FeO}^{eq*})_t = (\%\mathrm{FeO}^{s\text{-}g})_t$ is sometimes misunderstood, (s-g index means slag-gas interface). Actually, the reactions described in eq.AN1 - 43 and eq.AN1 - 47 correspond to the overall reaction, and the first one was used to compute the FeO-C equilibrium calculation at Figure 101.

$$FeO_{(l)} + C_{gr} = Fe + CO \qquad \text{eq.AN1 - 43}$$

$$FeO_{(l)} + \underline{C} = Fe + CO$$ eq.AN1 - 47

If the hypothesis of liquid phase mass transfer of FeO in slag is the rate controlling mechanism, the reaction described in eq.AN1 - 56 is assumed to be in equilibrium [33, 34, 36, 38, 39, 103].

$$FeO_{(l)} + CO = Fe + CO_2$$ eq.AN1 - 56

At such high temperatures, $P_{CO_2} \approx 0$, $P_{CO} \approx 1$, therefore, $a_{FeO} \to 0$ at the slag-gas interface.

$$K_{FCO_2} = \frac{P_{CO_2}}{a_{FeO} P_{CO}}$$ eq.AN1 - 57

Hence, equation eq. 199 was replaced by,

$$r_t^{\text{Fe-Red}} = k_{\text{Fe-Red}}^{\text{CMInj}} \cdot W_{C,t}^{\text{Slag}} \cdot \frac{(\%\text{FeO})_t}{100}$$ eq. 220

Former studies postulated that viscous flow occurs by movement of particles past other particles [41], and a link between diffusion coefficient and the mobility $B = \overline{\upsilon} / \overline{F}$ concept was proposed. Mobility is defined as the ratio of the mean velocity by force acting or a potential field on the particle. The flux $\overline{J}$ due to many particles influenced by the same potential field is describe in eq. 221, where the force field is replaced by a potential gradient ∇V, and C_i is the molar concentration of specie *i*.

$$\overline{J} = C_i \cdot \overline{\upsilon} = C_i \cdot \overline{\upsilon} = C_i \cdot B \cdot \nabla V$$ eq. 221

Diffusion is a process in inhomogeneous multi-component systems, which aim to equilibrate the whole system by mass transport. The rate of equilibration, or homogenization, is influenced by temperature, composition, the structure of the phases and the size of the species. Hence, considering the potential gradient as the chemical potential gradient, eq. 221 can be written for one dimension as

$$\overline{J} = -C_i \cdot B \cdot \frac{\partial(\mu_i^0 + RT \cdot \ln a_i)}{\partial x}$$ eq. 222

Moreover, the possibility of mixed control dictated by mass transfer of FeO to the slag-gas interface and Boudouard reaction at gas-solid carbon interface,

motivated others authors [33, 36, 37] to investigated iron oxide reduction with rate models based on iron oxide activity instead of the simplified approach through %wt FeO. Thus, equation eq. 223 was also evaluated in this study.

$$r_t^{\text{Fe-Red}} = k_{\text{Fe-Red}}^{\text{CMInj}} \cdot W_{C,t}^{\text{Slag}} . (\text{a}_{FeO})_{\text{t}} \qquad \text{eq. 223}$$

5.1.5.1.
Iron Oxide Activity

In order to test the model described by eq. 223, the activity coefficient of iron oxide has to be calculated. Former researchers [8, 37, 104] suggested that basicity index could influence iron oxide activity, as presented earlier in Figure 5. More recently, the influence of basicity index was found too weak by other authors [33, 105]. Combining the activity coefficient estimates from former researchers [8, 104] the data from others who did not consider the basicity index CaO/SiO_2 relevant [105], Figure 102 resulted in a moderate trend connecting iron oxide activity coefficient and basicity index B.

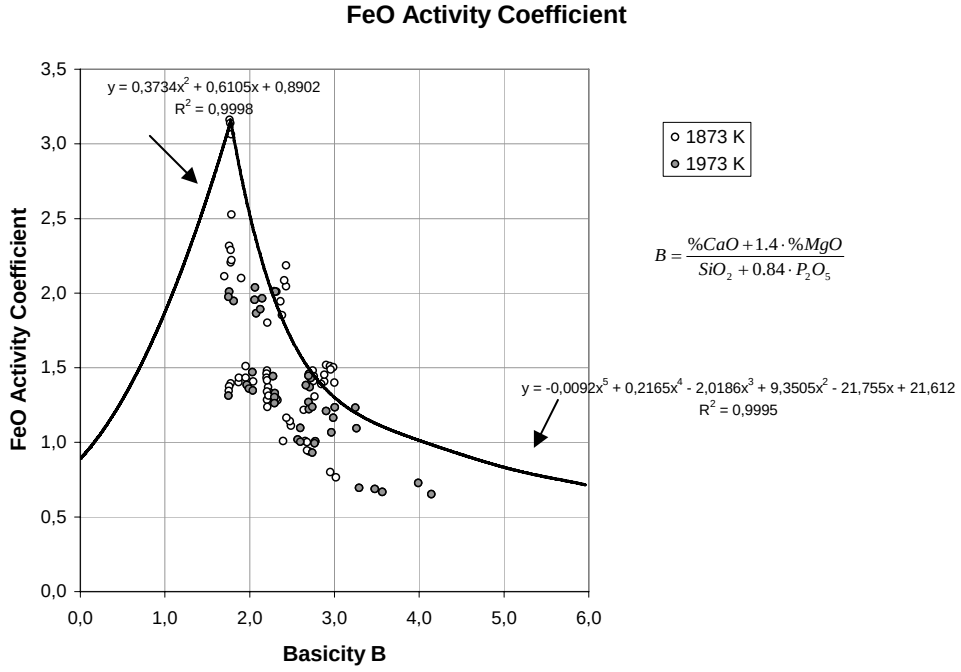

Figure 102 – Iron oxide activity coefficient [8] curve and discrete points [105] represent the measured furnace slag chemistries.

However, the fact that mole fraction of different oxides are interdependent because $\sum C_{MeO_i,t}^{Slag} = 100\%$, came up as an argument that basicity index or CaO and SiO_2 isolated effects are not affecting the activity coefficients significantly.

Considering the present study data, the basicity index CaO/SiO_2 shown in Figure 103 is varying in a range of 1.7 to 2.2, and a clear interdependence of oxides in slag such as FeO, CaO, SiO_2 and MgO are plotted in Figure 104.

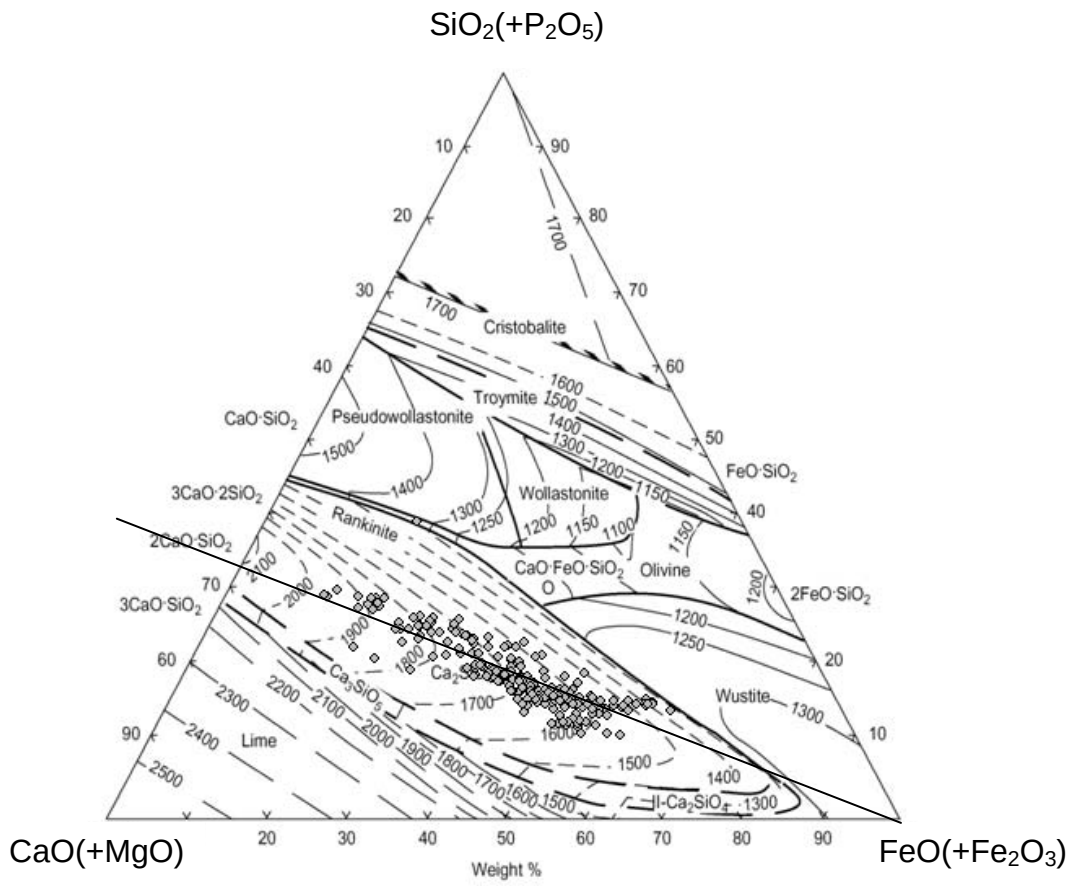

Figure 103 – Schematic representation of a pseudo-ternary phase-diagram adapted from Slag Atlas [106] for simplification plot of slag chemistry. The discrete points are measured furnace slag chemistries ($\%Al_2O_3$ ~ 3%).

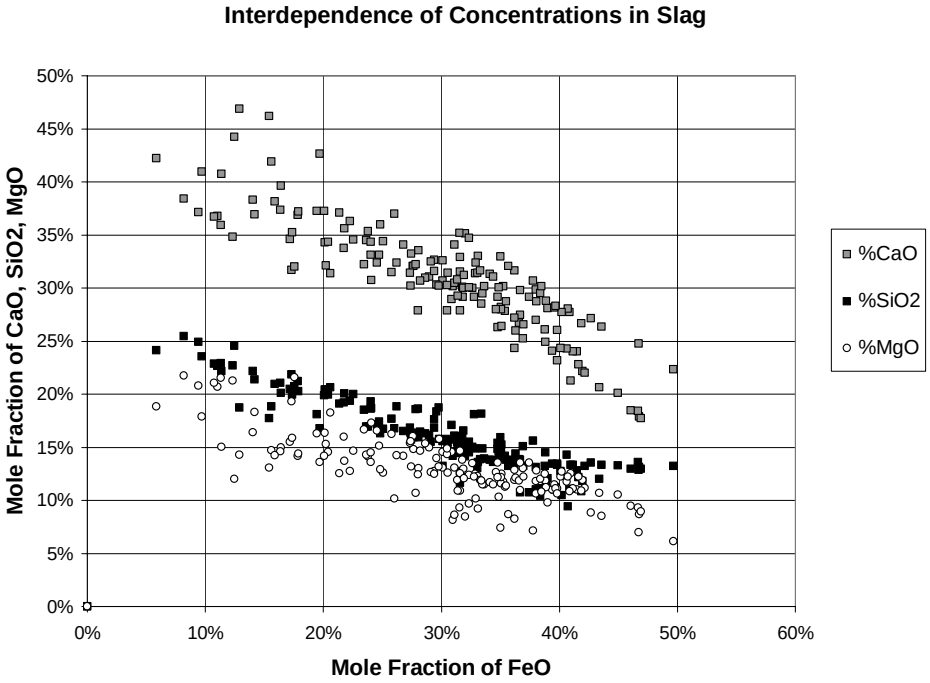

Figure 104 – Mole fraction interdependence between slag oxides.

Iron oxide activity has been controversial due to the complexity of oxides solutions. Particularly for steelmaking slag, most of authors conclude that iron oxide activity present a positive deviation in respect ideal behavior, even though others concluded for negative deviation (Figure 105).

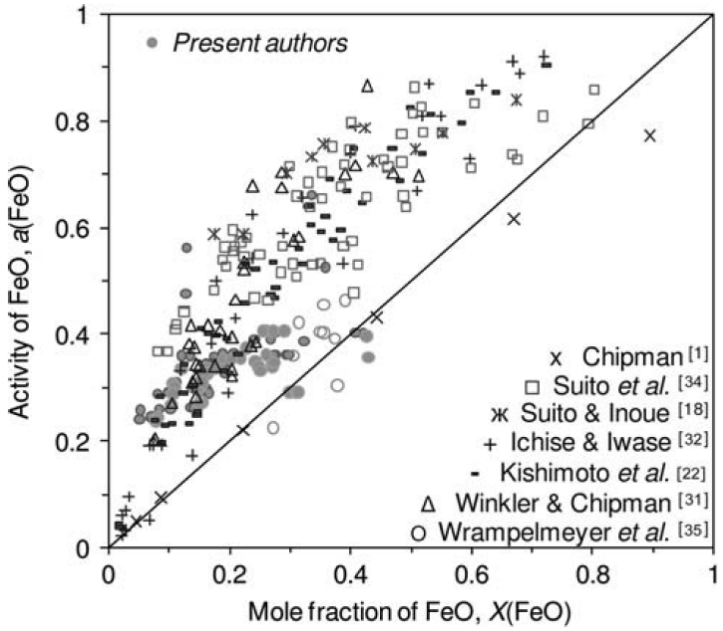

Figure 105 – Effect of FeO concentration on its activity in the range of 1573-1873 K, based on several authors data [105].

A regular solution model [107] was used to estimate the iron oxide activity for this study purpose, according to eq.AN1 - 80. The approximate validity of the model was considered quite satisfactory to formulate the reactions of the ferrous-ferric iron equilibrium in FeO-$FeO_{1.5}$-CaO-MnO-MgO-SiO_2 slag solutions [12, 86] .

$$RT \ln \gamma_i = \sum_j \alpha_{ij} X_j^2 + \sum_j \sum_k (\alpha_{ij} + \alpha_{ik} - \alpha_{ijk}).X_j X_k \qquad \text{eq.AN1 - 80}$$

The regular solution model eq.AN1 - 80 applied to the slag chemistries of the present study, as expected, resulted in a strong dependence of FeO activity coefficient and its mole fraction, according to Figure 106.

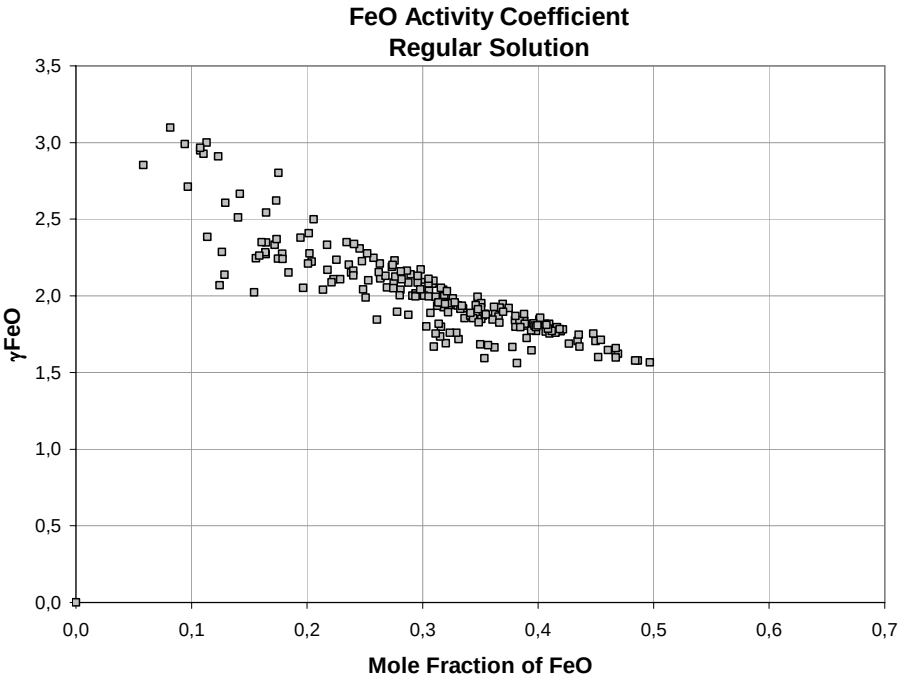

Figure 106 – Activity coefficient of FeO vs. its mole fraction computed by the regular solution model at 1873 K.

The ferrous iron oxide FeO is not stoichiometric and is usually described as FetO, where t varies from 0.95 to 0.98. It was observed that pure ferrous oxide metal, in equilibrium with oxygen saturated iron, presented 0.94Fe^{2+} : 0.06 Fe^{3+} mass ratio [105]. Besides, the non-stoichiometry of FeO was considered negligible in steelmaking processes [78].

The ferric ion, or Fe^{3+} (~ $FeO_{1.5}$) was estimated by ThermoCalcTM (cell model) to be less than 0.5% in equilibrium with the slag and Fe metal phases chemistries available in the present study. Hence, FeO notation in this study corresponds to description shown in eq. 224

$$\%FeO = \frac{MW_{FeO}}{MW_{Fe}} \cdot \%T.Fe \qquad \text{eq. 224}$$

where, $\%T.Fe$ is the total iron mass measured concentration.

Figure 107 presents the a_{FeO} estimated by the adopted regular solution model [107], which is in relevant agreement with CSIRO model [33], and the schematic representation of an average of the data collection from Figure 105. Other empirical models [105] seemed to be limited to FeO mole fraction lower than 0.38´ and underestimates the a_{FeO} in the range of 0.20 to 0.38 FeO mole fraction, when compared to the regular solution model estimates.

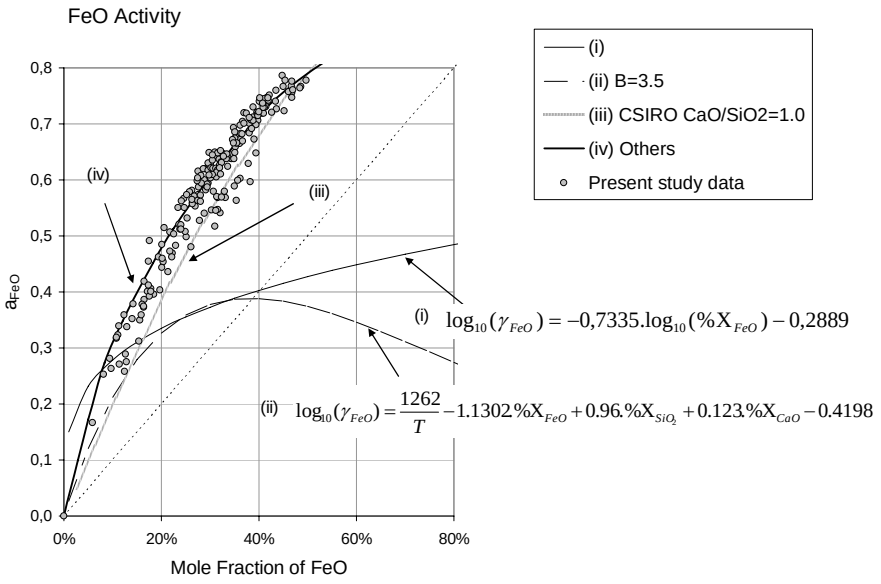

Figure 107 – FeO activity (i) empirical model at 1873 K [105]; (ii) empirical model with basicity index B = 3.5; (iii) Commonwealth Scientific and Industrial Research Organization (CSIRO) at 1723-1823 K [33]; (iv) schematic average of data collection at 1573-1873 K Figure 105; Discrete points computed from regular solution model applied to the slag chemistries of the present study at 1873 K.

In contrast to other FeO activity coefficient models [10], the estimated a_{FeO} by the regular solution model is not influenced by slag basicity index B, and show moderate correlation with optical basicity instead, according to Figure 108. Further study are recommended to evaluate in more detail the correlations found

between iron oxide activity coefficients based on a regular solution model and the optical basicity (Figure 109 and Figure 110).

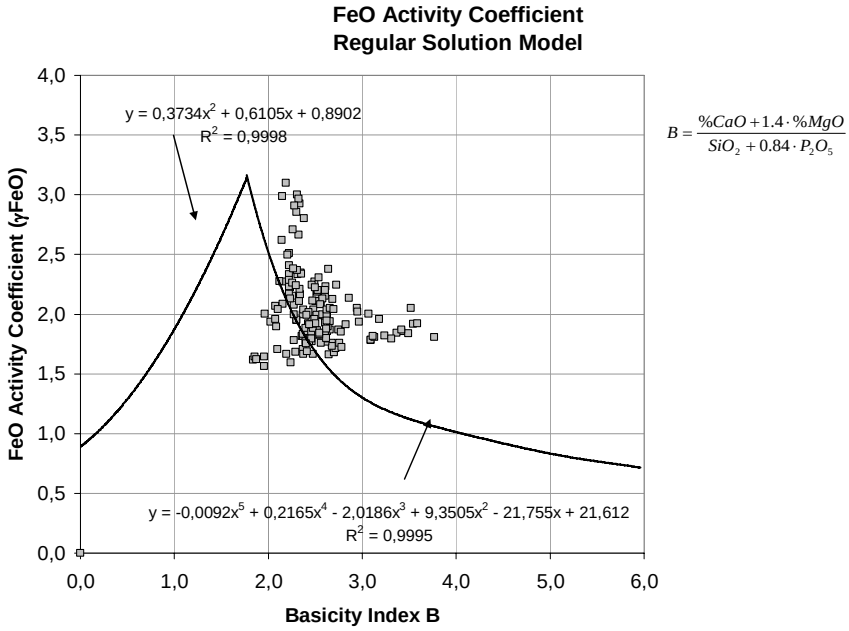

Figure 108 – FeO activity coefficient estimates versus basicity index B at 1873 K [10]. The discrete points are measured furnace slag chemistries and computed at 1873 K.

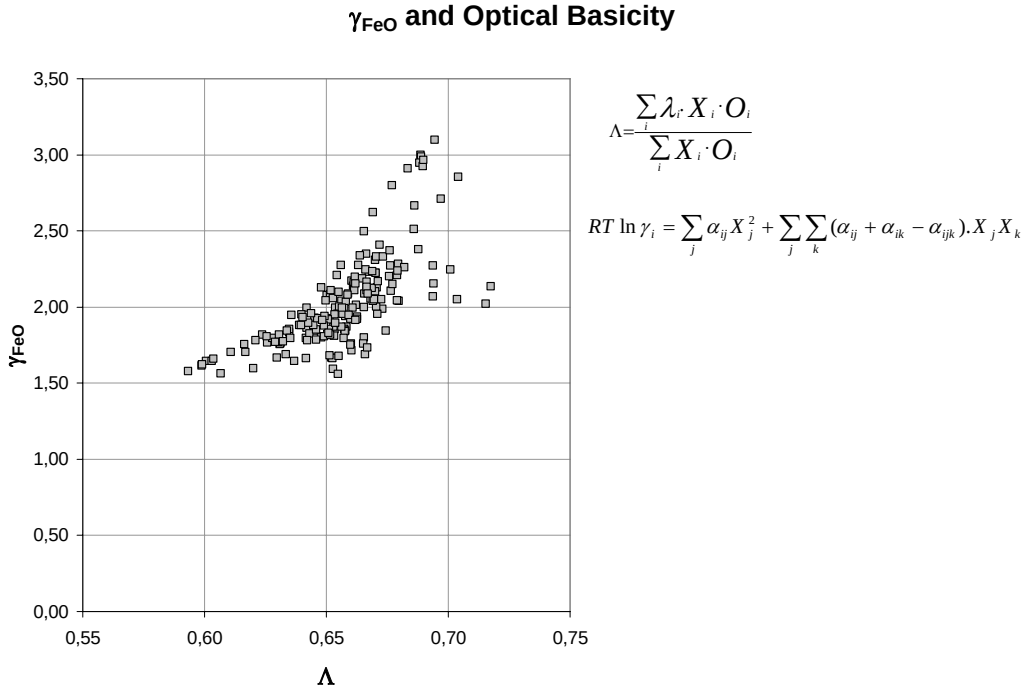

Figure 109 – Activity coefficient of FeO versus optical basicity at 1873 K.

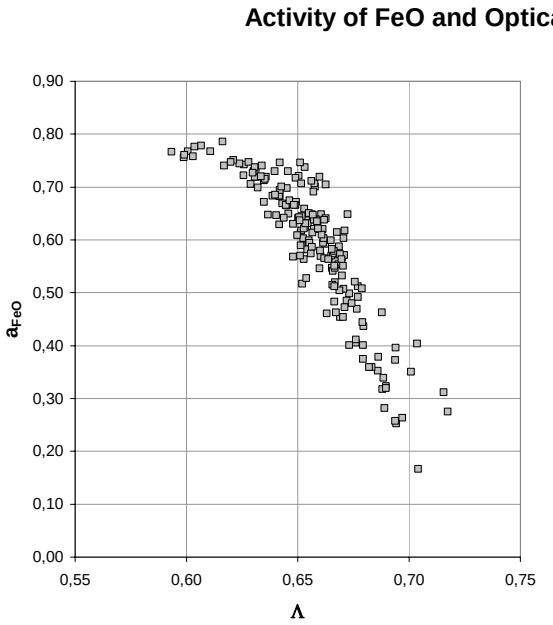

$$\Lambda = \frac{\sum_i \lambda_i \cdot X_i \cdot O_i}{\sum_i X_i \cdot O_i}$$

Figure 110 – Activity of FeO versus optical basicity at 1873 K.

5.1.5.2. Rate Constant of Iron Oxide Reduction

During EAF steelmaking, carbonaceous materials such as coke are injected into the slag to reduce iron oxide and make the slag foam. Slag foaming is critical for the protection of refractory, water cooled roof and sidewalls panels from the arc, minimizing heat loss.

In the present study, several experiments in industrial scale were conducted aiming to force iron oxide reduction in a higher degree by increasing the ratio carbon/oxygen injection after meltdown was complete. Usually, in melt shops with high productivity profile, there is not such high carbon injection rate, and the oxygen injection is not interrupted, or even decreased during refining step. This job procedure avoids process interruption as well decrease the electrical energy consumption. In contrast, some specialty steel mills follow a primary de-oxidation procedure just before tapping the melt to the ladle. For secondary metallurgy purposes, certain quality and amount of solid/liquid inclusions are not accepted, then, significant portion of the product of de-oxidation should be gaseous. Accordingly, the EAF electrical power is switched off and deep carbon injection is provided not assisted by oxygen injection through 10 to 15 minutes before tapping. During this period of time, significant FeO is

reduced, and sometimes metal phase recarburization (carbon dissolution) may occur.

According to the current model prediction, almost 15-35% of the carbon injected maybe discarded as non-reacted particles during slag off. This means carbon is reacting out side the furnace or remains in the tapped slag and is useless for improving iron yield. One way to verify this hypothesis is to collect slag samples and cool them fast enough to avoid remaining carbon to react with FeO. This indicates that job procedures and the slag door technology should keep the slag as long as possible inside the vessel to improve Fe recovery.

The calculated parameter k_{red} varied significantly, and maybe related to:

- Variation of operational conditions
- Slag basicity index
- Iron oxide state, concentration and CO stirring
- Slag viscosity
- Temperature

Variation of operational conditions

The reactions rates can be influenced by operational variations, such as reported in similar industrial scale study [108]: lance angle of the submerged pipes handled by lance manipulator, flow rate of carrier gas even at the same carbon mass flow, particle size, off-gas system and premature slag off. In addition, the slag off assumed in the current model is a linear function of the coke injection rate, which is somehow not accurate. Tilting movements in the EAF aiming to accelerate slag off can cause deviations from the model prediction too.

Slag basicity index

Furthermore, it is also suggested that the slag basicity may affect the rate of reduction of FeO: higher the SiO_2 or lower the basicity in the slag, lower the FeO reduction rate [33, 37, 108]. In the phase diagram FetO-CaO-SiO_2 presented in Figure 111, two lines of iso-basicity index CaO/SiO_2 and four levels of FeO molar fraction are depicted by dotted lines. Considering a fixed FeO content, increasing de basicity index, a slight decrease in a_{FeO} is expected,

according to the regular solution model adopted in the present study. At FeO molar fraction of 0.6, an increase of basicity index from 1.0 to 2.3 would result in less than 10% of decrease in a_{FeO}. In the present study, the binary basicity index CaO/SiO_2 is limited to a range of 1.9 to 2.5 and may not be affecting de rate in the extent some times reported in literature. Besides, the adopted regular solution is computing the isolated and combined effects of CaO and SiO_2 on the iron oxide activity.

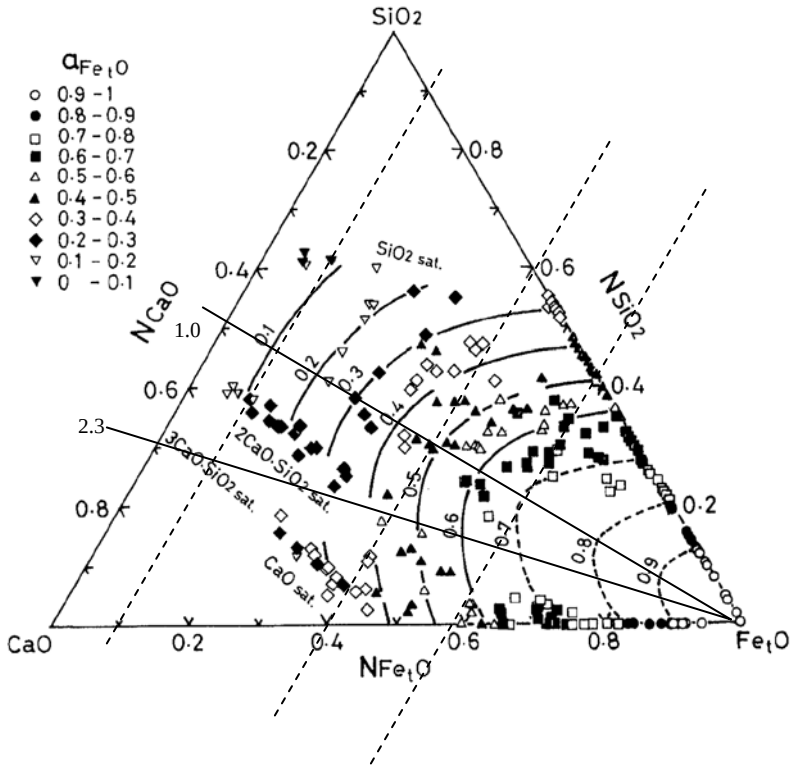

Figure 111 – Estimated values for a_{FeO} by regular solution model and the measured values in Fe_tO-CaO-SiO_2 slags equilibrate with liquid iron at 1873 K [107]

Iron oxide state and concentration

The observed variation of k_{red} implies some dependence on the wt% FeO in mass concentration, as well on the iron oxide activity, as presented in Figure 112 and Figure 113, respectively. Even though both are considered weak correlations, the correlation coefficient found based on an exponential function like $y = a.e^{b.(a_{FeO})}$ was almost 80% higher when a_{FeO} is applied in comparison to wt% FeO.

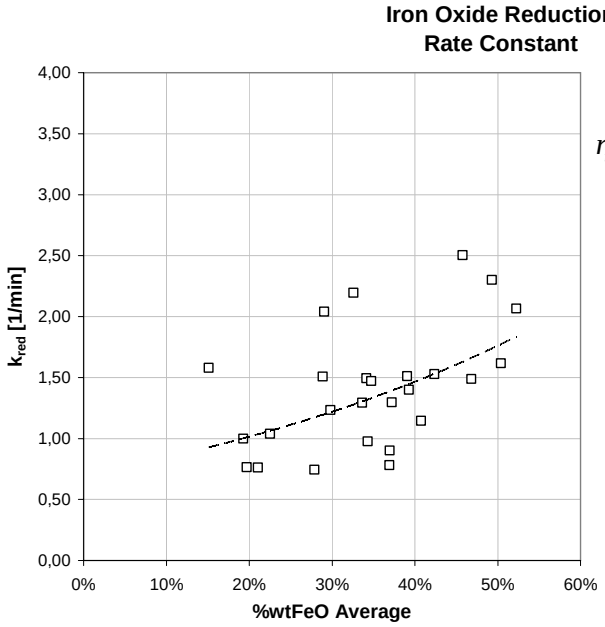

$$r_t^{\text{Fe-Red}} = k_{\text{Fe-Red}}^{\text{CMInj}} \cdot W_{C,t}^{\text{Slag}} \cdot \frac{(\%\text{FeO})_t}{100}$$

Figure 112 – Iron oxide reduction rate parameter versus the average of iron oxide mass concentration ($y = a.e^{b.(wt\%FeO)}$, R^2 = 0.27)

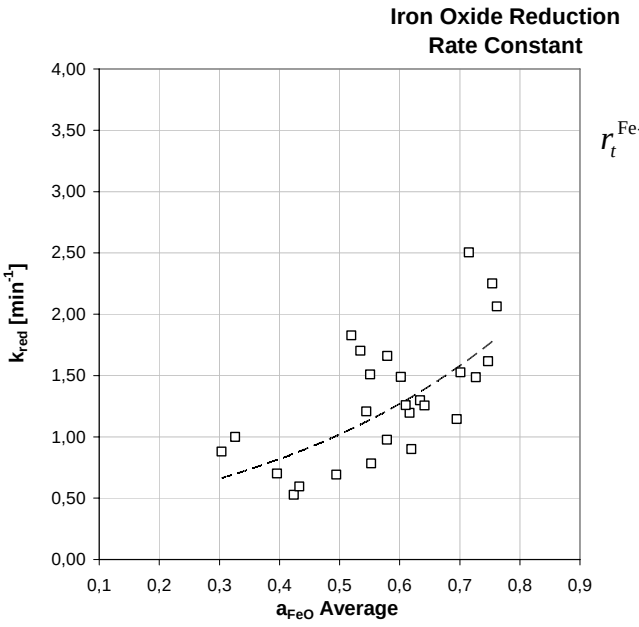

$$r_t^{\text{Fe-Red}} = k_{\text{Fe-Red}}^{\text{CMInj}} \cdot W_{C,t}^{\text{Slag}} \cdot (a_{FeO})_t$$

Figure 113 – Iron oxide reduction rate parameter versus the average of iron oxide activity. ($y = a.e^{b.(a_{FeO})}$, R^2 = 0.47)

The dependence of the apparent rate parameter k_{red} with FeO content in slags was also observed in other studies [33, 37, 39, 103]. Despite the fact that there is no consensus about the rate controlling mechanism, some statements are reported and generally accepted, such as: (i) liquid phase mass transfer of

FeO is concluded for wt% FeO lower than 10%; (ii) chemical control for wt% FeO higher than 40%; and (iii) mixed control for wt% FeO in the range of 10% to 40%. The alleged chemical control has been a controversial statement. Experiments conducted in the range of 1470 to 1560 ^{o}C computed activation energy around 60 kcal/mol, which is definitely pointing out that at least one chemical reaction is the rate controlling mechanism [36]. Excluded laboratory scale experiments, when rotating samples or melt stirring were used to minimize mass transfer rate controlling, other studies indicating Boudouard chemical reaction as the controlling mechanism at carbon source-gas interface, the available activation energy measurements are somehow viewed with certain skepticism [109].

The trends presented in Figure 112 and Figure 113 may imply that increasing FeO content, the reaction at carbon source interface creates higher CO flow rate, and the evolution of CO bubbles is presumed to accelerate FeO mass transfer to the slag-gas interface. It has been observed elsewhere [110] that gas bubbling takes place at the interface of Fe-C droplets created by the iron oxide reduction. The gas bubbles detach and move upward against buoyancy force through the emulsion, mixing the slag-metal-carbonaceous materials all the way up to leaving the liquid phase. Examining the curve $a_{FeO} - k_{red}$ (Figure 112), its convexity profile seems to be opposite to the concavity depicted by the curve $\%X_{FeO} - a_{FeO}$ (Figure 107). Actually, $dk_{red} / d\, a_{FeO}$ should decrease with increasing a_{FeO} at high FeO content, in contrast, the stirring effect may be increasing k_{red} .

As a simplification, the current rate model presumes that reaction $FeO_{(l)} + C_{gr} = Fe + CO$ is sufficient to formulate the rate equation $r_{red} \propto k^{*}_{red} \cdot (\%C) \cdot (\%FeO_{(l)})$. This assumption is somehow not respecting the elementary reaction premise. This reaction is just an overall reaction, and do not represent other several elementary reactions such as adsorption-desorption mentioned previously on session 2 Literature Review. On the other hand, other model formulations which consider the p_{CO} measurement at the reaction interface as well the estimates of interface of reaction extent probably will fail, because such measurements cannot be done in industrial scale.

The current assumption that the ratio $Fe^{+3}/T.Fe$, where $T.Fe = Fe^{+2} + Fe^{+3}$, is negligible or not effective on iron oxide reduction rate at equilibrium with Fe-Low C, may be another source of model uncertainties. The role of $Fe^{+3}/T.Fe$ was suggested to have influence on the dephosphorization kinetics [86, 87]. Experiments were conducted with CaO-Li_2O-SiO_2-FeO-Fe_2O_3 slag/ Fe-4.4%C pointed out the increase of dephosphorization rate when the oxygen potential at the slag-metal interface was increased by means of higher Fe_2O_3 contents in the slag. Other researchers evaluated if the reduction rate parameter would increase by increasing the basicity index, which causes increase in $Fe^{+3}/T.Fe$ ratio. Even though Fe_2O_3 is presumed to be more easily reduced than FeO, the reduction rate parameter depended relatively weakly on the oxidation state of the iron in slag, $k \propto \left(Fe^{+3}/Fe^{+2}\right)^{\alpha}$, where α varied in the range of 0.15 to 0.25 [33].

Considering the mass balance of the overall injected oxygen in the EAF as demonstrated afterwards in Table 26, about 20% of total injected oxygen is consumed to create FeO in the slag. Thus, if $Fe^{+3}/T.Fe$ reaches an average of 0.50, for instance, computing 120 kg slag/ton, (a) 40% of FeO, means ~ 8 Nm^3 O_2/ton ; (b) 20% FeO + 20% Fe_2O_3, means ~ 9 Nm^3 O_2/ton. Hence, the difference in respect to the total oxygen injection is smaller than 2%.

Slag viscosity

The viscosity of slag melts is usually described as function of temperature and its structure. Former models were developed from silicates, whose polymeric behavior could be modified by the addition of basic oxides, then, the basicity indexes are attempting to infer about the slag viscosity [106]. Furthermore, under saturation conditions, soluble species can precipitate as solid phase, decreasing the liquid fraction of slag. Obviously, increasing the fraction of precipitated solid phases Θ, higher the effective fluid viscosity μ_e, accordingly [111],

$$\mu_e = \mu.(1-1.35\Theta)^{-5/2} \qquad \text{eq. 225}$$

The mass transfer in the slag liquid phase is performed by ions, due to ionic nature of slags. Eyring relationship (eq.AN3 - 38) has been used successfully in several works, suggesting an inverse proportionality of diffusivity of species in respect to the slag viscosity [106] (λ is the mean inter-atomic distance),

$$D = \frac{k_B.T}{2.\lambda.\mu}$$ eq.AN3 - 38

Therefore, if FeO mass transfer is the rate controlling mechanism, the viscosity may also affect the rate of the iron oxide reduction. Figure 114 presents a schematic ternary diagram adapted for CaO(+MgO)-SiO_2(+P_2O_5)-FeO(+Fe_2O_3), with present study slag chemistries depicted by the discrete points, over iso-viscosity lines. Consequently, slag containing 20 %wt FeO concentration, may result in viscosity almost three times higher than 40 %wt FeO, since the melting point of such slag is increased, which will reduce the liquid fraction. The current model does not account variations on transport phenomena, and perhaps, the effect of viscosity is primarily affecting the rate parameter k_{red} of iron oxide reduction. Figure 112 implies a decreasing of k_{red} when wt% FeO decreases.

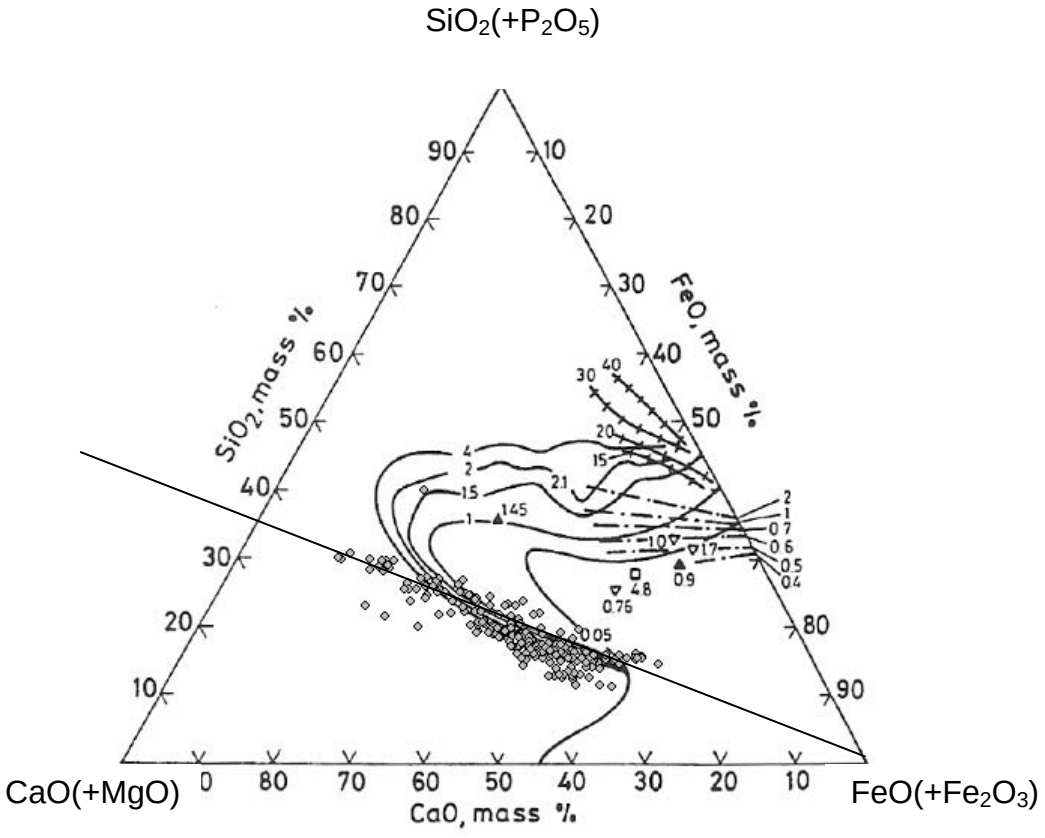

Figure 114 – Schematic representation of a pseudo-ternary viscosity (Poise = 10^{-1} Pa.s at 1400 ^{o}C) diagram adapted from Slag Atlas [106] for simplification plot of slag chemistry. The discrete points are measured furnace slag chemistries (%Al_2O_3 ~ 3%).

Temperature

The current model does not take into account the thermal balance, and consequently, no bath temperature variation is estimated. However, it is expected a minor effect of the temperature in the range of 1550 to 1650 ^{o}C on the constant of decarburization rate, since the rate–controlling step is accepted to be not the chemical reaction. The mass transfer of oxygen and carbon, which are the controlling parameters, depends much less on temperature. In the case of iron oxide reduction, this assumption is not fully applicable, because the controlling may be mixed: both FeO mass transfer in the slag as well chemical reaction at slag-gas and carbon-gas interfaces. Future model developments should include the available temperature data, instead of using a constant temperature of 1873 K. The temperature correction like $T = a + b.e^{t}$ as presented in Figure 90 has been applied only for the dephosphorization model.

5.1.5.3. Recarburization

Re-carburization model was proposed in this study to provide supplementary inference about the role of carbon reactions for a particular limiting condition, when the FeO content in the slag reaches the vicinity of equilibrium assumed for the system Fe-C-O. At this point, it is expected that more FeO reduction would occur and re-carburization would be observed, following the equilibrium curve (Figure 115) [37].

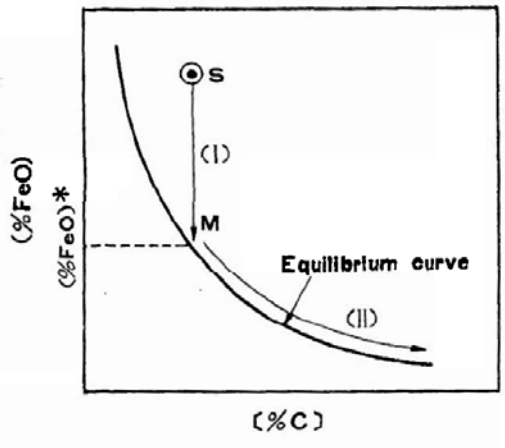

Figure 115 – Schematic representation of the expected patterns reduction of iron and recarburization.

According to the model described in session 3.13 Recarburization, the computed dissolution rate is fast enough to have the blend of carbonaceous particles (overall) completely dissolved in the metal phase in 4 seconds (Figure 116). For model simplification, when the FeO in equilibrium is attained, all carbon particles are able to dissolve in the metal phase in 2 seconds, corresponding to a conversion of 96%. In present study, the time interval for data collection in EAF occurred at every 2 seconds.

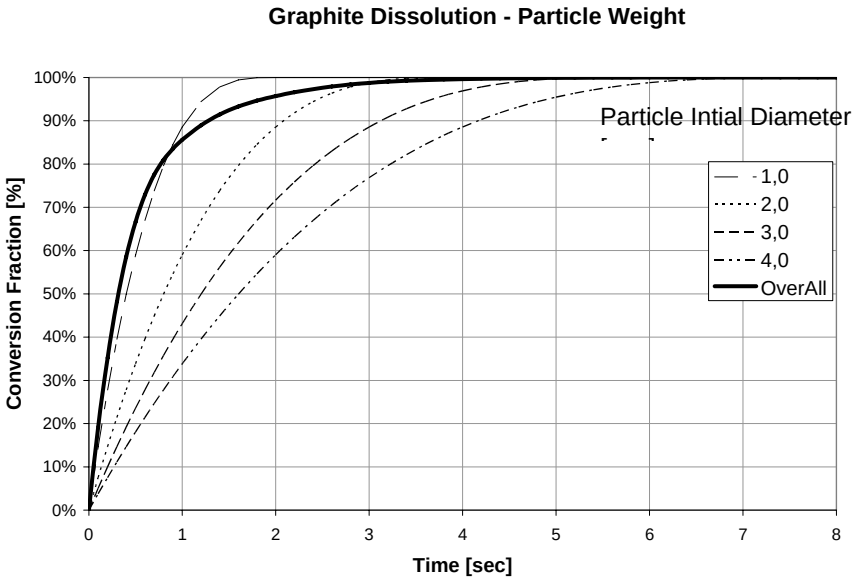

Figure 116 – Dissolution of injected coke in terms of mass conversion. “overall” means the weighted average of the size distribution of the carbonaceous material used in this study.

The re-carburization model could not be evaluated in more detail in this study, because only two heats got closer to the presumed Fe-C-O equilibrium curve. The model predictions for carbon and phosphorous were not in agreement with the samples’ chemistry. For instance, heat 99317 was submitted to deep carbon injection and, according to the samples analysis shown in Figure 117, recarburization occurred, despite the fact that the model did not predicted any carbon dissolution in the metal phase. Furthermore, rephosphorization also took place. Even though the phosphorus content in equilibrium increased, the driving force predicted by the model for rephosphorization was not achieved in time. The phosphorus content in equilibrium increased because of the drop on *Lp* (Figure 118), caused by higher temperature and low FeO content in the slag (Figure 119). Actually, recarburization and dephosphorization are connected to the oxygen concentration, and they tend to occur in the same direction.

The current model failed to start the recarburization algorithm, maybe due to (and/or): (i) the Fe-C-O equilibrium curve is underestimating the FeO content in equilibrium, and recarburization could occur at higher FeO content (Figure 120); (ii) part of the injected carbon that did not react with the slag could penetrate and dissolve in the metal phase directly, allowing deoxidation and recarburization to start around 48-50 minutes. At this point, rephosphorization also occurred and wt% FeO decreased to 20% ; (iii) in the interface slag-metal, dissolution of carbon in metal phase was more favorable than the iron reduction rate due to an increase in slag viscosity, as well because of lower FeO content (driving force is decreased).

The direct dissolution of carbonaceous materials appears to be more realistic in consequence of operational issues related to unexpected submergence of consumable pipes in the metal phase. Carbon could have been dissolved faster in metal phase than in slag phase, since 25%wt FeO seems to be too high to equilibrate with 0.20%wt C dissolved in the metal phase.

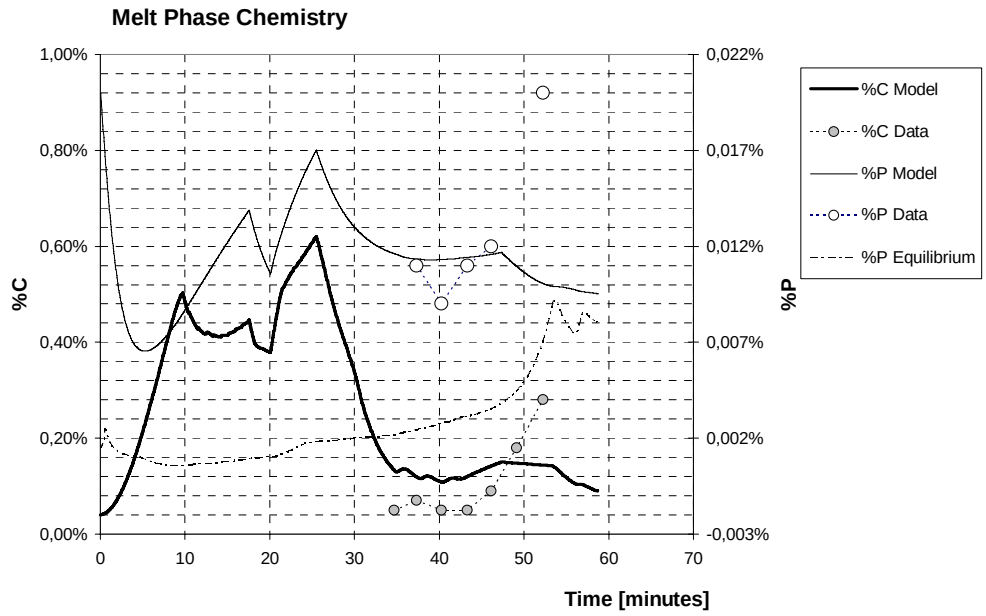

Figure 117 – Carbon and phosphorus model prediction, measured chemistry (discrete points) in metal phase; heat 99317, 11% pig iron

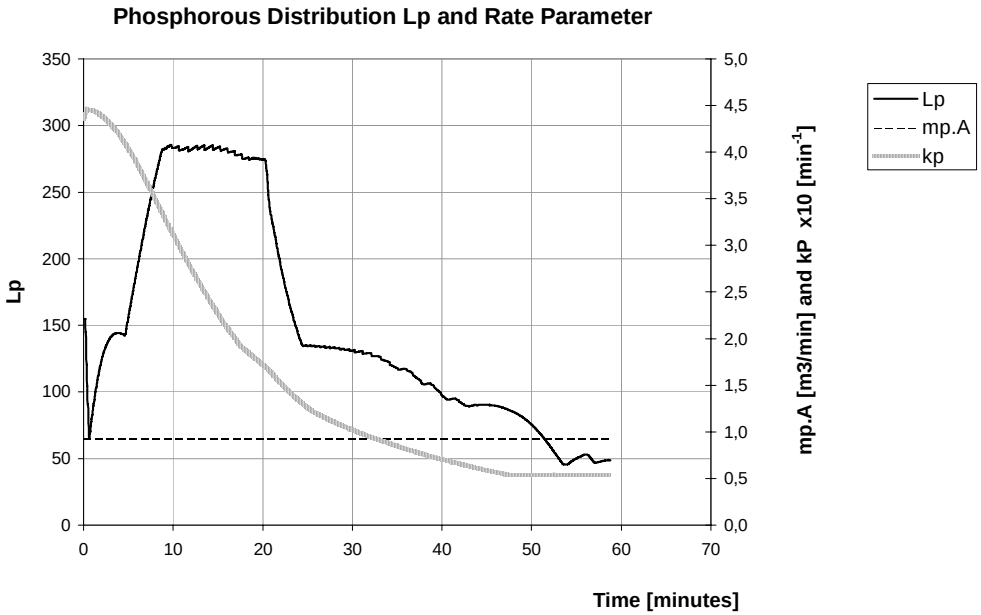

Figure 118 – Phosphorus distribution L_P, product $m_P^* A$, and overall dephosphorization rate parameter k_P, heat 99317, 11% pig iron.

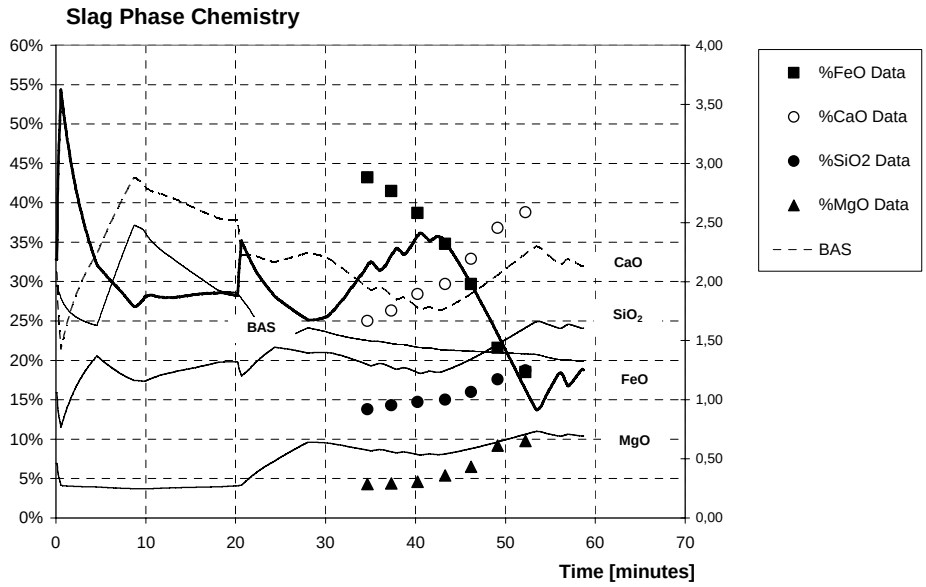

Figure 119 – Slag chemical composition predicted by the model and %wt measured slag chemistry (discrete points): heat 99317, 11% pig iron

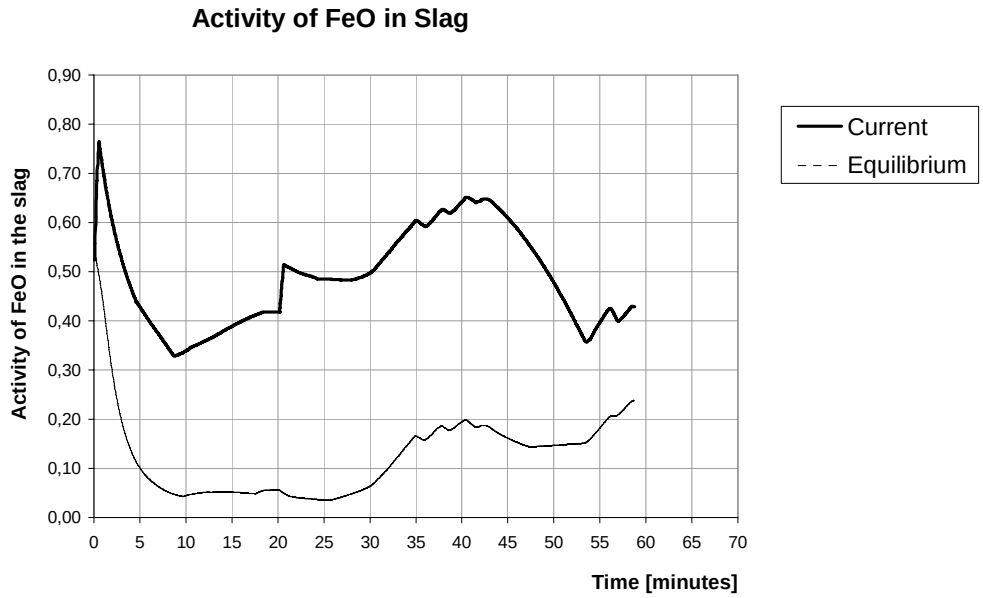

Figure 120 – FeO activity predicted by the model and FeO activity in equilibrium, heat 99317, 11% pig iron

The second and last case of recarburization and rephosphorization, occurred in the heat 90306 (Figure 121), starting around 35 minutes, when %wt FeO content in the slag was ~ 15% (Figure 122), much lower than heat 99317 (Figure 119). The carbon injection time was long, without significant oxygen injection for 13 minutes. Additionally, coke was charged earlier through the first bucket, aiming to increase the resident time of carbonaceous material reacting with slag phase.

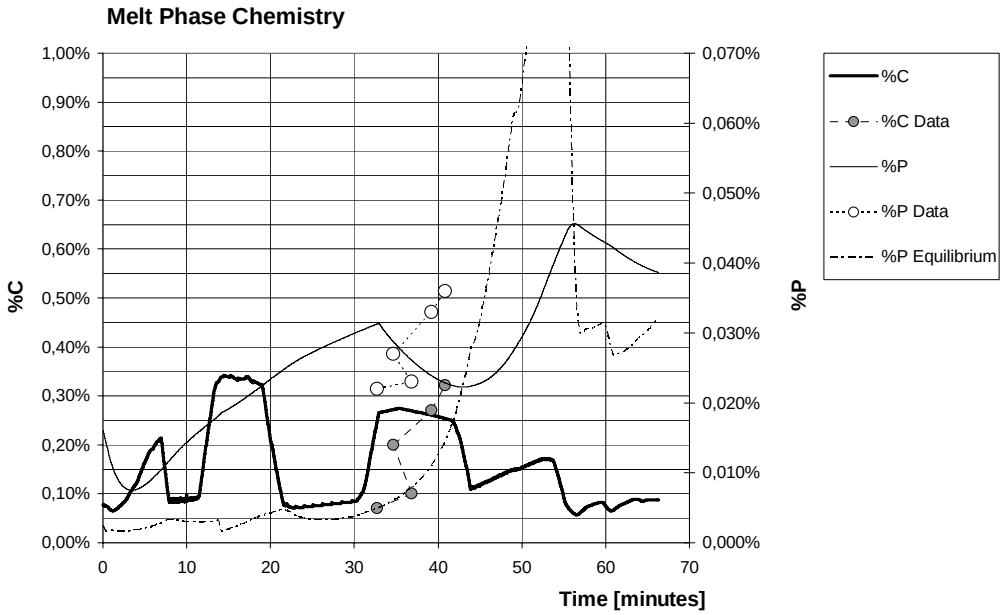

Figure 121 – Carbon and phosphorus model prediction, measured chemistry (discrete points) in metal phase; 90306, 34% pig iron.

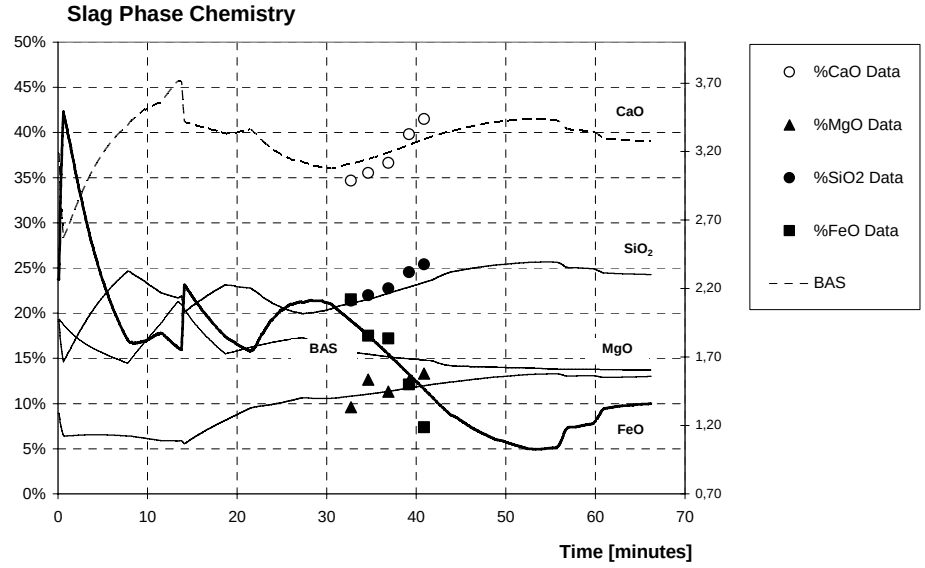

Figure 122 – Slag chemical composition predicted by the model and measured slag chemistry (discrete points): heat 90306, 34% pig iron

The current activity of FeO and its expected activity in equilibrium in the system Fe-C-O are shown in Figure 123, which indicates the condition $a_{FeO} = a_{FeO}^{eq}$ adopted to start the recarburization algorithm, was satisfied in two

occasions: (i) 5-10 minutes caused by charged coke dissolution in meltdown stage; (ii) and 45-65 minutes during full coke injection along the refining step. In fact, according to the computed melting rates, ferrous materials were completely molten around 35 minutes (Figure 124).

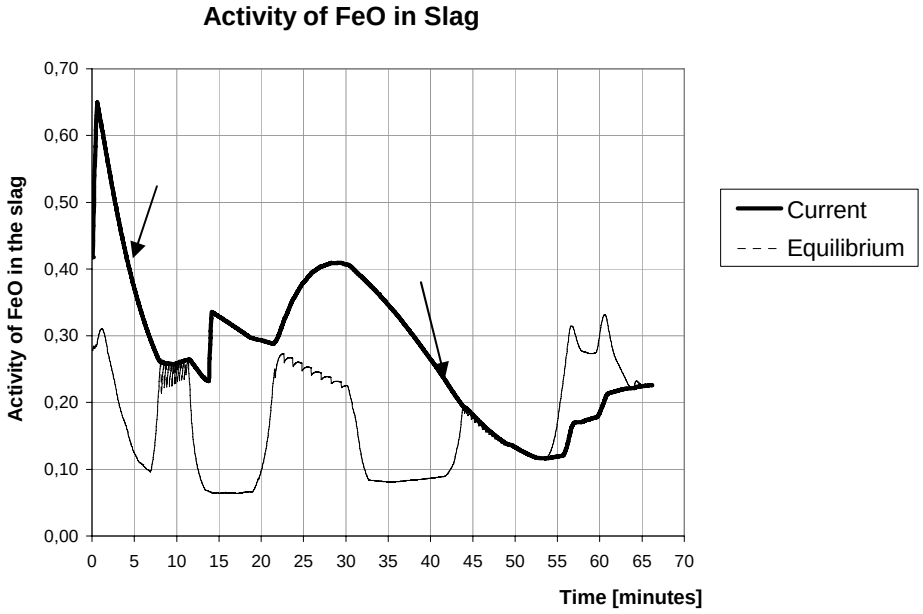

Figure 123 – FeO activity predicted by the model and FeO activity in equilibrium, heat 90306, 34% pig iron

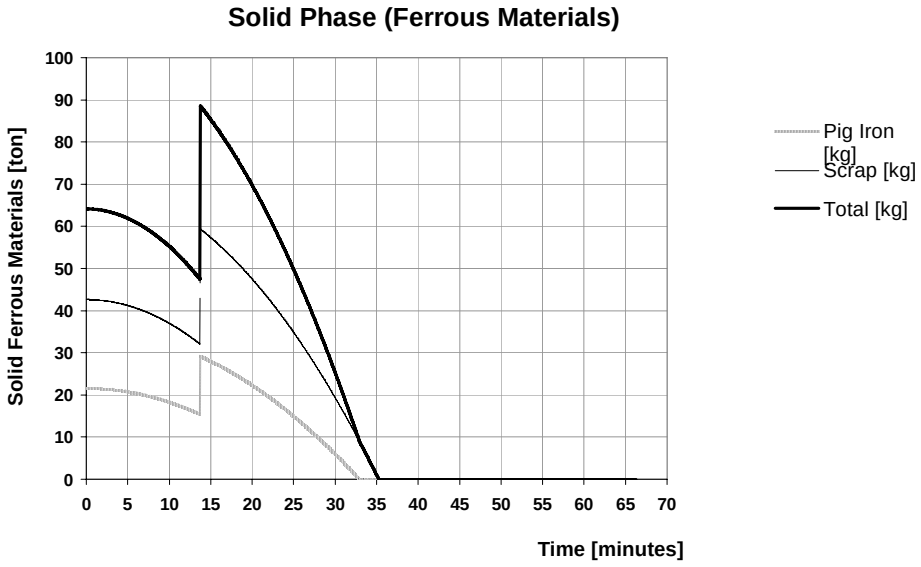

Figure 124 – Estimated solid phase (pig iron + scrap mix) evolution along the heat 90306

The combination of melting pig iron with no oxygen injection in the interval of 32 to 42 minutes (Figure 125), could explain the increase in carbon content

shown in Figure 121. Carbon dissolution from the remaining pig iron and probability not from carbon injection, resulted in soluble carbon increase. Injected carbon was partially consumed for FeO reduction, and other particles not reacted left the vessel in the slag off volume. According to the model prediction, recarburization occurred after 45 minutes, and the apparent contradictory estimate of $a_{FeO} < a_{FeO}^{eq}$ could exist only for a few minutes, because of carbonaceous material dissolution rate in metal phase is faster than iron oxide reduction in slag phase at such low FeO content, which was measured and fairly estimated to be around 5% %wt FeO. Minutes later, the presumed equilibrium condition was achieved.

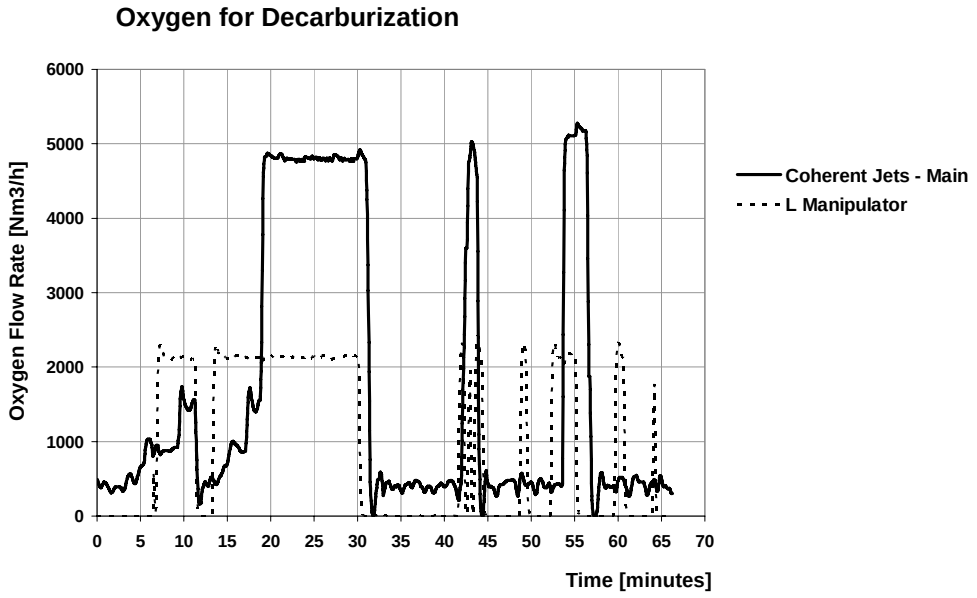

Figure 125 – Measurement of experimental oxygen injection profile along the heat 90306. Both Coherent Jets and Lance Manipulator are dedicated to inject oxygen in the metal phase

The computed phosphorus in equilibrium increased very fast due to late melting of pig iron, and also because of decreasing oxidation level in metal and slag phases. However, in this particular heat, the model failed to determine the phosphorus content in the metal phase. The predicted phosphorus pattern did not follow the higher level of phosphorus found in the last metal phase probe. The driving force was favorable for rephosphorization only between 42 to 56 minutes, where, $(\%P - \%P^{eq}) < 0$, the L_P was very low (Figure 126), and the temperature was increasing fast. Perhaps the empirical L_P model is

underestimating the %P in equilibrium and/or the extrapolation for such low level of FeO content would be a constraint.

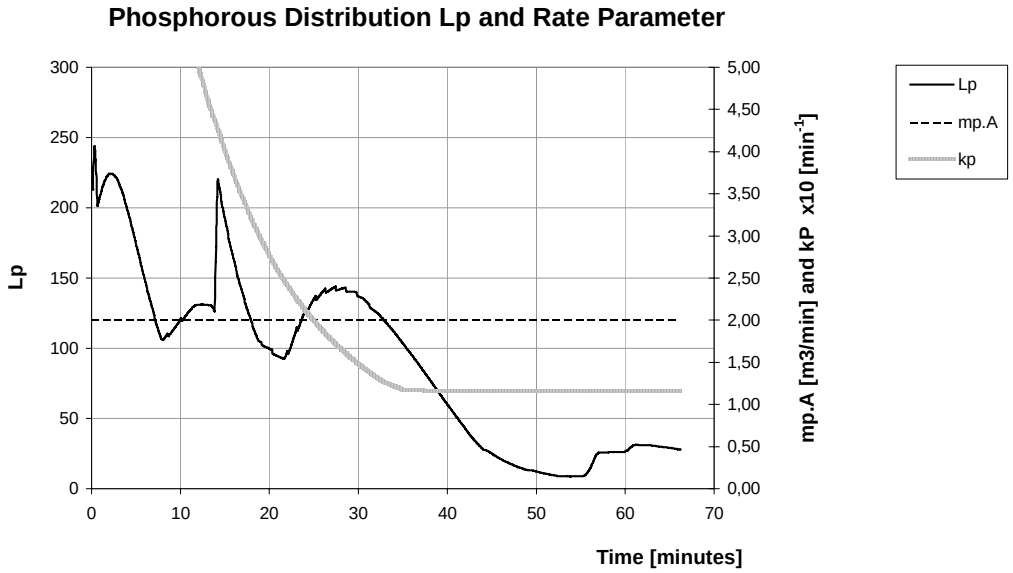

Figure 126 – Phosphorus distribution L_P, product $m_P^* A$, and overall dephosphorization rate parameter k_P, heat 90306, 34% pig iron

Figure 127 depicts schematic examples of operational patterns of iron oxy-reduction, decarburization and recarburization. There are two master curves for FeO-C relation: the solid line is the equilibrium at 1873 K, and $p_{CO} = 1.5$; the dotted curve is current condition apart from the presumed equilibrium. These patterns depend on the way oxygen and carbon injection are adjusted in EAF facilities.: pattern (i) means a balanced injection of carbon and oxygen, following the stoichiometry of reaction $FeO_{(l)} + C_{gr} = Fe + CO$, decarburization and FeO reduction are occurring; (ii) higher oxygen flow rate is imposed, decarburization is occurring, but the excess of injected oxygen is dissolving in the Fe-C metal phase and more FeO is created; (iii) similar to pattern ii, but with higher carbon flow rate, forcing FeO reduction simultaneously to decarburization; (iv) in contrast, very high carbon flow rate combined with low oxygen input.

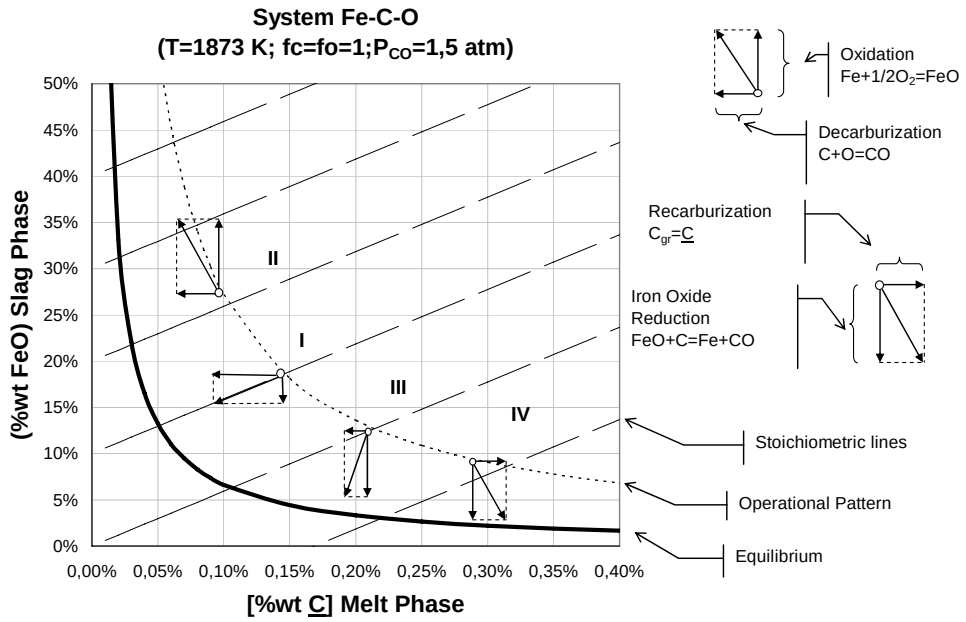

Figure 127 – Schematic representation of typical patterns of oxy-reduction of iron, and decarburization and recarburization.

Heats processed in high EAF productivity facilities, where the refining stage is short and carbon-oxygen injection flow rates ratio are usually in the range of 0.60-0.85 kg carbon/Nm^3 O_2, the probability to follow the “Operational Pattern” shown in Figure 127 is higher.

Based on the data collected for heats submitted to longer periods of carbon injection (>10 minutes) without relevant and simultaneous oxygen injection, it could be speculated they are almost following an “Equilibrium Pattern”. Figure 128 shows a few data of soluble oxygen-carbon found at an EAF facility [112] submitted to deep and long deoxidation practice, 10-15 minutes before tapping. The metal chemistries (discrete points) were in quite better agreement with the presumed Fe-C-O equilibrium. Figure 129 also points out the pattern %wt FeO slag versus %wt C metal phase for three heats is the conditions described above. They showed better agreement trends when compared to high productivity EAF facilities not submitted to deep deoxidation presented earlier in Figure 101. The three dashed-thin lines depicted in Figure 129, refer to the equilibrium patterns where the activity coefficient of iron oxide corresponded to the slag chemistry predicted by the regular solution model, regarding binary basicity index in the range of 1.7 to 2.2. Such trends reinforce the hypothesis that the departure from Fe-C-O equilibrium in EAF could be in part a consequence of kinetic issues.

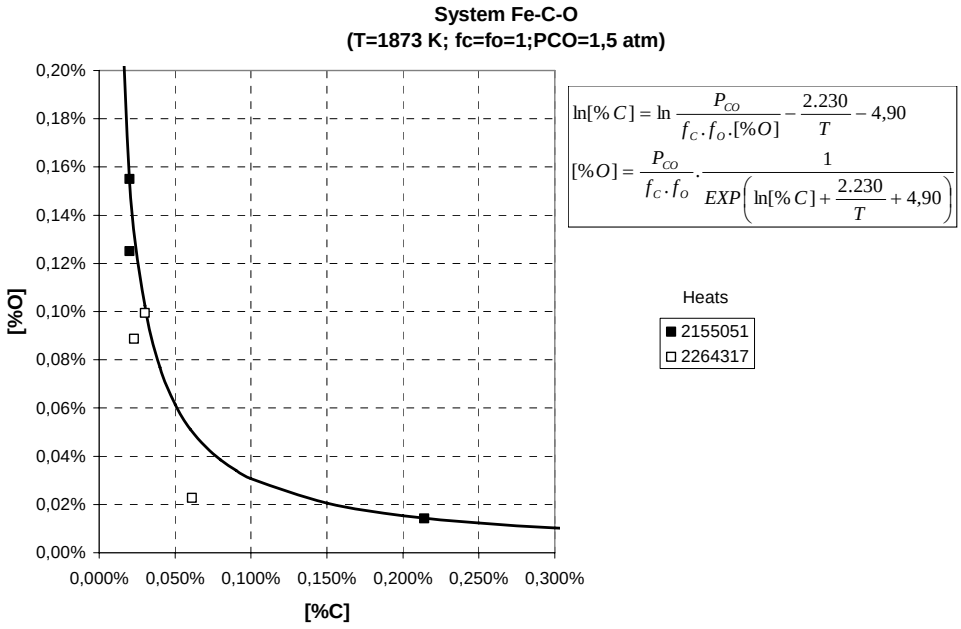

Figure 128 – Equilibrium curve for %C vs. %O soluble in iron melt. Plot of soluble oxygen by electrochemical probes and carbon content through optical spectrometer. Discrete points refer to heats 2155051 and 2264317, produced in EAF facility of the same size, scrap-pig iron basis, and regularly submitted to full carbon deoxidation before tapping [112].

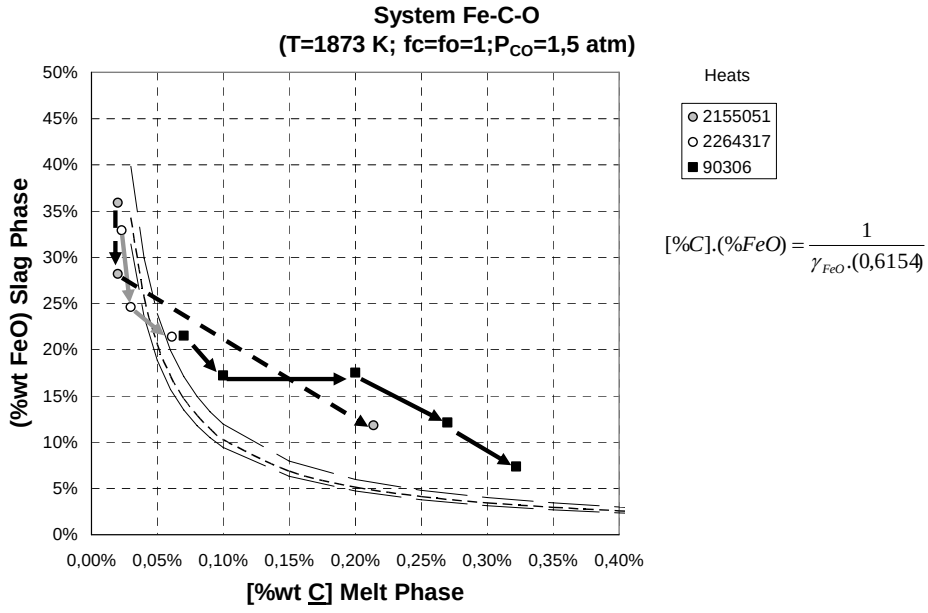

Figure 129 – Mass concentration of FeO in slag phase in equilibrium with carbon in the Fe-C metal phase. The discrete points are measured furnace slag chemistries submitted to deep deoxidation through carbon injection. Three presumed equilibrium curves are depicted in dashed-thin lines, according to different basicity indexes found in this study.

5.1.6.
Initial slag amount

The calculated initial slag amount of 2.4 ton is realistic, based on previous mass balance with real slag weight measurements. However, the estimated variation from 1 to 5 ton in the slag amount may have been caused by the refractory wear during the campaign, as well the hot heel size, both estimated visually, bringing more uncertainties for the model prediction.

5.1.7.
Effectiveness of oxygen flow rate

Most of the injectors used in this work were controlled by an automated system, allowing pre-set the flow rates for different injection program. The lance manipulator handles consumable pipes for both oxygen and carbon injection through the slag door, which could imply source of variation on the effective availability of oxygen and coke for the reactions. Furthermore, the degree of EAF volume filled by ferrous materials varied due to the wide range of pig iron charged. Hence, it is expected that the secondary parameters OLE_{FeO}, $OPCE_{Decarb}$ and $OPCE_{FeO}$, described in Table 21 present variations too. Actually, they represent the amount of oxygen consumed in the different reactions, and its complimentary portion means the amount that was wasted and addressed to off-gas. Table 26 presents the summary of oxygen mass balance.

By convention, if iron oxidation is considered a side effect, and according to the assumptions in the present model, the current operational procedures lead to oxygen injected in excess of 20% through lancing mode and 2% through post combustion mode. The oxygen excess is believed to increase the remaining iron oxide in the slag, after oxidizing C, Si, Mn and CO. The amount of oxygen sent to the off-gas phase is estimated as up to 1% and 2% for lancing and post combustion modes, respectively. Once more, the effectiveness of the post combustion injectors seems to be low, meaning that only the average of 24% of the oxygen injected is effective for post combustion according to the used operational conditions. The contribution of the incoming atmospheric air in the post combustion was not estimated.

Table 26 – The overall injected oxygen mass balance

	Total	%	100%
Lancing Mode	Oxygen consumption for	%	58,5%
	FeO -> CO, SiO2, MnO	%	37,0%
	Post combustion (CO->CO_2)	%	20,4%
	Off-gas	%	1,2%
Burning Mode	Burners	%	34,6%
PC Mode	Oxygen consumption for	%	6,8%
	FeO -> CO, SiO2, MnO	%	0,9%
	Post combustion (CO->CO_2)	%	1,6%
	FeO remaining after reactions with carbon	%	2,5%
	Off-gas	%	1,8%

5.1.8. Melting Rates

According to the results presented in Figure 130 and Figure 131, the pig iron melting rate is lower than the overall scrap blend melting rate. The variation of melting rates is high, meaning that the model prediction for metal and slag phase chemistries would be worse than presented if melting rates parameters were assumed constant for all heats. Indeed, most of electricity input, gas and powder injection are fully automatic and controlled by modern computers and PLC network in updated EAF facilities, but undoubtedly, the diverse ferrous charge arrangement brings the major sources of variation. At least one decade of searching the complex melting behavior of scrap in EAF vessels has been not enough to provide suitable models. Actually, the melting rates are computed by inverse calculation, using GRG algorithm to reach the optimum fitting of the measured contents of most relevant species in the metal and in the slag phases. The carbon and phosphorus contents are important as tracer species for tracking the pig iron melting rate. Regarding only the high carbon content and lower melting point, pig iron has a higher potential to melt earlier and faster than scrap. However, the geometry differences, specially the pig iron area to volume ratio that lies from 20 to 120 times smaller than regular scrap grade, can influence its melting kinetics. In addition, the possibility of chilling effect could explain partially why pig iron would melt, or at least be available in the hot heel, at a slower rate than scrap.

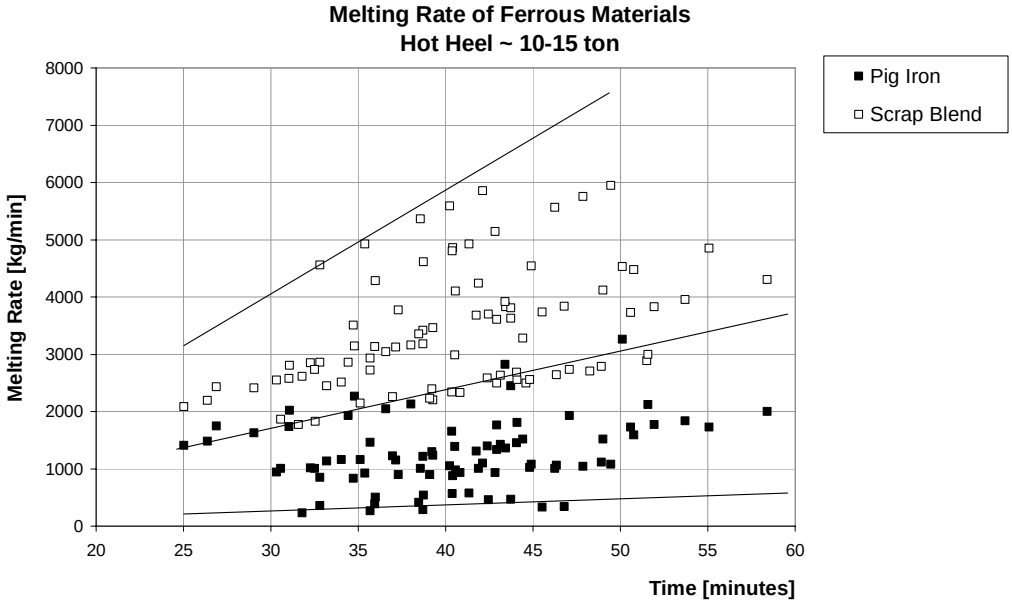

Figure 130 – Computed overall melting rates for scrap mix and pig iron charged over hot heel of 10-15 ton.

.

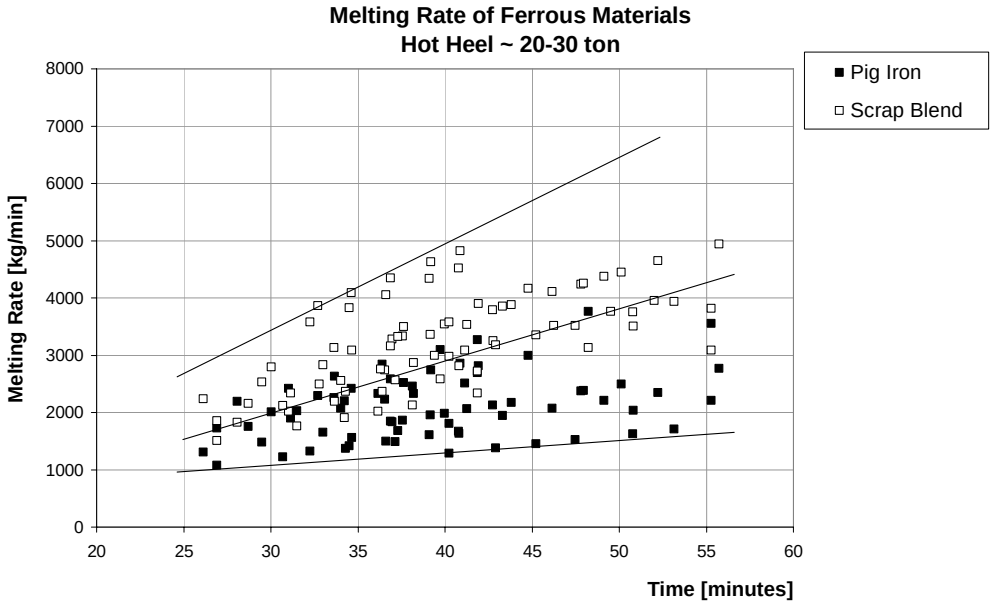

Figure 131 – Computed overall melting rates for scrap mix and pig iron charged over hot heel of 20-30 ton.

Some studies conducted on EAF industrial scale [42] have found that the pig iron melting rate seemed to be at least similar to heavier scrap grades. Reported evidences pointing out that lighter scrap grades surrounding the pig iron pieces may lead to a solidified layer enveloping pig iron, support the argument of increasing resistance to heat transfer and late pig iron melting. This

solidified layer, or shell, could also present many gaps due to shrinkage, hence, decreasing the pig iron heating rate during the first minutes of heat processing.

The scrap blend used in the present work have shown low density and high area to volume ratio, what is consistent with a higher melting rate computed for scrap when compared to pig iron. Figure 132 presents the trend of decreasing the overall melting rates when the apparent density of the ferrous materials increases.

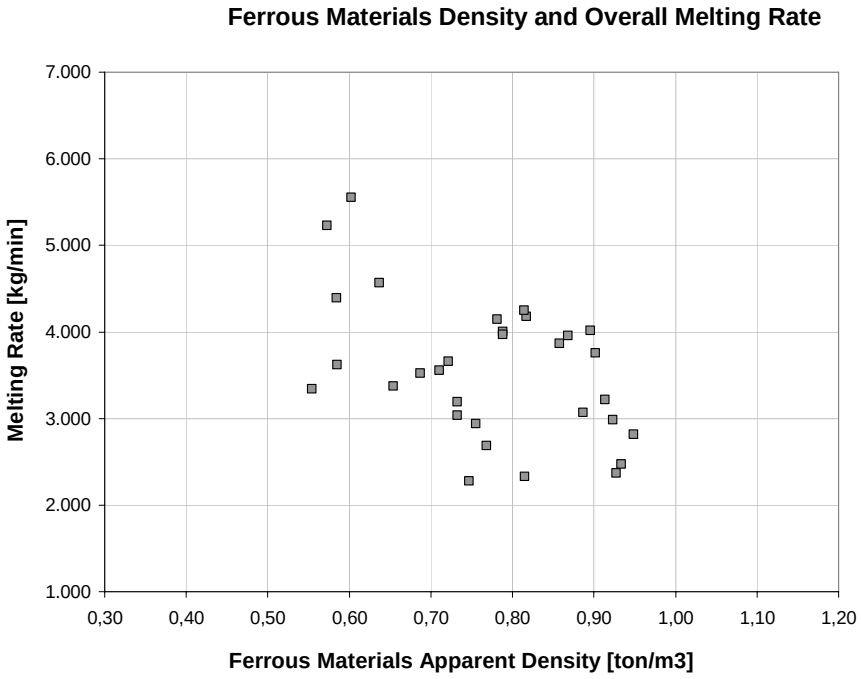

Figure 132 – Computed overall melting rates for ferrous materials (scrap blend and pig iron) versus the overall apparent density.

Figure 130 and Figure 131 show the computed melting rates for all scrap blend and pig iron used in the present study, considering two different hot heel sizes: 10-15 ton and 20-30 ton. As described earlier, as higher the enthalpy available previously to bucket charge and denoted by the hot heel size, lower the possibility of “chilling effect”. The hot heel size is almost the double in the heats shown in Figure 131, when compared to others shown in Figure 130. The apparent increase on the pig iron melting rates is in agreement with the increase of the hot heel size.

The developed model depends on a number of variables including melting rates and reaction rate parameters. The pig iron melting rate has been proved to be one of the most important factors, while scrap melting is less important. Below, follows additional examples of the melting rates effects on the chemistry prediction. Figure 133 and Figure 134 show the effect of pig iron and scrap

melting rates. The first set on Figure 133 refers to lower pig iron charge 11%, and the second set on Figure 134 is related to higher pig iron charge 39%.

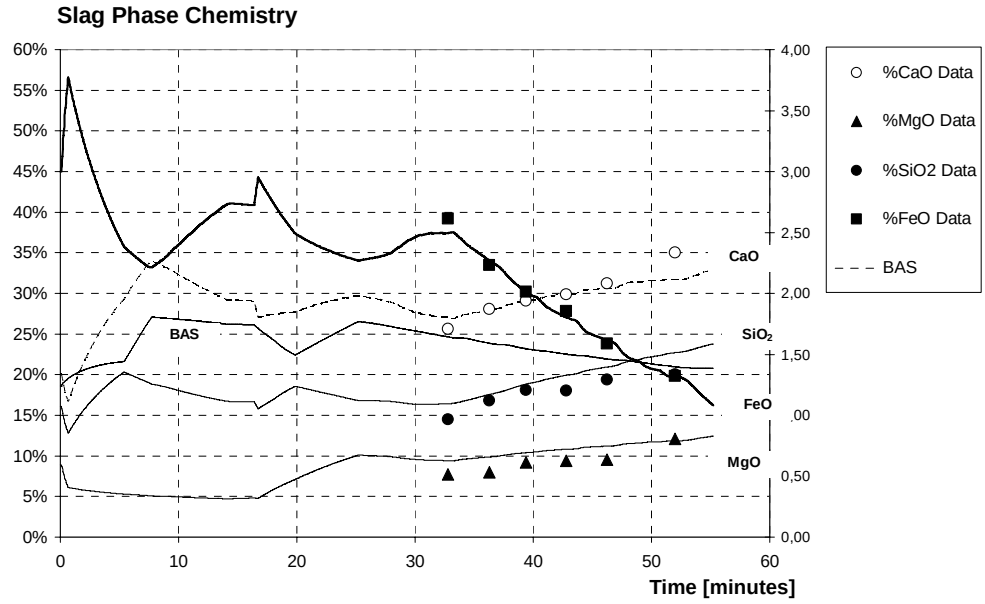

(a) melting rates pig iron 936 kg/min; scrap 3952 kg/min

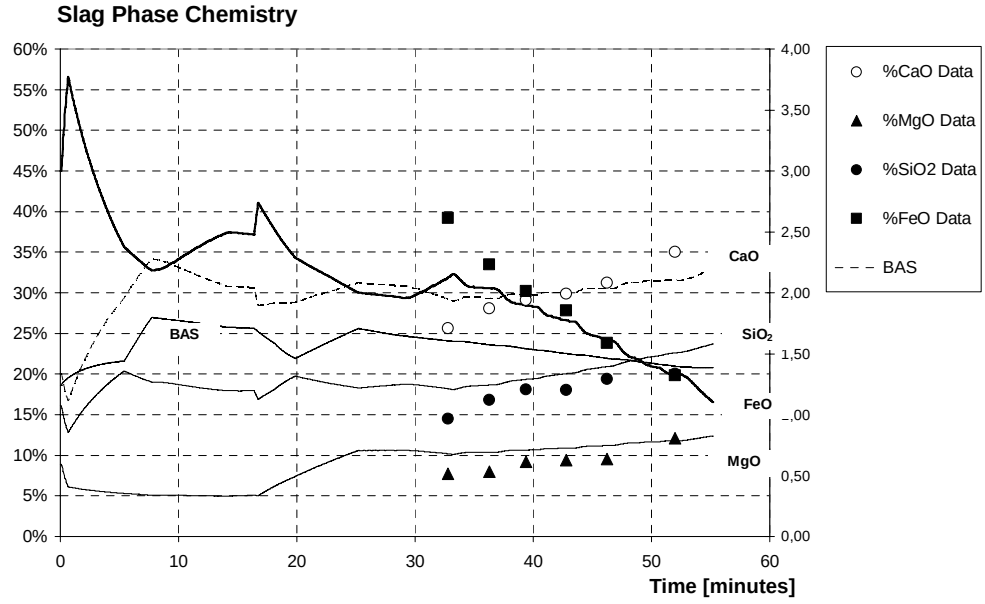

(b) melting rates: pig iron 1872 kg/min; scrap 3952 kg/min

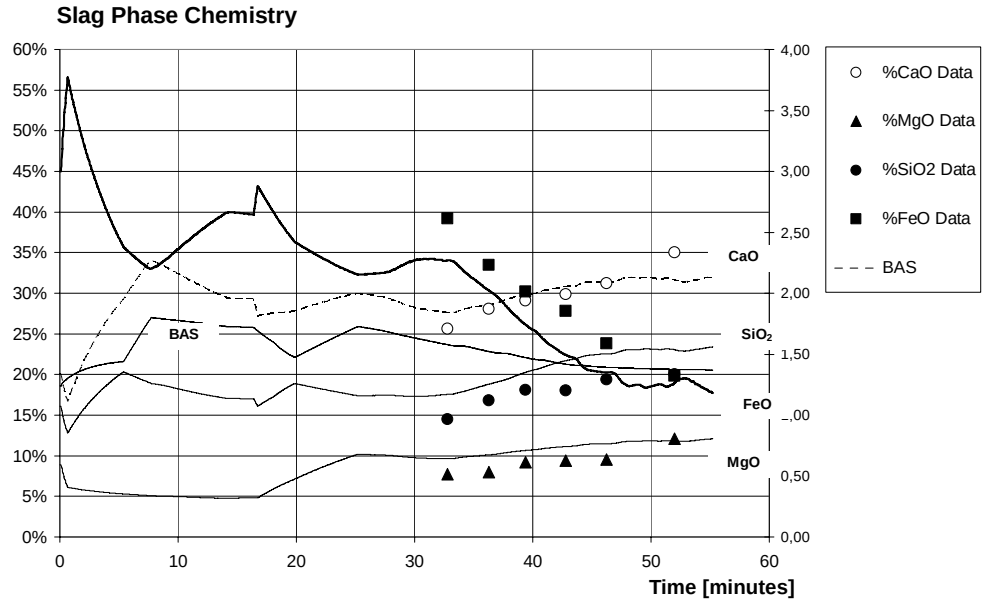

(c) melting rates pig iron 936 kg/min; scrap 5928 kg/min

Figure 133 – Effect of pig iron and scrap melting rates on the model prediction for slag chemistry. Heat 99318, 11% pig iron.

As expected, the sensitivity of the slag chemistry is more significant when the larger amount of pig iron is charged.

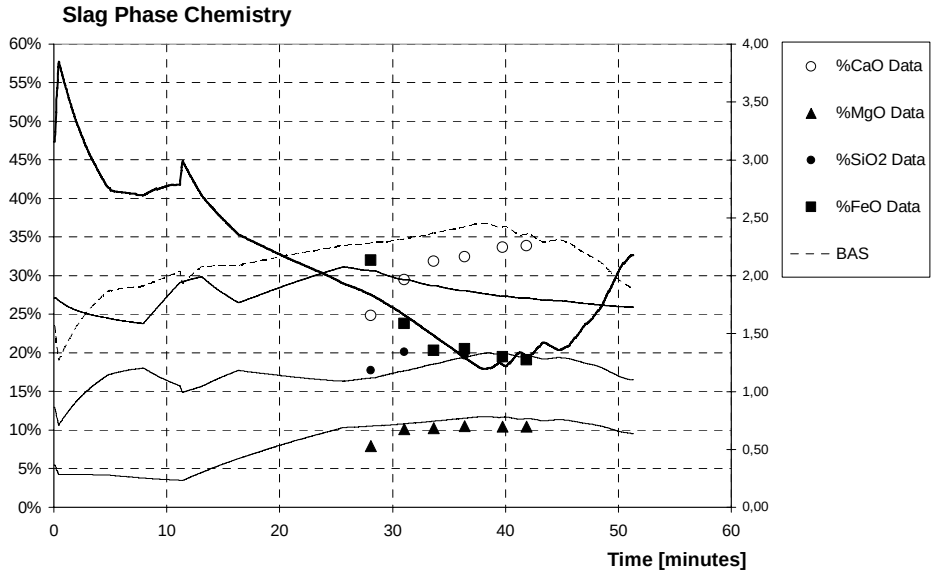

(a) melting rate: pig iron 3762 kg/min

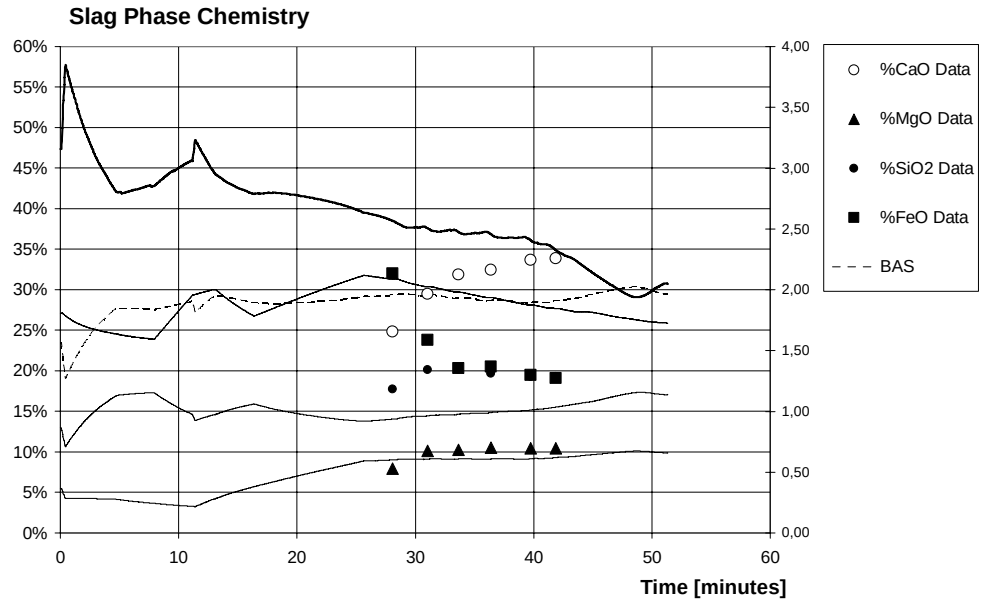

(b) melting rate: pig iron 1880 kg/min

Figure 134 – Effect of pig iron melting rates on the model prediction for slag chemistry. Heat 99736, 39% pig iron.

5.1.8.1. Melting Rates – Laboratory Experiments and the Chilling Effect

Steel samples, preheated in different extent, were immersed in Fe-C melt. Pig iron samples were non-preheated before immersing. The melting profiles for steel samples presented on Figure 135 were qualitatively consistent with other experiments conducted elsewhere [45, 51, 56, 59, 60, 63, 69, 113, 114], presenting chilling effects when the steel samples were not preheated.

The melting rate measurements of pig iron single samples seem to be quite obvious, regarding its low melting point, but contrasting with the trends obtained from the industrial data. The laboratory experiments resulted in melting times measurements almost four times shorter than steel samples, implying that the possibility of CO blanketing effect or any other retarding influence are not relevant accounting the particular testing conditions in this study.

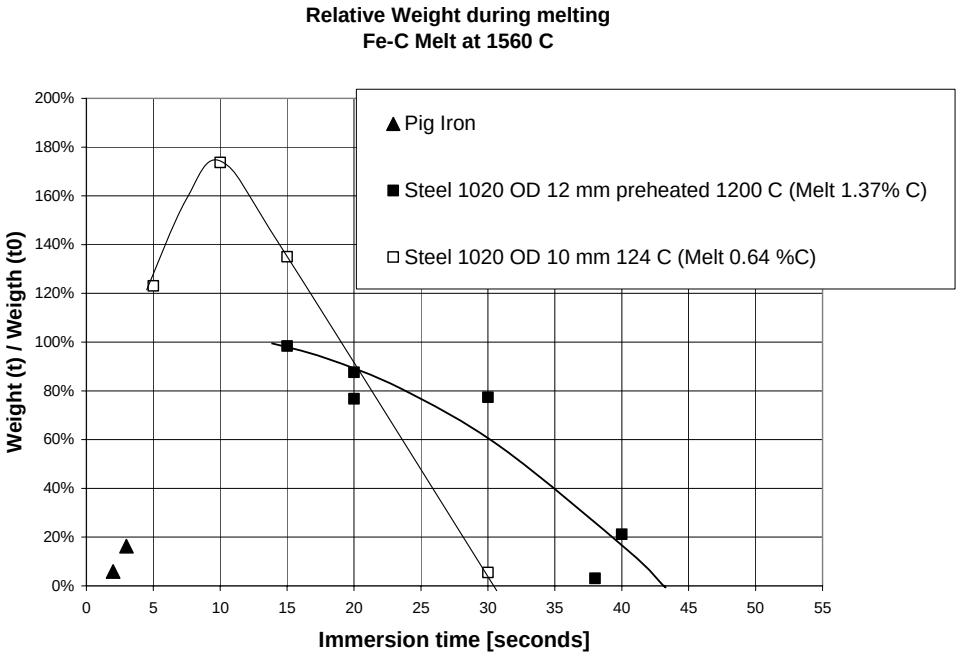

Figure 135 – Weight ratio of cylindrical samples. Mild steel samples of OD 12 mm were pre-heated up to 1200 ^{o}C and OD 10 mm up to 124 ^{o}C. Pig iron sample was not pre-heated.

The eq. 67 was modified, including the preheating enthalpy term for both iron plate and pig iron cylinder resulting in eq. 226,

$$\varphi = \frac{\rho_S.(\Delta H_m + C_{p_S}.(T_m - T_{S0}))}{C_{p_L}.\rho_L.(T_L - T_m)}.\frac{V_{S0}}{V_L} \qquad \text{eq. 226}$$

The term $C_{p_S}.(T_m - T_{S0})$ is a simplification, aiming to account the cases when the preheating temperature did not reach the melting temperature. The preheating temperature for simulation was around to 0.8 T_m .

Figure 136 presents the estimate for the melting time and the respective melting rates according to eq. 226 as well the experimental plots. The heat transfer coefficient is varied from 15,000, 25,000 to 30,000 W/(m^2.K). The heat transfer coefficient of 25,000 W/(m^2.K) fitted the experiment data regarding the steel samples. However, the radiation heat sources in the resistance furnace were not taken into account, thus, the convective heat coefficient may be lower than estimated. This estimate is in the same order of others calculated elsewhere, as presented in Table 13.

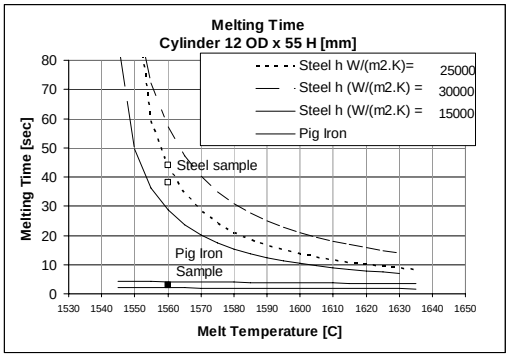

(a)

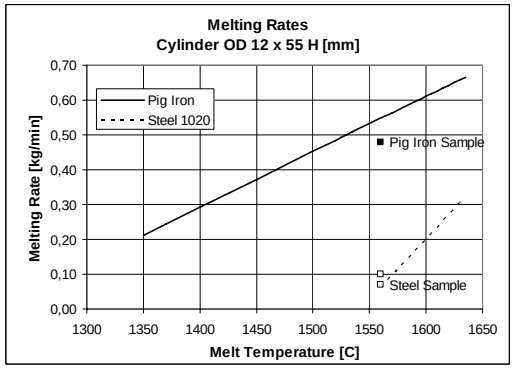

(b)

Figure 136 – (a) Melting time and (b) melting rates plot according to eq. 226 and the experiment results. The steel samples were preheated up to 1200 ^{o}C.

The short melting time and undefined final diameter of pig iron samples resulted in low measurement accuracy, meaning that melting rates maybe even higher than accounted for this study. These qualitative results are far from the reality at EAF facilities, due to the synergy among different solids charged simultaneously: plates, thin plates, cylinders, etc., and besides, usually immersed in limited melt volume. Hence, it is quite reasonable to presume that the chilling effect is very probable in the first basket and even in second one, depending on the progress of energy input. Motivated by such complexity, some researchers started applying the concept of multiple samples [63], trying to simulate conditions closer to the real situation in an EAF hot heel.

The area to volume ratio for different geometries according to typical scrap grades usually charged in EAF is presented on Figure 137 and detailed in Table 27. Pictures of scrap grades of low, medium and high density are shown in Figure 138, Figure 139 and Figure 140, respectively.

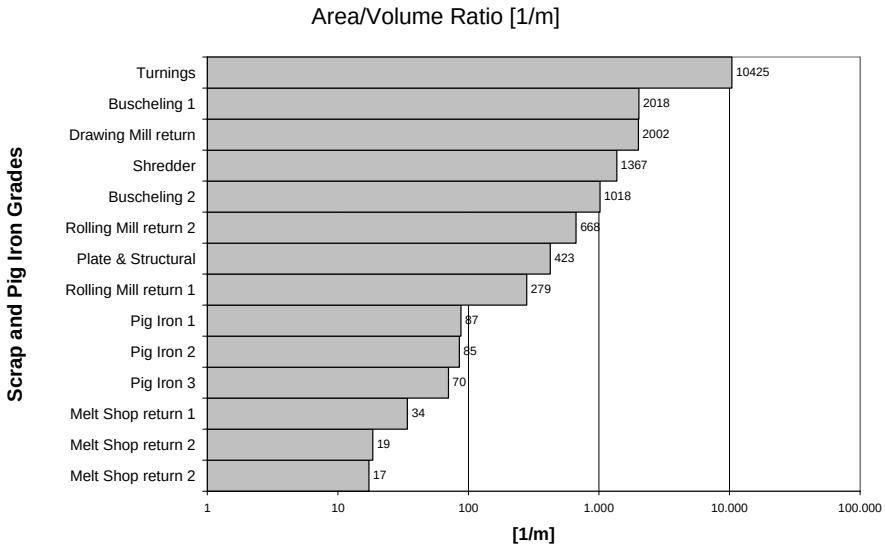

Figure 137 – Area to volume ratio for typical scrap and pig iron grades.

Table 27 – Area to volume ratio for typical scrap and pig iron grades.

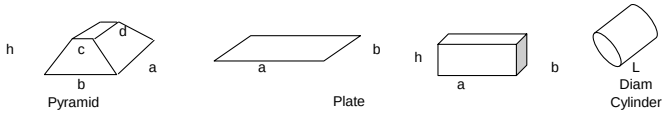

	METALLIC GRADE	Diam	L	a Length	b Width	c Top Width	d Top Length	h Hight or Thickness	Area	Volume	Area/Volume Ratio	Weight
		[mm]	[mm]	[mm]	[mm]	[mm]	[mm]	[mm]	[m2]	[m3]	[1/m]	[kg]
Pyramid	Pig Iron 1			150	120	30	80	95	5,65E-02	6,46E-04	87	5,1
Pyramid	Pig Iron 2			150	110	10	30	95	4,53E-02	5,32E-04	85	4,2
Pyramid	Pig Iron 3			450	180	110	350	70	1,96E-01	2,79E-03	70	21,9
Plate	Buscheling 1			400	150			1	1,21E-01	6,00E-05	2018	0,5
Plate	Buscheling 2			400	150			2	1,22E-01	1,20E-04	1018	0,9
Plate	Shredder			150	100			1,5	3,08E-02	2,25E-05	1367	0,2
Plate	Plate & Structural			800	100			5	1,69E-01	4,00E-04	423	3,1
Plate	Turnings			80	5			0,2	8,34E-04	8,00E-08	10425	0,0
Plate	Melt Shop return 1			130	130			600	3,46E-01	1,01E-02	34	79,8
Plate	Melt Shop return 2			250	250			800	9,25E-01	5,00E-02	19	393,5
Cylinders	Melt Shop return 2	250	800						6,77E-01	3,93E-02	17	309,1
Cylinders	Rolling Mill return 1	15	80						3,95E-03	1,41E-05	279	0,1
Cylinders	Rolling Mill return 2	6	800						1,51E-02	2,26E-05	668	0,18
Cylinders	Drawing Mill return	2	500						3,14E-03	1,57E-06	2002	0,01

Scrap grades can be loaded in different positions in the bucket. Usually they are loaded in alternate layers in the bucket volume, and preference is given for heavy scrap on the bottom and lighter ones on the middle and top. The motivations for these job procedures which are currently adopted in most of EAF facilities are: (i) to avoid heavy pieces cave in against the electrodes causing breakages; (ii) to provide longer time for melting heavy pieces.

Buscheling (Thin Plates)

Buschelings (Plates)

Entangled (Wire)

Steel Turnings

Figure 138 – Low density scrap (0.25 – 0.55 ton/m^3)

Low density scrap that usually presents very high area to volume ratio tends to preheat and melt faster than other scrap grades. This behavior results in higher consumption of available enthalpy of the surrounding liquid metal phase. Emphasis is given for steel turnings that can provide area to volume ratio around 1,000 times higher than heavy scrap and 5 to 20 times higher than medium density scrap grades. Depending on the local scrap market, steel turnings may vary from 5 to 30% of the scrap mix.

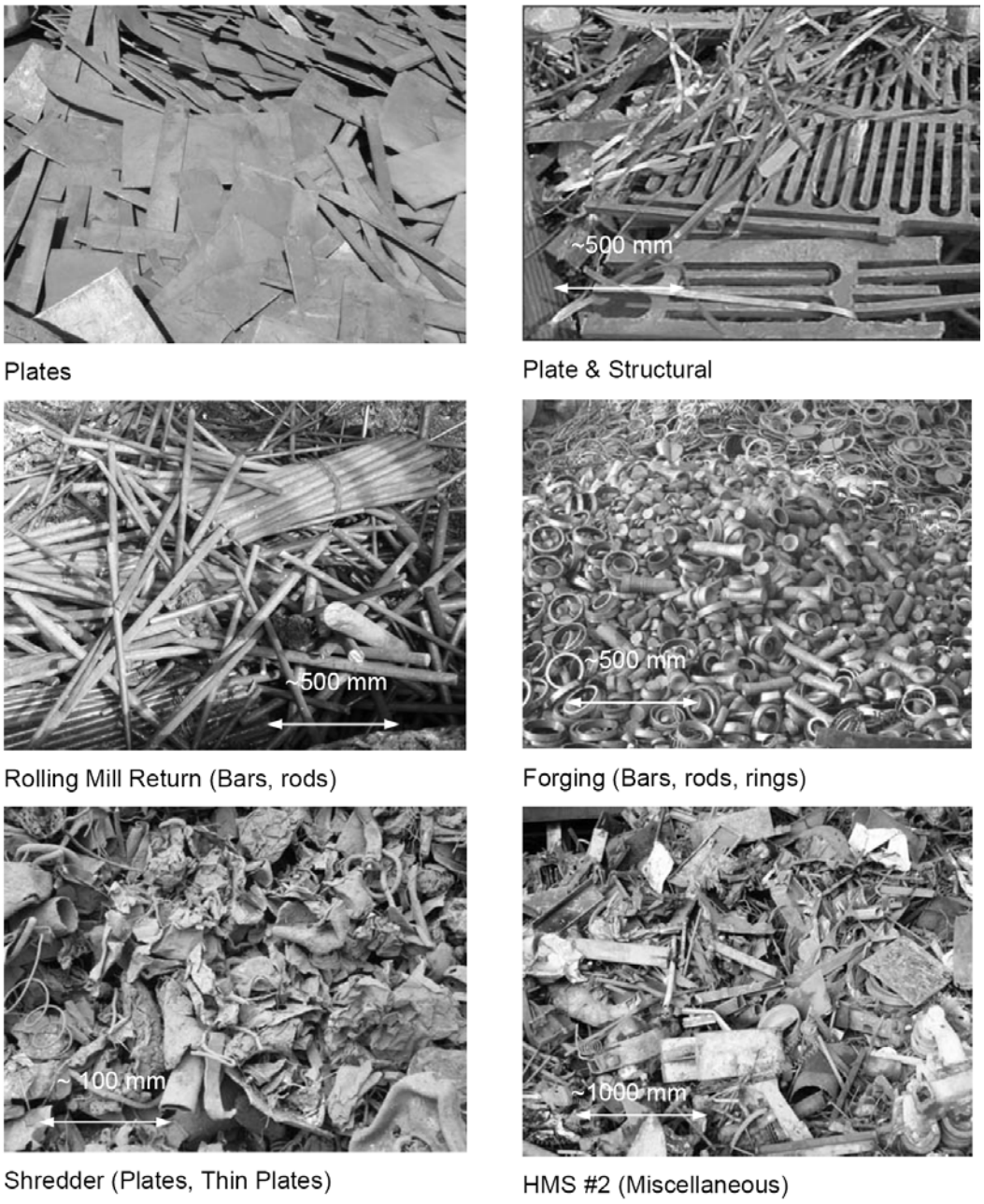

Figure 139 – Intermediate density scrap (0.60 – 1.1 ton/m3)

Intermediate density scrap are preferred by production engineers, since they fill out the EAF volume properly, avoiding scrap leveling delays due to light scrap as well decreasing the possibility of remaining non-melted heavy pieces by the end of the heat. Nevertheless, medium scrap usually provides interstitial room which can accommodate scrap of smaller size.

Figure 140 – High density scrap and pig iron

Heavy scrap grades presenting massive geometry are sometimes prohibited in EAF facilities, not only due their limited melting rates, but also because they remain non-melted during the refining step, becoming very often a cause of water cooled parts damage by fire back of supersonic oxygen jet. Pig iron is considered a heavy grade, however it can be distributed in layers and spread all over the bucket volume. Contradicting the expected high melting rates, pig iron is usually constrained up to 20-30% of the charge because of the melting difficulties as reported by several mills.

Such huge differences in area to volume ratio among scrap grades lead to a wide range of potential melting rates. The simplified model, according to $t_m = C_{p_L}\rho_L.V_L/h.A_0.f(\varphi)$ (eq. 73) and φ (eq. 226), is applied to predict melting rates of mild steel in geometries such plates, cylinders and pig iron in sphere shape. Examples of typical scrap dimensions are described on Table 28 and the computed melting rates estimates are presented on Figure 141 .

Table 28 – (a) Dimensions of typical scrap and pig iron grades applied to Figure 141 and Figure 144; (b) Physical properties

		One piece							
		$Width_S$	L_S	$Thick_S$	V_{S0}	A_{S0}	A/V	Ws	r_{mix}
		Diameter	Length	Thickness	Initial Solid Volume	Initial Solid Area	Area/ Volume Ratio	Initial Solid Weight (one piece)	Apparent Solid Density
		[mm]	[mm]	[mm]	[m3]	[m2]	[1/m]	[kg]	[ton/m3]
Mild Steel	Thin Plate	5	200	3	3,0E-06	3,2E-03	1077	0,02	0,50
	Plate	20	500	10	1,0E-04	3,0E-02	304	0,79	0,85
	Cylinder	15	500	0	8,8E-05	2,4E-02	271	0,70	1,00
	Heavy Cylinder	150	600	0	1,1E-02	3,2E-01	30	83,4	2,10
Pig Iron	Sphere	110	0	0	7,0E-04	3,8E-02	55	5,1	3,50

(a)

		Melt	Steel 1020	Pig Iron
%C			0,20%	3,9%
ΔH_m	[J/kg]		2,47E+05	2,27E+05
ρ	[kg/m3]	f(T,%C)	7,87E+03	7,27E+03
C_p	[J/kg.K]	f(T,%C)	7,90E+02	7,21E+02
T_m	[oC]		1522	1191
T_{S0}	[oC]		1500	1100
h	[W/m2.K]	25000		

(b)

The melting rate curves presented on Figure 141 take into account that: (i) only one geometry is charged at one time; solids preheating in the gas phase is conducted up to 1500 ^oC and 1100 ^oC, for steel and pig iron, respectively; (ii) the bulk temperature is homogeneous for all geometries immediately before immersion in the melt (hot heel); (iii) the overall heat transfer coefficient is 15,000 W/(m^2.K) and constant; (iv) the scrap distribution immersed in the melt is such that there is no any mass or heat transfer influence of one solid on any other of its own geometry. Therefore, for these singular conditions described above, some conclusions could be stated from Figure 141:

- different mild steel geometries loaded with the same weight may result in 1,000 times difference in melting rates due to very distinct area available for heat transfer. The melting rates increase following the sequence: heavy cylinders, cylinders, plates and thin plates;

- The higher the melt temperature, the higher the melting rates of any geometry, and the lower the required hot heel volume to start the melting period. Absence of plots means that the available enthalpy in the melt is not enough to start melting the immersed solid because of the chilling effect;
- Due to the low melting point, high melting rates are predicted for pig iron in sphere shape. Only mild steel plates and thin plates may present comparable melting rates;

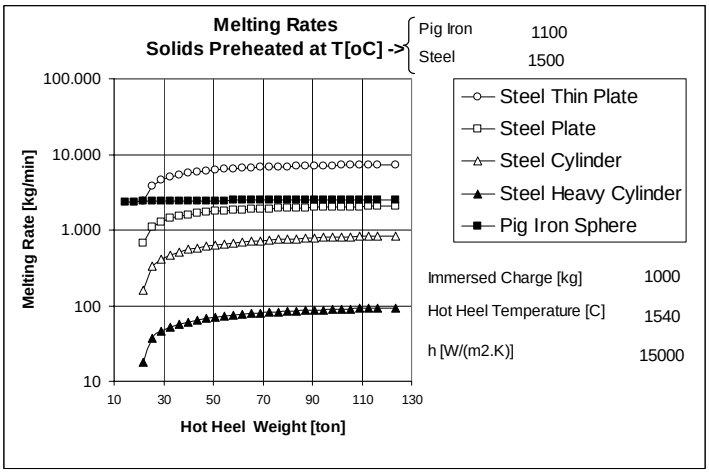

(a)

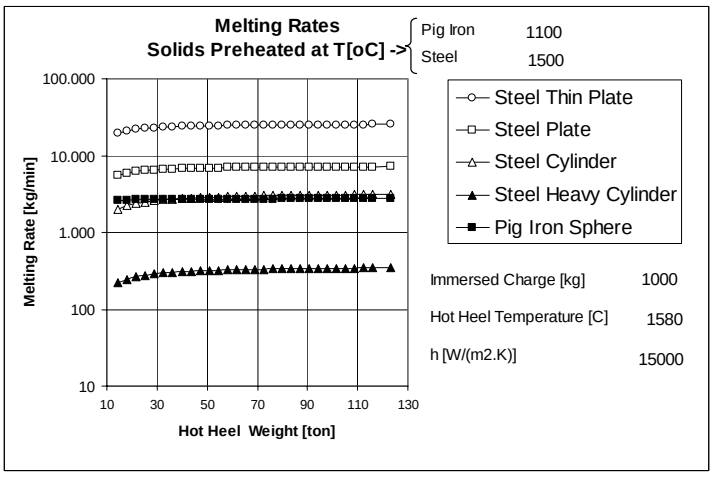

(b)

Figure 141 – Melting rates prediction for 1,000 kg of different geometries immersed individually in melt volume (Hot Heel) varying from 10-120 ton at: (a) 1540 ^{o}C and (b) 1580 ^{o}C.

According to the industrial data, the metal phase temperature is quite constant in the range of 1550-1570 ^{o}C at least during 60-80% of total electricity consumption. This might imply that the melting process is almost isothermal. Additionally from Figure 142, it can be suggested that the following 10-20% of

total electricity consumption is dedicated to overheat the metal phase in the range of 1620-1650 ^{o}C before tapping.

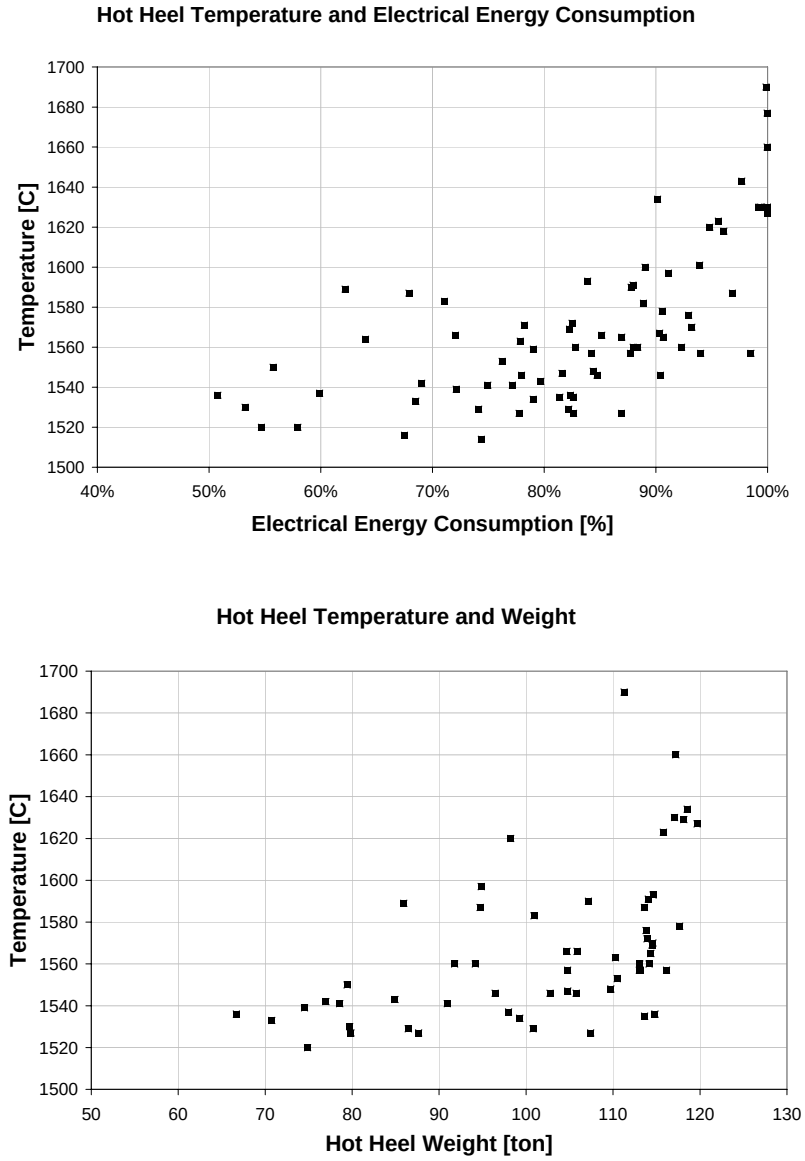

Figure 142 – Hot heel temperature measurements and calculated weight considering a 100 ton EAF tapping capacity and resident hot heel of 15-20 ton.

The merging of Figure 142 (a) and (b) results in Figure 143, presenting the plot of the computed hot heel weight as a function of the electrical energy input ratio. Hence, it is assumed that when the electrical energy input along the meltdown reaches 75-85% of total electricity consumption in conventional EAF, it could be roughly expected that most of the scrap is molten and the remaining

solid charge of 10-15 ton is already preheated and immersed in substantial hot heel estimated around 100-110 ton.

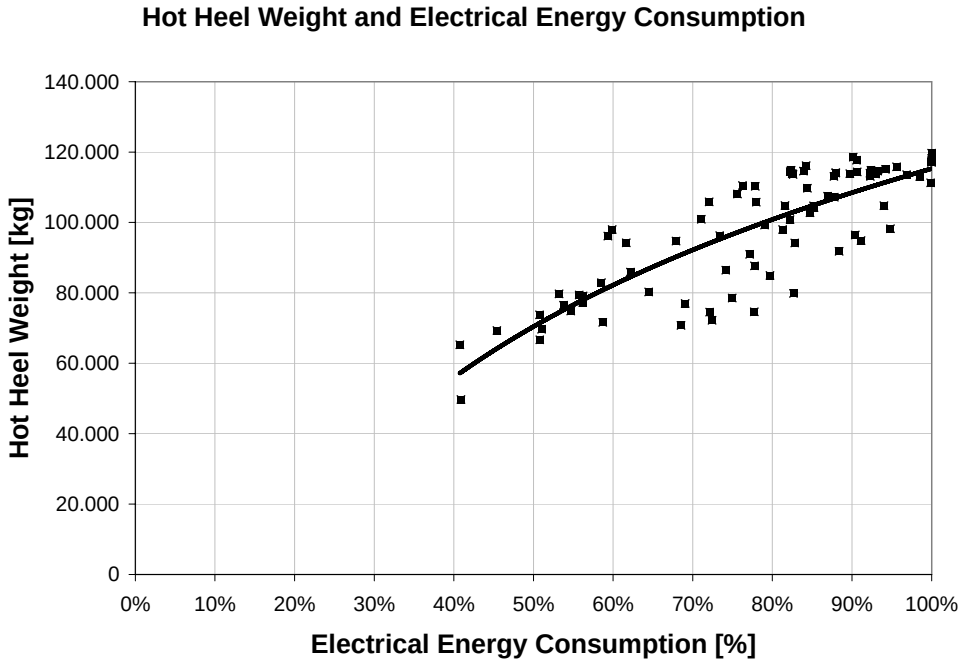

Figure 143 – Calculated Hot heel weight vs. electrical energy consumption ratio

According to eq. 73 and eq. 226, the melting rates are computed and are presented in Figure 144 for different solid geometries, presuming that: (i) before immersed in the hot heel, the solids are homogeneously preheated in the gas phase up to 1500 oC, close to the mild steel melting point (1522 ^{o}C); (ii) heat transfer coefficient for the solids in the metal phase is constant and equivalent to 25,000 W/(m^2.K); (iii) for this particular calculation, the different solid geometries are not immersed simultaneously, aiming to simulate the overall melting rate of the remaining solid in the hot heel influenced only by one geometry at one time; (iv) the amount of solids immersed in the hot heel depends on the hot heel volume and the scrap apparent density. Therefore, it was varied in the ratio 1:1 melt density and solid apparent density. Besides, Figure 144 presents the plot of the computed melting rates for the scrap mix and pig iron, according to the model proposed in this study. The estimates according to eq. 73 and eq. 226 do not consider the chemical composition of pig iron and are not plotted this time, because they are much higher than mild steel in any geometry. Table 29 describes the data for the different geometries.

Table 29 – Data for melting rate simulation

	$Width_S$	L_S	$Thick_S$	V_{S0}	A_{S0}	A/V	Ws	ρ_{mix}	Ws	Number of Pieces
	Diameter	Length	Thickness	Initial Solid Volume	Initial Solid Area	Area/ Volume Ratio	Initial Solid Weight (one piece)	Apparent Solid Density	Total Solid Weight (all pieces)	
	[mm]	[mm]	[mm]	[m3]	[m2]	[1/m]	[kg]	[ton/m3]	[ton]	[n]
Thin Plate	5	20	5	5,0E-07	4,5E-04	900	0,004	0,50	8,3	2.096.569
Plate	20	500	10	1,0E-04	3,0E-02	304	0,8	0,75	11,7	14.879
Block	400	500	250	5,0E-02	8,5E-01	17	394	3,00	11,7	30
Small Cylinder	20	300		9,4E-05	2,0E-02	213	0,7	1,00	11,7	15.787
Medium Cylinder	100	300		2,4E-03	1,3E-01	53	18,5	1,10	11,7	631
Heavy Cylinder	150	600		1,1E-02	3,5E-01	33	83,4	2,10	11,7	140
Sphere	200			4,2E-03	1,3E-01	30	33,0	2,50	11,7	355

Three metal phase temperatures of 1560, 1570 and 1580 ^{o}C were simulated and turned out to be very influential. The overall scrap mix melting rates computed based on industrial data fitted for a mild steel cylinder shape with dimensions (diameter x length) of 20x300 mm, 100x300 mm and 150x300 mm, respectively. For pig iron plot from industrial data, the melting rates fitted for mild steel cylinder shape of 100X300 mm, sphere with diameter of 200 mm and 300 mm, respectively. These estimates are consistent with experiments conducted in industrial facilities [42, 43], when it was concluded that pig iron melting rates behave similar to the heavy scrap grades.

The thin plate and plate shapes pointed out higher rates due to the larger heat transferring area when compared to cylinders and sphere geometries with the same weight. It is reasonable to presume that in case of solidified shield formation occur, its geometry would tend to circular dimensions such cylinders and sphere, instead of rectangular section.

For both mild steel and pig iron submitted to industrial conditions, the plot of the overall melting rates increased significantly when the hot heel weight was computed higher than 110 ton. The substantial increase in the metal phase temperature could explain such effect, according to the industrial measurements of metal phase temperature presented in Figure 142.

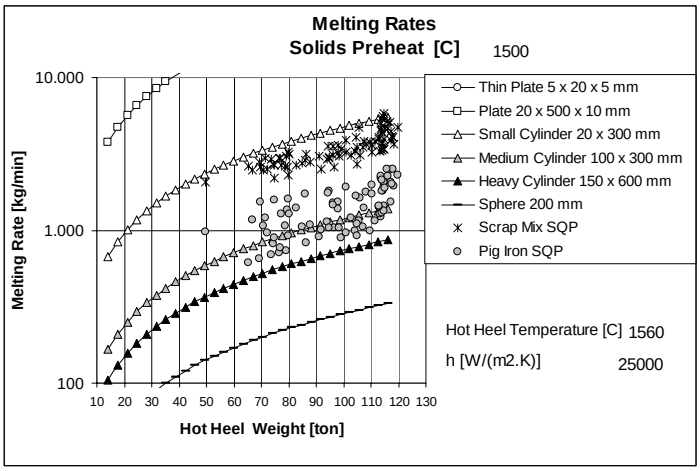

(a)

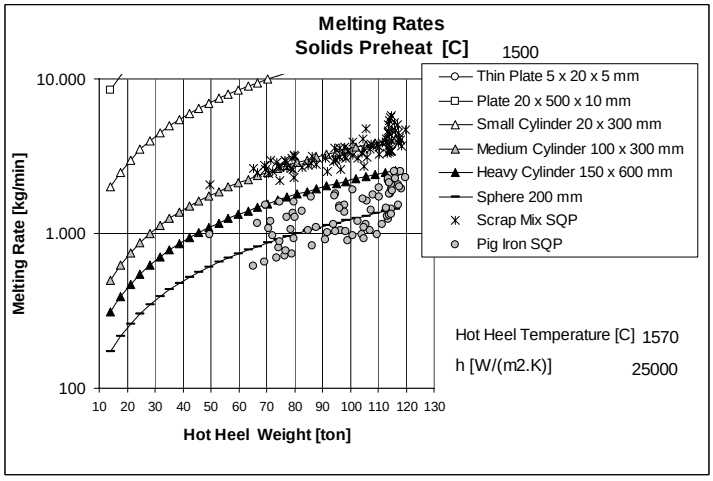

(b)

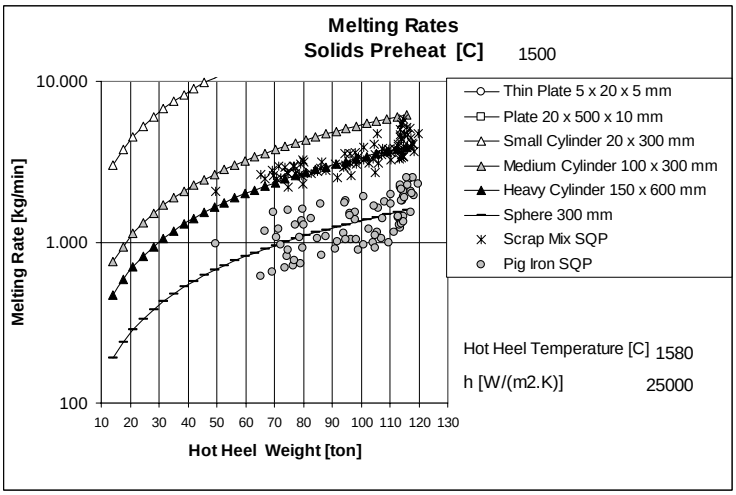

(c)

Figure 144 – Effect of melt temperature on melting rates prediction for variable weight of different geometries immersed individually in melt volume (Hot Heel). Melting rates discrete plots for scrap mix and pig iron were obtained though GRG calculation based on industrial tests.

In contrast, the melting rate computed for pig iron according to the model proposed in this study is much lower than the estimates suggested by eq. 73 and eq. 226. Another set of laboratory experiments were conducted in order to simulate higher chilling effect, which could explain the low melting rates computed for pig iron under industrial conditions. The sample design implied in wrapped up mild steel and pig iron cylinders in steel mesh properly assembled to provide heat transferring area equivalent to commercial scrap grades. Figure 145 describes three different mesh assembly designed to achieve 15-23 times the area to volume ratio in respect of the pig iron cylinder.

	METALLIC GRADE	Area/Volume Ratio [1/m]	In respect of Pig Iron
Pyramids	PIG IRON 1	87	1.0
	PIG IRON 2	85	1.0
	PIG IRON 3	70	0.8
Plate	Buscheling 1	2018	23.1
	Buscheling 2	1018	11.6
	Shredder	1367	15.6
	P&S	423	4.8
	Turnings	10425	119.2
Cylinders	Mshop return 1	34	0.4
	Mshop return 2	17	0.2
	Rmill return 1	279	3.2
	Rmill return 2	668	7.6
	Dmill return	2002	22.9
	Total Scrap mix	153	

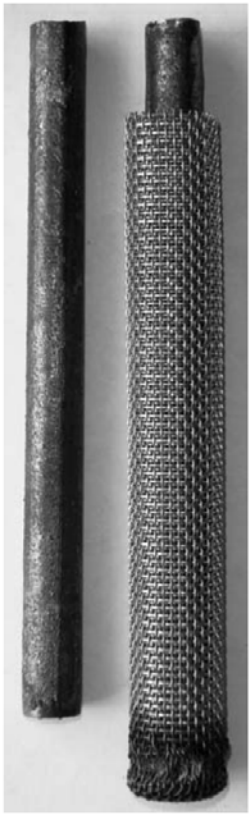

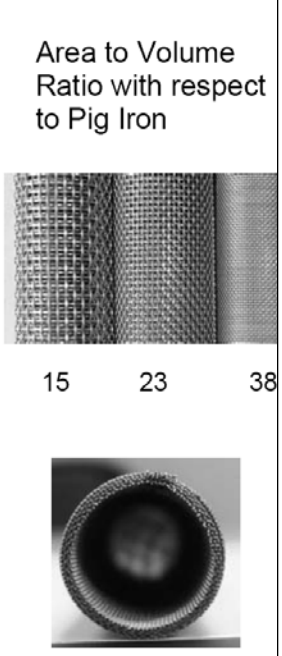

Figure 145 – Wrapped up samples

As expected for mild steel cylinders wrapped up in steel mesh, the melting time took longer when compared with single steel cylinder. The total weight of cylinder OD 10 mm and mesh was very close to the single cylinder OD 12 mm. The chilling effect was remarkable and solidified shell was always observed. Figure 146 and Figure 147 point out the occurrence of shrinkage of the solidified shell and high volume of voids which could contribute for a higher heat transfer resistance.

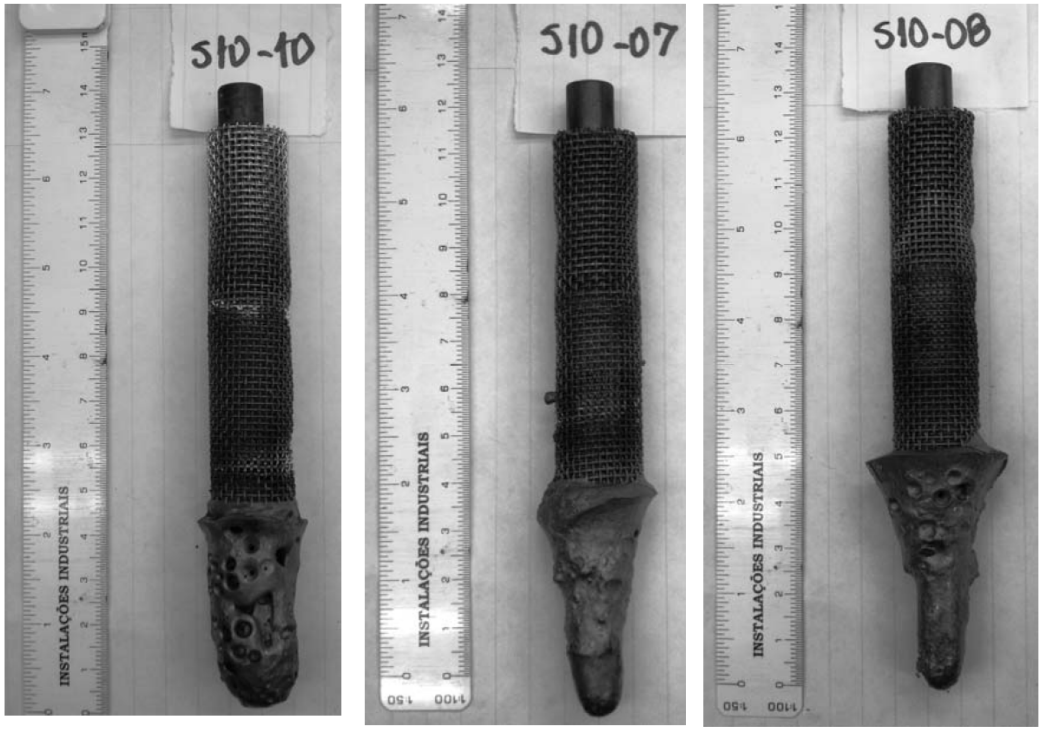

Figure 146 – Mild Steel samples wrapped up in steel mesh after immersion in melt at 1560 ^{o}C

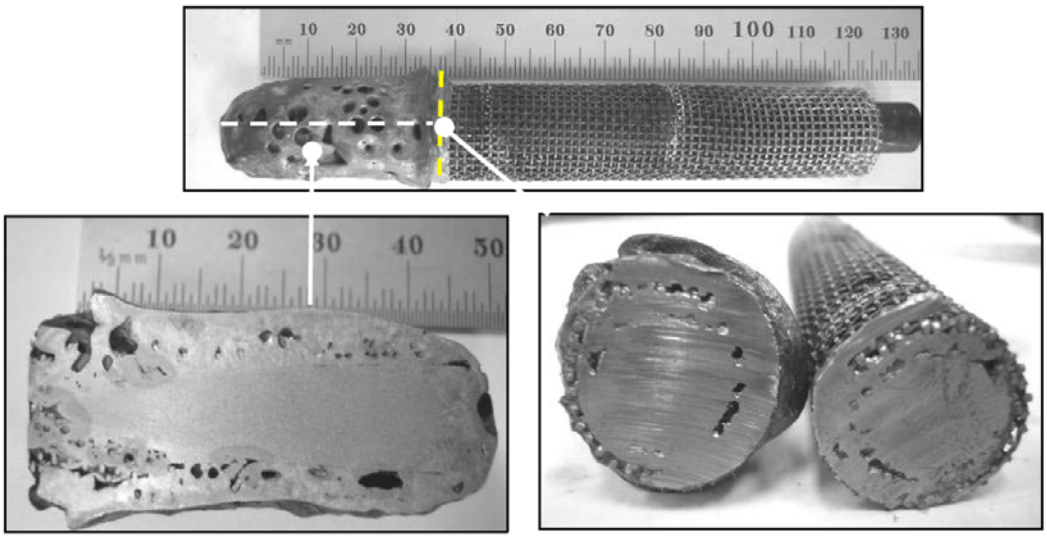

Figure 147 – Longitudinal and transversal cross section of steel samples wrapped up in steel mesh immersed in melt at 1560 ^{0}C for 10 sec (S10-10).

Samples of pig iron single cylinders were submitted to low melt temperature. Figure 148 presents the extreme chilling effect condition, where low melt temperature produced a cylindrical shield of OD 55 mm from a former cylinder of OD 12 mm in 16 sec.

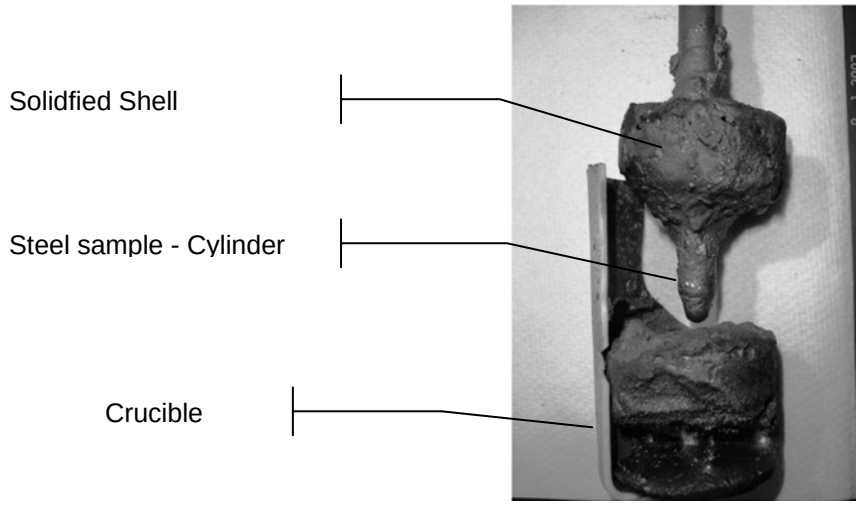

Figure 148 – Single mild steel sample immersed in melt at low temperature 1518 ^{o}C for 16 sec (S12-11).

Figure 149 presents the formation of a solidified shell over a single pig iron sample. The melt temperature was set lower than 1500 ^{o}C but higher than pig iron melting point. The metallography revealed occurrence shield shrinkage and change in the round geometry of the pig iron sample cross section. This feature suggests that the pig iron sample melted but remained encapsulated in the solid steel shell.

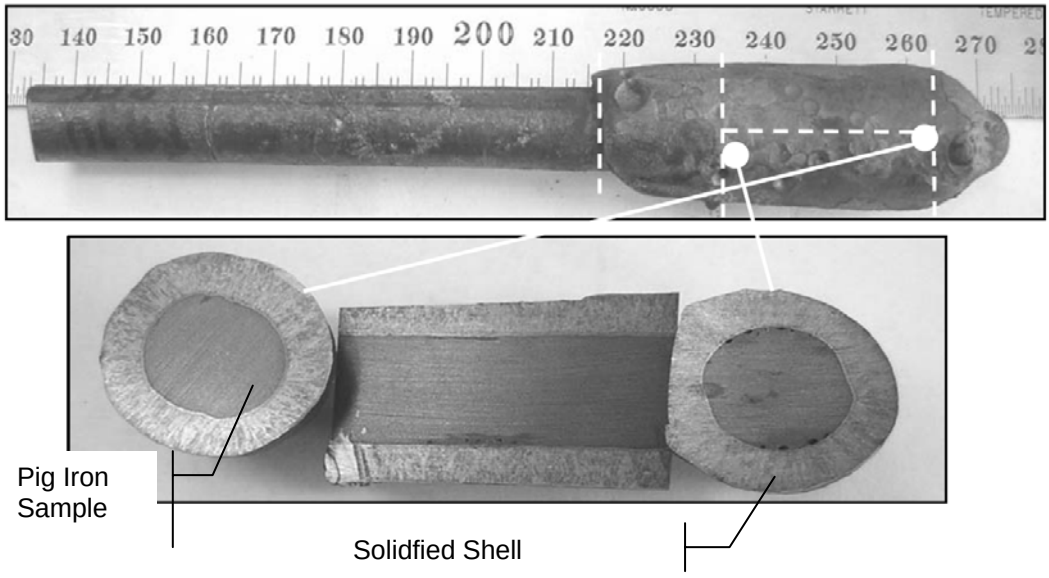

Figure 149 – Single pig iron sample immersed in melt at low temperature 1472 oC for 8 sec (PH10-206).

Immersing pig iron samples wrapped up in steel mesh at melt temperature around 1560 ^{o}C, resulted in formation of remarkable shell and melted pig iron. Figure 150 presents the rupture of the shell when the sample was removed from

the crucible, causing the encapsulated melted pig iron volume to leave the interior of the solid shell. Chemical analysis and metallography confirmed the mechanism described above.

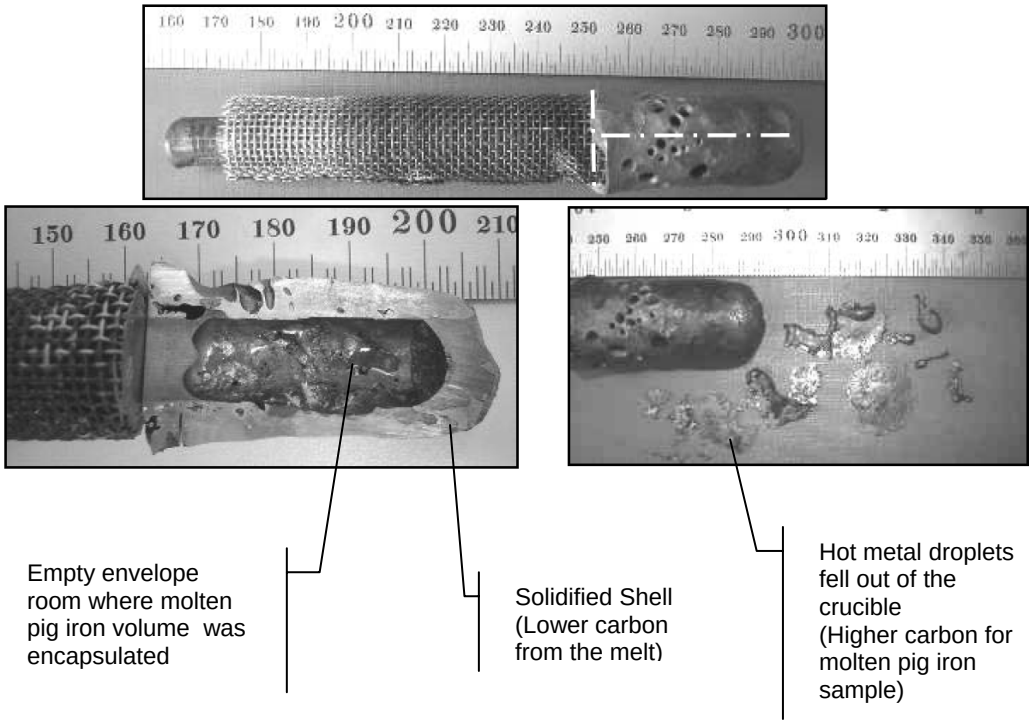

Figure 150 – Longitudinal and transversal cross section of pig iron wrapped up on steel mesh sample and immersed in melt at 1563 ^{0}C for 9 sec (PH10-200).

Under EAF industrial conditions, the same mechanism of pig iron encapsulating is supposed to take place in the hot heel. Figure 151 sketches the progress of the physical state of one piece of pig iron charged simultaneously with other scrap grades: (a) due to presence of lighter scrap grades which demand higher heat transfer rate than pig iron, a solidified shell from the surround hot heel is produced; (b) depending on the hot heel size and energy input, the former solidified shell may grow; (c) as the meltdown proceeds, heat is transferred through the shell and the pig iron temperature reaches its melting point. Thus, melt pig iron is encapsulated; (d) As the melt temperature increases, re-melting of the solidified shell begins. Besides, diffusion of carbon from the encapsulated melted pig iron into the low carbon solidified shell occurs as presented in Figure 152. Therefore, the process of dissolution of the solidified shell takes place in the internal interface. Hence, the dissolution will occur even at temperatures lower than the melting temperature of the external interface between the solidified shell and the hot heel; (e) whatever mechanism is predominant, whether internal dissolution or melting at the external interface, the

solidified shell thickness is decreased causing its final rupture and the melted pig iron is released and leaks toward the hot heel.

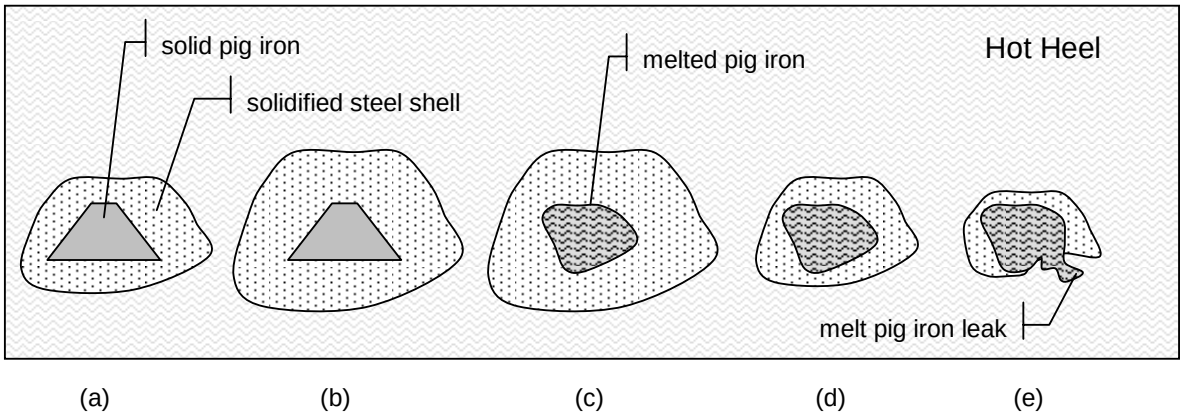

Figure 151 – Pig iron encapsulating progress and final leak to the hot heel volume

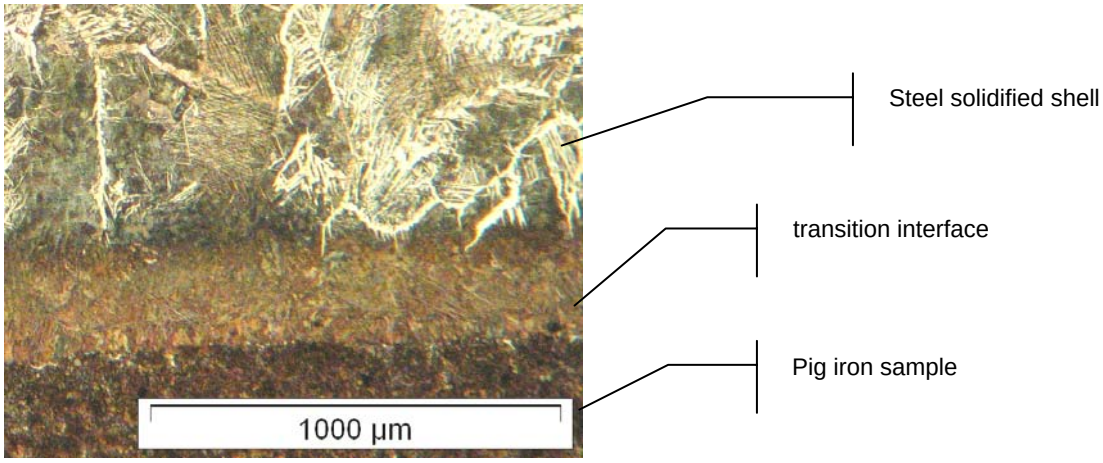

Figure 152 – Pig iron and solidified shell interface

The proposed mechanism for pig iron encapsulating is consistent with the operational observation in EAF facilities. In contrast to other operation elsewhere, it is usual to charge significant amounts of pig iron in Brazilian facilities. Hence, events of sudden boiling in the EAF are quite often observed. Depending on the pig iron encapsulating extent, huge boiling has been reported at the end of processing heat. This conclusion is also supported by the fact that, in many times the sudden boiling is reported, there is no any indication of scrap cave in from the upper water cooled wall, meaning that the boiling was caused by CO evolution from the hot heel.

Therefore, assuming that not all pig iron is released to the hot heel whenever it is melted, instead of naming pig iron melting rate in Figure 144, it should be more suitable to call that rate as pig iron availability rate.

The inherent phenomenon complexity makes quite difficult to reproduce industrial EAF conditions in laboratory scale. Consequently, the determination of melting rates for different scrap grades and their substitutes such as pig iron and HBI through laboratory experiments is very limited with the purpose of direct application in dynamic models.

Nevertheless, this study on this matter brought also insights for EAF operators and designers concerning the lower shell refractory profile and size. Additionally, it motivates the evaluation of bucket layering procedures in order to maximize melting rates, and consequently, increase the EAF productivity and safety.

5.1.8.2. Model Validation

The transient and complex nature of ferrous materials melting and the chemical reactions rates under EAF conditions make modeling prediction very dependent on the way the buckets are layered, how fast they are charged, and the ferrous materials distribution in the EAF volume as well. As mentioned earlier, the model calibration was conducted allowing several main model parameters to assume different values for different heats in order to reproduce the measured slag and metal phases chemistries. Pig iron melting rates and oxygen-carbon injection definitely affected the results. Actually, very different oxygen-carbon injection practices and pig iron charging influenced significantly the range and average values of the models parameters. Therefore, to validate the model under low variation of operational conditions, particular settings connected to real EAF operations were reproduced for five heats (n. 91014 to 91018) [115], all of them processed in sequence by the same shift personnel, keeping quite similar inputs such as oxygen-carbon injection, electrical power input and fluxes recipe. Besides, the models parameters were set constant as well, according to Table 30.

Table 30 – Models parameters settings for validation tests

				Validation Settings
Decarburization	Critical %Carbon	$[\%C]^{Cr}$	[%]	0,100%
Desiliconization	Desiliconization Parameter	k_{Si}	[min^{-1}]	
	Critical %Silicon	$[\%Si]^{Cr}$	[%]	0,074%
	Ratio k_{C2} / k_{Si} Model Avg			
Dephosphorization	"a" mA Product for Phosphorous Removal	a	[m^3/min]	2,00
	"b" mA Product for Phosphorous Removal	b	[min^{-1}]	0,00
Post Combustion Ratio	Post combustion Ratio maximum. It is the maximum value for post combustion ratio regarding the C->CO, CO2 above the slag promoted by PC Injectors	$R_{PC}^{Max\ Atm}$	[%]	0,80
	Post combustion Ratio in the Slag. It is the average value for post combustion ratio in the slag due to FeO + CO = Fe + CO2	R_{PC}^{Slag}	[%]	3,0%
Iron Oxide Reduction	FeO reduction rate constant. $k_{FeO->Fe}$ (Coke reaction).	k_{red}	[min^{-1}]	1,60
Initial Slag Amount	Initial slag amount	$W_{initial}^{Slag}$	[ton]	1,23
Oxygen - Lancing Injector	Effectiveness of the oxygen in excess from the lancing mode for the Fe oxidation to FeO. This Parameter concerns about the idle flame, which is not reaching the bath.	OLE_{FeO}	[%]	93%
Oxygen - Post Combustion Injector	Effectiveness of the oxygen available through the PC Injectors for decarburization purposes	$OPCE_{Decarb}$	[%]	15%
	Effectiveness of the oxygen available through the PC Injectors for FeO formation by reaction with solid scrap, steel bath surface and/or steel droplets	$OPCE_{FeO}$	[%]	58%
Raw Materials	Pig Iron Chemistry	$\%C\ (v)$	[%]	4,2%
		$\%Si\ (v)$	[%]	0,8%
		$\%P\ (v)$	[%]	
	Carbonaceous Materials - Injection Yield	n_{CMat}	[%]	96%
	Pig Iron Charge		%	22%
	Max Pig Iron Melting Rate		[kg/min]	1638
	Max Scrap Melting Rate		[kg/min]	4511

The computed overall melting rates for scrap mix and pig iron are presented in Figure 153, which in contrast to Figure 130 and Figure 131, the overall melting rates are presumed almost the same for the heats accounted for model validation.

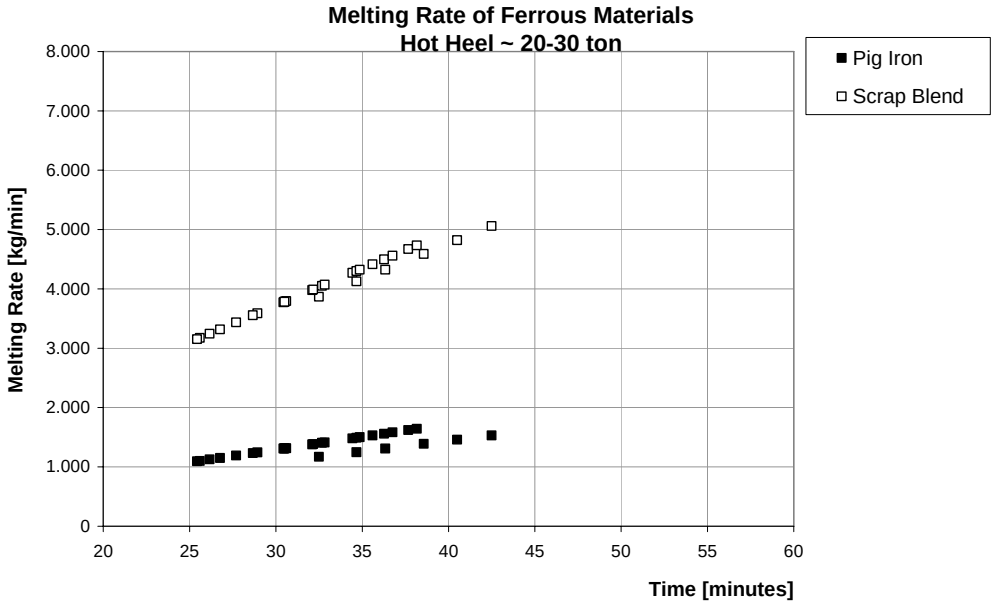

Figure 153 – Computed overall melting rates for scrap mix and pig iron charged over hot heel of 20-30 ton; included all validation heats 91014 to 91018, 22-24% pig iron.

Typical model prediction for soluble carbon and phosphorus are presented in Figure 154 for heat n. 91016. The dispersive trend shown in Figure 155 and Figure 156 for soluble carbon in the beginning of refining stage is reproduced, together with the better convergence to measured tapping carbon. The %wt C scale is amplified in Figure 155 to denote this trend.

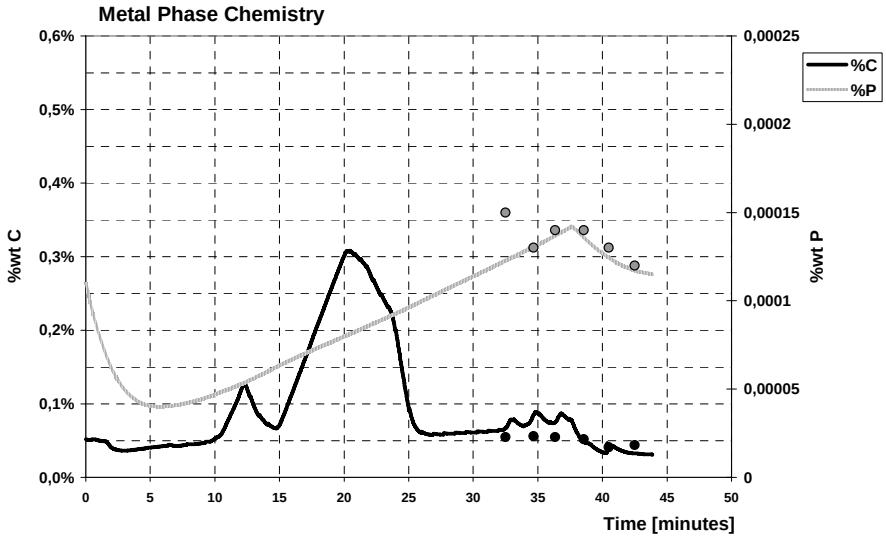

Figure 154 – Carbon and phosphorus model prediction, measured chemistry (discrete points) in metal phase; heat 91016, 23% pig iron.

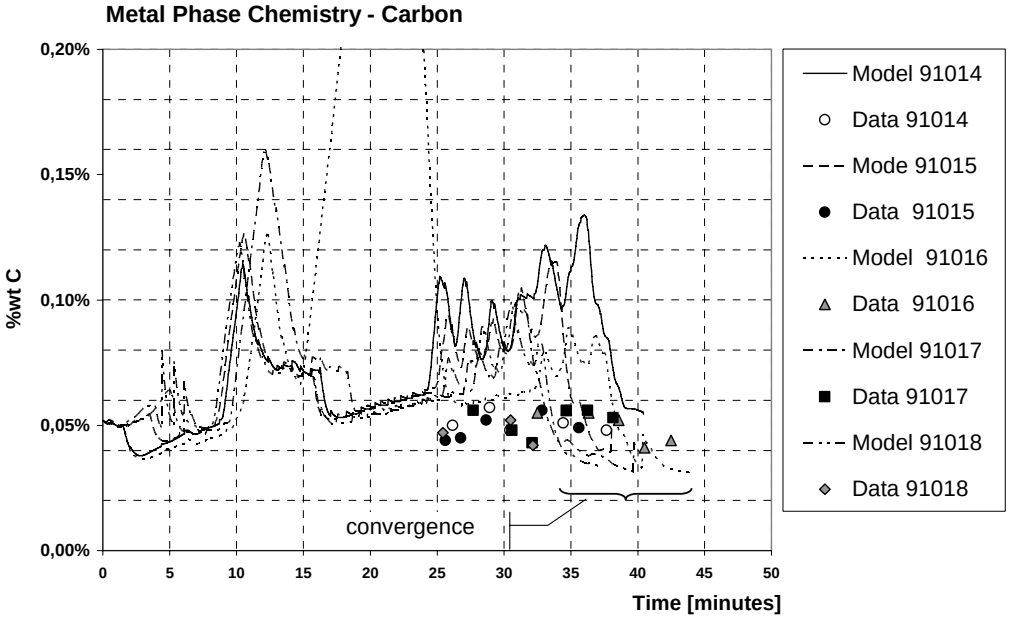

Figure 155 – Carbon content model prediction, measured chemistry (discrete points) in metal phase; included all validation heats 91014 to 91018, 22-24% pig iron.

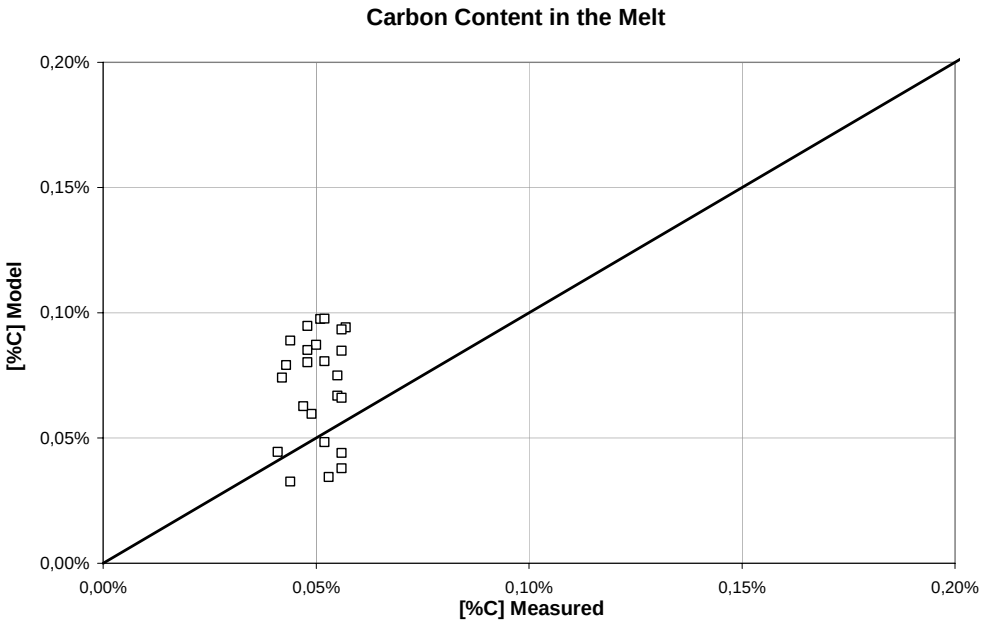

Figure 156 – %wt C measured in the melt vs. Model prediction

Phosphorus prediction in the metal phase is based on a constant product "$m_P \cdot A$". Figure 157 and Figure 158 denote a better model agreement when compared to soluble carbon prediction.

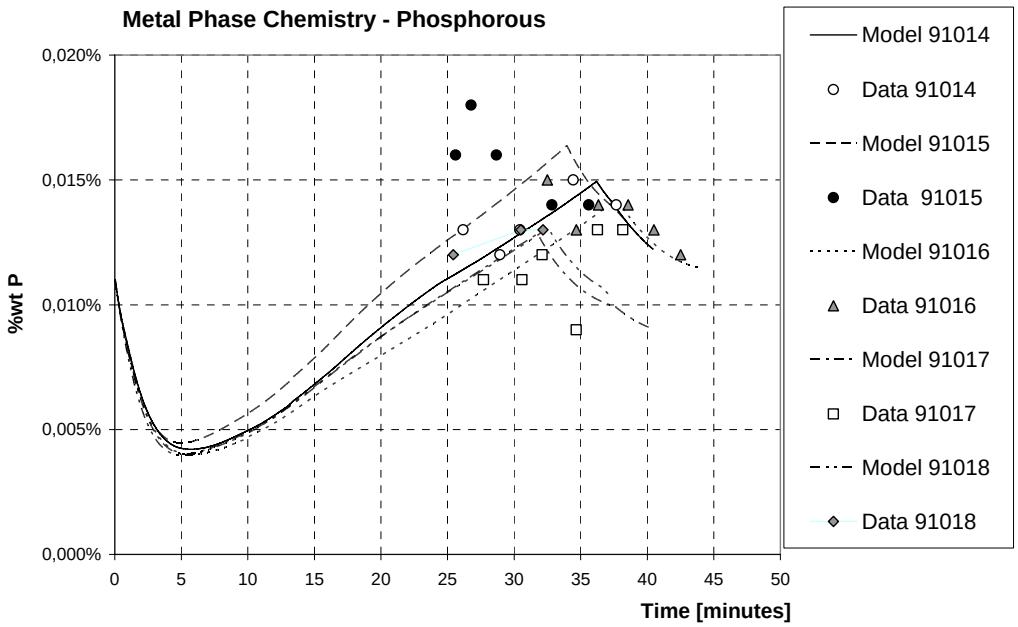

Figure 157 – Phosphorus content model prediction, measured chemistry (discrete points) in metal phase; all heats used for validation n. 91014 to 91018, 22-24% pig iron.

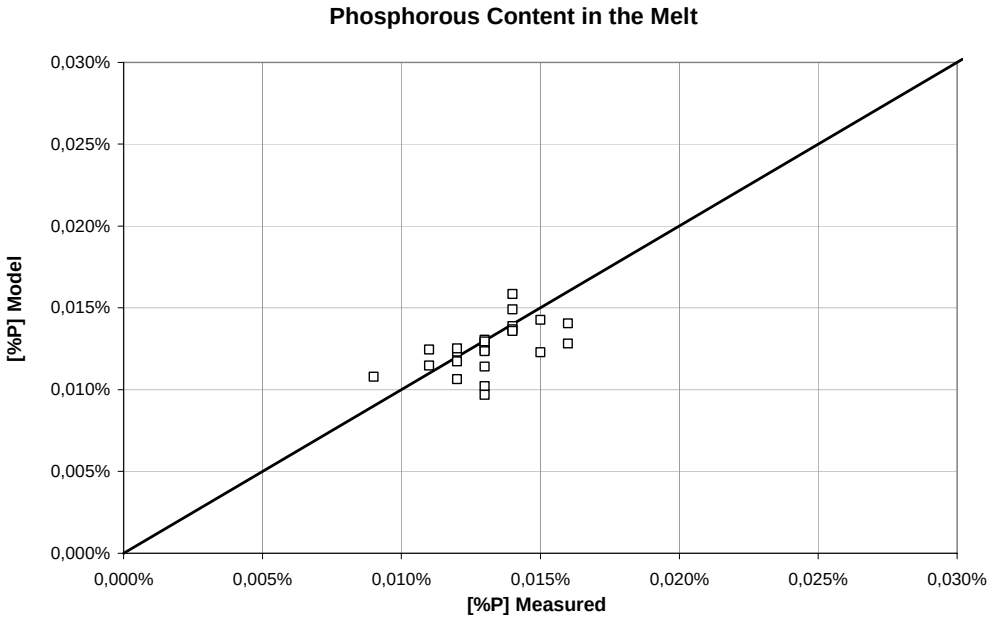

Figure 158 – %wt P measured in the melt phase vs. Model prediction.

The slag phase chemistry forecast by the model presented moderate agreement with the measured chemistry. Figure 159 shows a typical model prediction using heat 91014 as an example. Figure 160 plots heats used for model validation on the industrial scale perspective, the trends for FeO reduction resulted in quite close prediction to the measured chemistry. Accordingly, Figure

161 points out a reasonable correlation coefficient R^2 of 0.76 between the model prediction and measured chemistry.

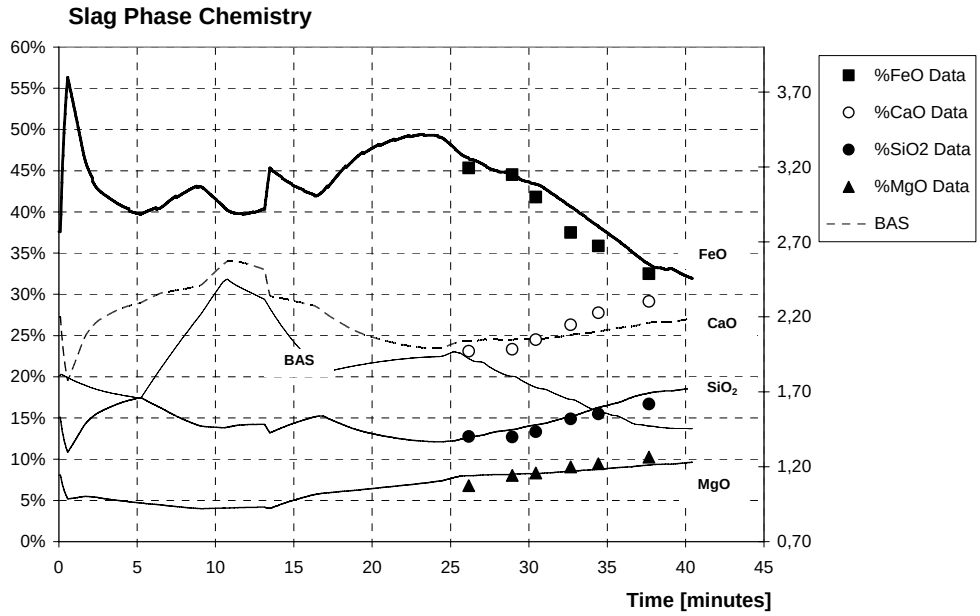

Figure 159 – Slag chemical composition predicted by the model and measured %wt chemistry (discrete points): heat n. 91014, 24% pig iron.

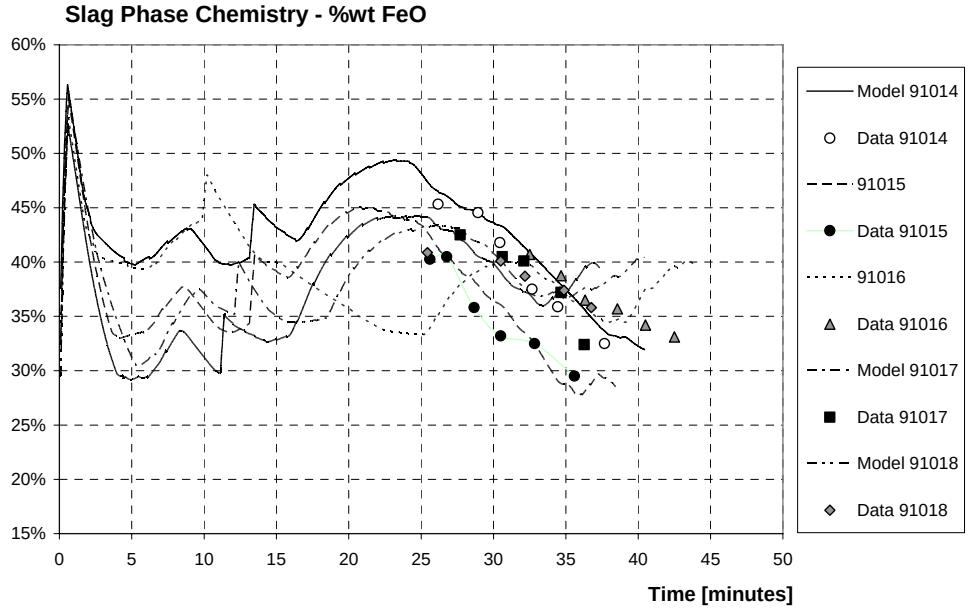

Figure 160 – wt% FeO content in slag predicted by the model and measured %wt chemistry (discrete points): all heats used for validation n. 91014 to 91018, 22-24% pig iron.

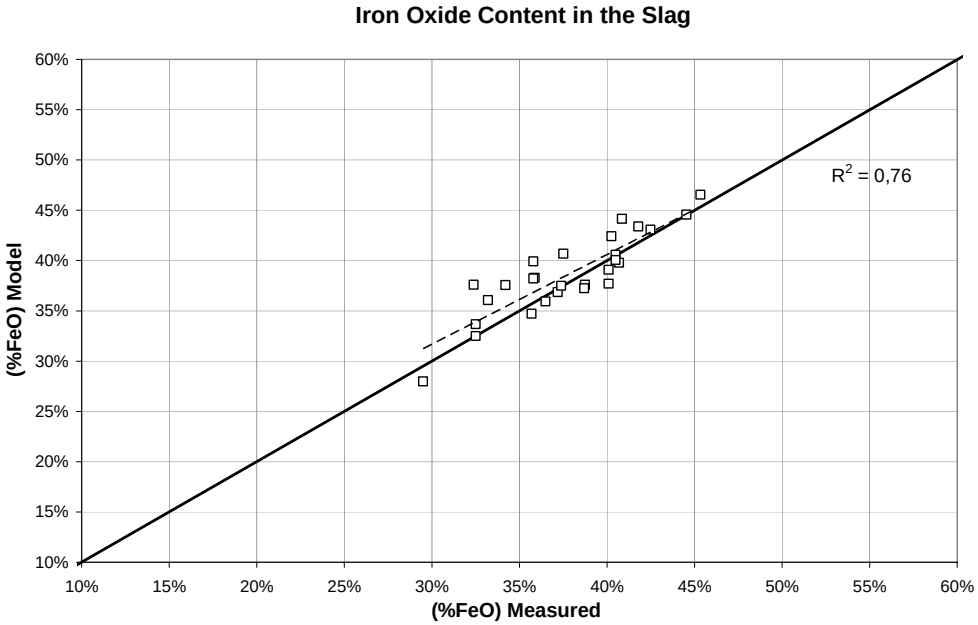

Figure 161 – %wt FeO measured in the slag vs. Model prediction

Additional comparison of predicted and measured chemistry of relevant oxides contents in slag phase is shown in Figure 162, Figure 163, Figure 164, and Figure 165, for %wt CaO, SiO_2, MgO and P_2O_5, respectively. Slag formers such as lime and dololime were charged almost in the same amount, hence, no significant variation was expected for CaO and MgO oxides contents. SiO_2 varied according to the scrap impurities content.

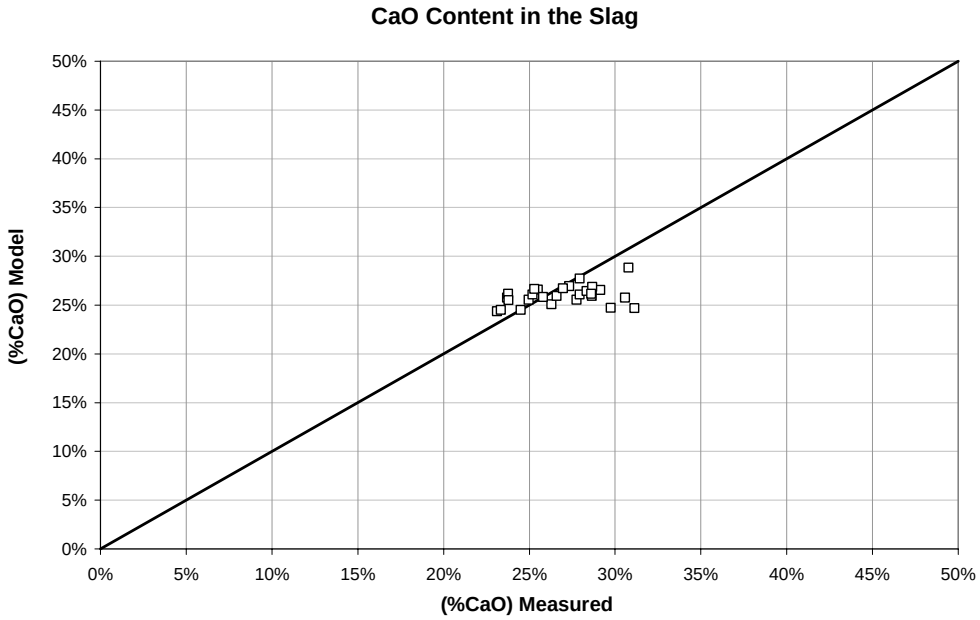

Figure 162 – %wt CaO measured in the slag vs. Model prediction

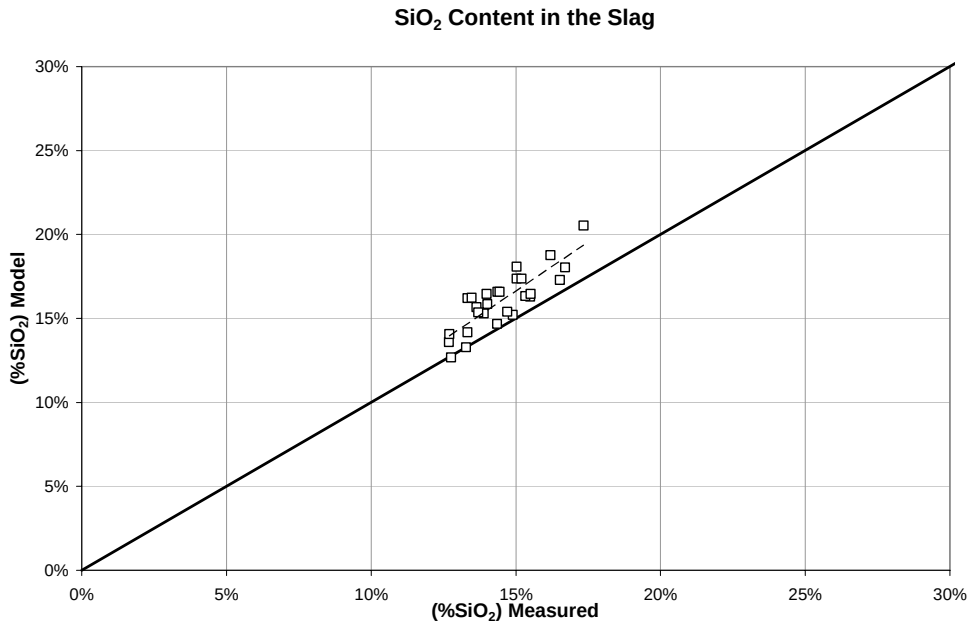

Figure 163 – %wt SiO_2 measured in the slag vs. Model prediction

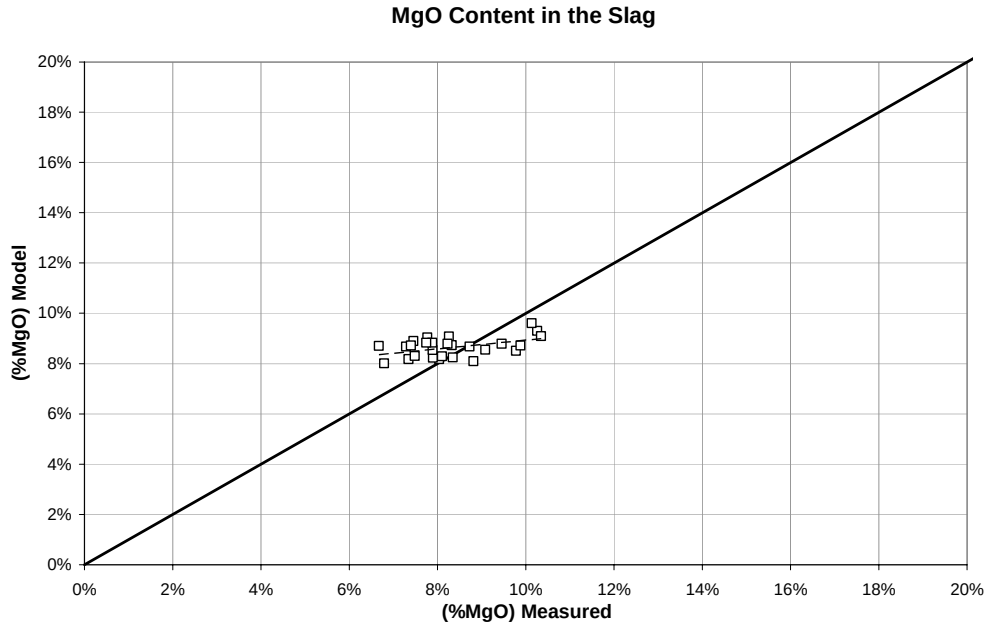

Figure 164 – %wt MgO measured in the slag vs. Model prediction

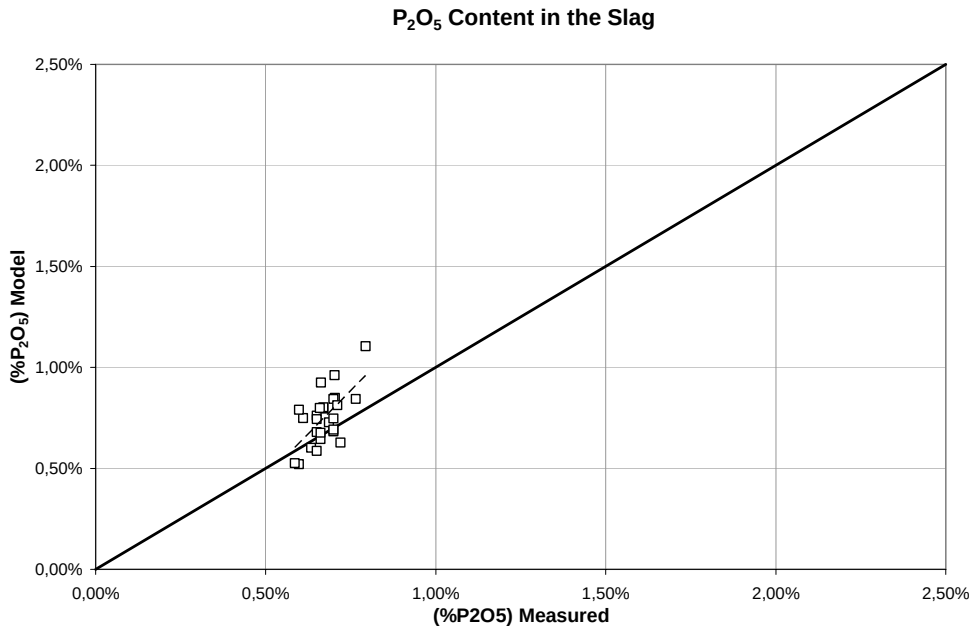

Figure 165 – %wt P_2O_5 measured in the slag vs. Model prediction

The validation tests were useful to prove the potential of the current algorithm to predict mainly the iron losses through iron oxidation-reduction reactions, under limited operational conditions range. Phosphorus has been used successfully to support inverse calculation of pig iron melting rates, at least, to forecast indirectly the soluble carbon availability in the metal phase. Further investigations should be conducted to improve soluble carbon estimates. Therefore, complimentary measurements of the off-gas flow rate and its chemical composition is strongly recommended to improve model predictions.

The use of inverse calculation to determine the model parameters could give us insights to develop a real-time tool managed by a neural network concept. The effect of variations on the scrap quality and operational job procedures could be minimized if off gas and slag mass as well their chemistry are available to calibrate the model.